

REPORT DOCUMENTATION PAGE				<i>Form Approved</i> OMB No. 0704-0188	
Public reporting burden for this collection of information is estimated to average 1 hour per response, including the time for reviewing instructions, searching existing data sources, gathering and maintaining the data needed, and completing and reviewing this collection of information. Send comments regarding this burden estimate or any other aspect of this collection of information, including suggestions for reducing this burden to Department of Defense, Washington Headquarters Services, Directorate for Information Operations and Reports (0704-0188), 1215 Jefferson Davis Highway, Suite 1204, Arlington, VA 22202-4302. Respondents should be aware that notwithstanding any other provision of law, no person shall be subject to any penalty for failing to comply with a collection of information if it does not display a currently valid OMB control number. PLEASE DO NOT RETURN YOUR FORM TO THE ABOVE ADDRESS.					
1. REPORT DATE (DD-MM-YYYY) 09/04/2012		2. REPORT TYPE Final		3. DATES COVERED (From - To) 7/1/2009-5/31/2012	
4. TITLE AND SUBTITLE Advanced Material Intelligent Processing Center: Next Generation Scalable Lean Manufacturing				5a. CONTRACT NUMBER	
				5b. GRANT NUMBER N000140911011	
				5c. PROGRAM ELEMENT NUMBER	
6. AUTHOR(S) John W. Gillespie, Jr. and Suresh G. Advani				5d. PROJECT NUMBER	
				5e. TASK NUMBER	
				5f. WORK UNIT NUMBER	
7. PERFORMING ORGANIZATION NAME(S) AND ADDRESS(ES) Center for Composite Materials University of Delaware Newark, DE 19716				8. PERFORMING ORGANIZATION REPORT NUMBER	
9. SPONSORING / MONITORING AGENCY NAME(S) AND ADDRESS(ES) Office of Naval Research 100 Alabama St SW Suite 4R15 Atlanta, GA 30303-3104				10. SPONSOR/MONITOR'S ACRONYM(S) ONR	
				11. SPONSOR/MONITOR'S REPORT NUMBER(S)	
12. DISTRIBUTION / AVAILABILITY STATEMENT "Approved for Public Release; distribution is Unlimited"					
13. SUPPLEMENTARY NOTES					
14. ABSTRACT The University of Delaware was awarded Advanced Material Intelligent Processing Center: Next Generation Scalable Lean Manufacturing (N000140911011) in 2009, Program Manager Ignacio Perez. The objective in this grant focuses on design, analysis, process, materials, and automated manufacturing technologies at basic and applied levels of research that will enable a new streamline design process for maritime and next generation lean manufacturing. The research conducted under this grant continues to improve our understanding of the process physics and address manufacturing and material issues as we develop affordable composite molding processes for structures of interest to the Navy. The overarching goals are to develop processing, characterization and automation tools such as (i) process models and simulations (ii) property evaluation methodologies and development of material constitutive models, (iii) imbedded instrumentation for health monitoring and (iv) modular tooling and online sensing and control strategies for the next generation Navy composite structures and applications. The target has been to improve quality, repeatability, tolerances, and affordability through modeling and simulations, process control.					
15. SUBJECT TERMS Composite materials, Processing, Control, Resin transfer molding, Vacuum-assisted resin transfer molding, simulation, modeling					
16. SECURITY CLASSIFICATION OF:			17. LIMITATION OF ABSTRACT U	18. NUMBER OF PAGES 95	19a. NAME OF RESPONSIBLE PERSON John w. Gillespie, Jr.
a. REPORT U	b. ABSTRACT U	c. THIS PAGE U			19b. TELEPHONE NUMBER (include area code) 302-831-8702

Final Report for

***Advanced Material Intelligent Processing Center: Next Generation Scalable Lean
Manufacturing***

Co-PIs

John W. Gillespie, Jr
Center for Composite Materials
University of Delaware
Newark, DE 19716
302-831-8702
gillespie@udel.edu

and

Suresh G. Advani
Center for Composite Materials
University of Delaware
Newark, DE 19716
302-831-8975
advani@udel.edu

Administrative Contact:

Geradine E. Hobbs
Research Office
University of Delaware
210 Hullihen Hall
Newark, DE 19716
302-831-8618
geh@udel.edu

Grant No. N000140911011
Duration of Effort 7/1/2009-5/31/2012

20120927014

Preamble:

University of Delaware was awarded two grants: (1) Advanced Material Intelligent Processing Center: Next Generation Scalable Lean Manufacturing (N000140911011) in 2009 and (2) Advanced Material Intelligent Processing Center: Maritime Manufacturing (N000141010971) in 2010. The program manager for both these grants is Dr. Ignacio Perez. Although these two grants have been assigned separate project numbers, the objective in both these grants is the same and focuses on design, analysis, process, materials, and automated manufacturing technologies at basic and applied levels of research that will enable a new streamline design process for maritime and next generation lean manufacturing. Thus the tasks proposed in the second grant (N000141010971) will seamlessly continue the work completed in corresponding tasks from the previous grant (N000140911011).

The research conducted under these grants continues to improve our understanding of the process physics and address manufacturing and material issues as we develop affordable composite molding processes for structures of interest to the Navy. The overarching goals are to develop processing, characterization and automation tools such as (i) process models and simulations (ii) property evaluation methodologies and development of material constitutive models, (iii) imbedded instrumentation for health monitoring and (iv) modular tooling and online sensing and control strategies for the next generation Navy composite structures and applications. The tasks build on the previously ONR-funded phases of the Advanced Materials Intelligent Processing Center (AMIPC) in which the science base and technology created has been transitioned where possible to industry and government. The target has been to improve quality, repeatability, tolerances, and affordability through modeling and simulations, process design tools, and automation by combining robust sensors and process control. The overall focus of the research conducted under the current two grants builds on our decades of experience in autoclave processing of aerospace components for making high quality and high reliability composites. This "Aerospace at Sea Level" cost effective paradigm continues to develop the science base of the Automated Tape Placement(ATP) process of Oven Cured Vacuum Consolidated Prepregs to manufacture affordable large scale ship structures with hybridization using streamline material, manufacturing and design protocols developed in our research.

This report will summarize the work conducted under the first grant (Advanced Material Intelligent Processing Center: Next Generation Scalable Lean Manufacturing (N000140911011)). The progress and completion stage of various proposed tasks is reported here and continuation of the tasks proposed will be continued in the second grant (N000141010971) for which a no cost extension has been requested until Aug 2014.

Introduction and Background:

The next generation of technological advances in ship design and materials will emerge from the basic science base which can bring about seamless integration of the design, modeling, materials, process physics and structural analysis tools. The proposed integrated approach to design and

analysis, material development and characterization, process modeling, part and mold design, process optimization, and formulation of control actions for automation will allow one to address manufacturing complex and large scale structures with embedded sensors for process, health and life cycle monitoring. This will also remove the barriers to implementation of various functionalities into the structure and the associated manufacturing and structural integrity issues. Virtual manufacturing cell is the key to enabling large scale system integration and lean manufacturing. Finally, validation of various tools and their integration and implementation in an automation environment will ensure feasibility, affordability, and repeatability. These virtual tools will address the goal of *Scalable Lean Manufacturing* by adopting a predictive modeling approach which factors in automation and life cycle monitoring to develop a prototype instead of using cost prohibitive trial and error method.

The emphasis of **Advanced Material Intelligent Processing Center (AMIPC)** for the past few years has been to develop various science-based tools that capture the processing physics and characterize the materials. In this phase of the AMIPC, we are developing the science base models and the material base for Automated Tape Placement (ATP) process which is an attractive process to replace the current hand lay-up technique used to build small scale ships. To advance the ATP process development we decided to focus on oven cured vacuum consolidated prepreg based sandwich structures and had proposed a total of ten tasks which investigate design, analysis, process, materials, and automated manufacturing technologies at basic and applied levels of research and will form the building blocks to enable a new *Lean and Maritime Manufacturing Approach* for Ship Building.

The final ten tasks that were performed adopted the theme of intelligent manufacturing to address design, materials, processing, and variability issues in prepreg processing and create an integrated virtual manufacturing system for Automated Tape Placement (ATP) and Out of Autoclave (OOA) vacuum consolidated and oven cured prepreg sandwich structures.

They are

- (i) Characterization of Epoxy Prepregs and their Composites
- (ii) Void Removal and Migration From Prepregs for ATP and OOA Processes
- (iii) Consolidation Modeling Of Prepregs
- (iv) Modeling And Design of ATP Process
- (v) Scaling of Bagging and New Bagging Concepts for Vacuum Consolidated Oven Cure
- (vi) Smart Prepregs and Composite Materials
- (vii) Dynamic Response and Damage Tolerance of Sandwich Structures Subjected to Impulse Loading from Sea States and Foreign Object Impact
- (viii) Hybridization and Subcomponent Testing and Validation
- (ix) Integration of CFD to Structural Analysis for Streamlining the Marine Design Process
- (x) Virtual Simulation for Cost Reduction

The originally proposed Task (vi) on Modular Molding was integrated in task (iv). Removal of voids from prepregs was considered to be essential in order to obtain void free parts and hence a task (ii) was added to understand and model this phenomenon which will also be continued in the following grant N000141010971

Task IA: Characterization of Epoxy Prepregs and Their Composites: Rheology, Cure Behavior and Void Content

Using tape placement method to manufacture the high speed boat is a process that could take up to 30 days. Thus, this should be taken into account when selecting the materials that will be used in the process, such as out-life time and moisture resistance. Property stability of the prepregs during processing and storage under standard (RT/55% relative humidity) and RT/wet (90% relative humidity) can significantly affect the consolidation mechanism. It is essential therefore to isolate how these hygrothermal conditions affect the several key parameters, such as viscosity, degree of cure and voids.

This effort focuses on characterization of the candidate materials for Out of Autoclave (OOA) prepregs and core-cell (foam) for manufacturing marine vehicles using automated placement method. For prepregs, this study involved rheology, cure behavior of the resin, and void content in the composites cured at different temperatures for 24 hrs. These properties were also evaluated after hygrothermal conditioning of prepregs under RT/55%RH (RT is Room Temperature and RH is Relative Humidity) and RT/90%RH for 30 days. For core- cell material, thermal stability at different processing temperatures was investigated. Materials evaluated in this study are listed in Table 1.

Table 1-Candidate prepregs and foam for evaluated in the current study

Material	Vender	Reinforcement	Thickness	Impregnation Type	Sequence
ST 94-Prepreg	Gurit	0/90 Carbon Fabric	0.37 mm	Partially Impregnated	Dry fabric /Resin
ST 95- Prepreg	Gurit	0/90 Carbon Fabric	1.36 mm	Partially Impregnated	Dry fabric/Resin/Dry fabric/Resin
VTM264 Prepreg	ACG	0/90 Carbon Fabric	0.38 mm	Partially Impregnated	Dry fabric /Resin
Core-Cell P-600	Gurit				

Rheological behavior of the resin

In order to measure the flow behavior of the resin, rheological measurements were performed on the resin film of ST94 and ST95. Two types of tests were conducted; dynamic measurements at 3C/min and isothermal tests at 60C, 85C, 100C and 120C. Also, the effects of hygrothermal conditioning at RT/55%RH and RT/90%RH for 30 days on the viscosity of the resin were investigated. Prior to rheological testing, the resin was dried under vacuum for 24 hrs.

For each test (see Figure 1), the profile of $1/\mu$ (viscosity)-time was generated and the flow number (FN) was calculated using the following equation:

$$FN = \int_0^{t_{gel}} \frac{dt}{\mu}$$

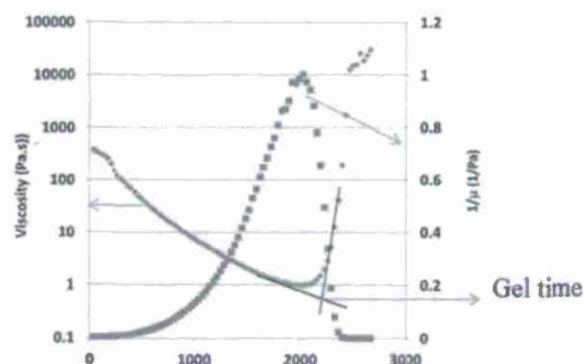


Figure 1- Typical profiles of Viscosity-time and $1/\mu$ (viscosity)-time generated from rheological tests on ST94 and ST95 resin

Table 2 lists the FN and the gel time (t_{gel}) results of dynamic and isothermal tests on ST94 and ST95. Dynamic test results show that ST95 resin tends to higher flow number and shorter gel time compared to ST94 resin. From isothermal test results, FN and gel time for both types of resins (except for ST95 at 85C) show decreasing trends with increased temperature. These results can be useful as guidelines for processing of the composites.

Table 2- Flow number (FN) and gel time (t_{gel}) from dynamic and isothermal tests

	ST94		ST95	
	FN(1/Pa)	t_{gel} (s)		t_{gel} (s)
Dynamic	570	2435	585	2110
Isothermal				
60C	669	60000	639	60000
85C	574	4000	738	4500
100C	563	1500	497	1187
120C	258	365	211	150

Dynamic viscosity experiments were conducted on resin samples treated under conditions of RT/55%RH and RT/90%RH for 30 days and compared to baseline samples (dried samples at RT for 16 hrs.). Results are given in Table 3. From this Table, the hygro thermal conditioning reduced the gel time and flow number. Ambient condition reduced the flow number by 32% for ST94 and 42% for ST95. Due to RT/90%RH conditioning, flow number was decreased by 13% for ST94 and 46% for ST95. Gel time for both types of resins was also reduced due to the conditioning, in which the reduction in gel time for ST95 is significantly higher than that obtained for ST94.

Table 3- Effects of hygrothermal conditioning on flow number (FN) and gel time (t_{gel}) conditioned ST94 and ST95 resin

Cure Temperature	ST94		ST95	
	FN(1/Pa)	t_{gel} (s)	FN(1/Pa)	t_{gel} (s)
Baseline	570	2435	585	2110
RT/55%RH for 30 Days	389	1420	341	1430
RT/90%RH for 30 Days	498	1450	318	160

Fabrication of panels and their characterization

Layers (12"x12") of prepregs were cut and placed in a degassing chamber having (descants material) for 24 hrs. This drying time schedule was estimated from drying tests conducted on the prepregs. Then, a lay-up of 8 layers for VTM 264 and ST94 and 4 layers for ST95 prepregs were proceeded as described in Figure 2. The panels were then cured isothermally at 60C, 65C, 85C, 100C and 120C for 24 hrs. under vacuum pressure.



Figure 2-Panel Fabrication Lay-up

For void measurements, samples of 1" in diameter were cut from the central regions of the cured panels. Samples were then embedded in epoxy, sectioned and polished. The sample was imaged at 10X over 18 middle regions of 0.05" increment and void content was measured. Table 4 shows the void content in the composites cured at different temperatures for 24hrs. Void content for VTM and ST94 show clear decreasing trends with increased temperature. ST 95 type exhibits higher void contents than other types. It was observed that unlike VTM prepreg the ST94 and ST95 prepreg exhibited significant degree of volatiles during drying procedure.

For Tg measurements, DMA-shear tests were conducted on the cured samples at different temperatures. These tests were performed at 5N force and 40 micrometers displacement. Results were depicted in Table 5. Tg shows increasing trends with increased cure temperature.

Table 4-Void content in panels cured at different temperatures for 24 hrs.

Cure Temperature	VTM 264	ST94	ST95
60C	1.46±0.40	Not fully cured	Not fully cured
65C	1.07±0.34	x	x
85C	1.30±0.21	1.56±0.37	~5
100C	1.10±0.34	1.32±0.62	~5
120C	0.92±0.30	1.35±0.81	~5

Table 5-1Hz-Tg measured for prepregs isothermally cured at different temperatures for 24 hrs.

Cure Temperature	VTM 264	ST94	ST95
65C	65.55C	90.34C	
85C	96.74C		95.38C
100C	100.1C	114.8C	100.40C
120C	102.6C	90.34C	99.06C

Effects of hygrothermal conditioning on moisture and void content

An exposure of preregs to ambient or humid conditions allows the moisture to be absorbed by the resin which leads to nucleation of void during the cure process. In this effort, moisture absorption tests were conducted on preregs under RT/90%RH. For these tests, samples were dried under vacuum for 16 hrs. then stored under RT/90%RH condition using an environmental chamber. Moisture content was measured as a function of time. Moisture absorption curves for preregs are depicted in Figure 3. Clearly, moisture gain behavior for preregs shows two-states of saturation. Moisture gain in the 2nd saturation state can be estimated as 2-3.5% for ST 94 and ST 95 preregs, which is comparable to moisture content of ~3.15% measured for ST film under same condition. VTM samples show 4-5% moisture content in the 2nd saturation state.

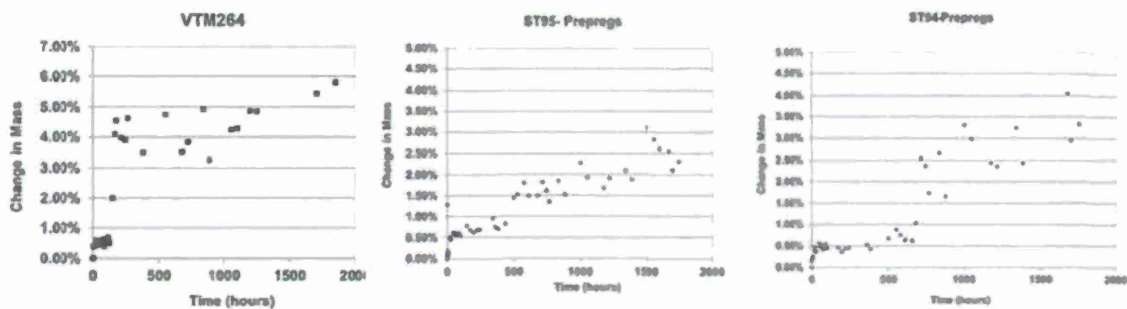


Figure 3: Moisture absorption behavior measured for preregs under RT/90%RH for 2000 hrs.

Void measurements were performed for the panels isothermally cured at 85C for 24 hrs., where the preregs were conditioned at RT/55%RH and RT/90%RH for 30 days prior to the cure procedure. Table 6 lists the void content for as received, dried (degassed for 16 hrs. using the bell jar), conditioned at RT/55%RH and RT/55%RH for 30 days. Obviously, degassed samples show higher void content than as received samples. This may be due to trapped gasses, which is most likely due to generated volatiles during the drying procedure under vacuum. It needs to be noticed that during the drying procedure ST95 preregs experienced thickness enlargement due to generated gases between the two layers. These trapped gases were arrested in place leading to high void content (see Figure 4).



Cured as received



Dried under vacuum for 16 hrs using degassing chamber and cured



Conditioned at RT/55%RH for 30 days and cured

Figure 4- Cross-section of cured ST95 preregs at 85C for 24 hrs.

With respect to void content values of as received samples, treated samples under ambient conditions exhibited an increase in the void content by a factor of ~1.63 for VTM and ~1.74 for ST94 and ST95 samples and conditioned samples at RT/90%RH increased the void content by factor of 4.7 for VTM, 4.4 for ST94 and 17.7 for ST95. During conditioning the resin in the prepregs can experience partial cure causing the moisture to be trapped by cured resin leading to void formation during final cure.

Table 6- Void content measured for prepregs subjected to different conditions and then cured at 85C for 24 hrs.

Condition	VTM 264	ST94	ST95
As Received	0.90±0.21	0.90±0.21	1.23±0.37
Dried (Degassed for 16 hrs.)	1.80±0.41	1.53±0.31	~5
RT/55%RH for 30 Days	1.47±0.46	1.57±0.36	1.57±0.36
RT/90%RH for 30 Days	4.22 ± 1.95	3.92 ± 0.83	15.89 ± 6.42

In this effort, DSC measurements were conducted on the in-situ resin to track the enthalpy for as received, dried and conditioned material at RT/55%RH and RT/55%RH for 30 days. Tests were carried out applying 5C/min heating rate. Results are given in Table 7. From this Table, the hygrothermal conditioning for 30 days caused the resin of the prepreg to cure with a degree of ~70% for VTM, ~53% for ST94 and ~64% for ST95.

Air Evacuation from the panel

To obtain high quality of composites, the lay-up of OVB prepregs should be free of air during the curing process. In this effort, the effect of air evacuation from the prepregs on the void content and thickness was investigated. For these tests, two panels (each consisting of 12"x50"eight layers) were prepared. One was cured isothermally at 85C for 16 hrs. under vacuum and the other one pre-evacuated air and then isothermally cured at 85C for 16hrs under vacuum

Table 7- Enthalpy (J/g) measured for prepregs subjected to different conditions and then cured at 85C for 24 hrs.

Condition	VTM 264	ST94	ST95
Neat resin	352	258	328
As Received	352±5	249±2	298±16
Dried (Degassed for 16 hrs.)	334±9	238±14	297±10
RT/55%RH for 30 Days	111±0.23	120.9±0.10	123±0.20
RT/90%RH for 30 Days	106±1.56	121±0.15	124±0.28

For both panels, the void content, thickness over the length of the panel was measured. Void content results for both types of panels are shown in Figures 5 and 6. Pre-evacuated panels show relatively constant void content over the length, but the panel in which air was not pre-evacuated shows a higher void content in the middle of the panel and lower void content near the vacuum vent.

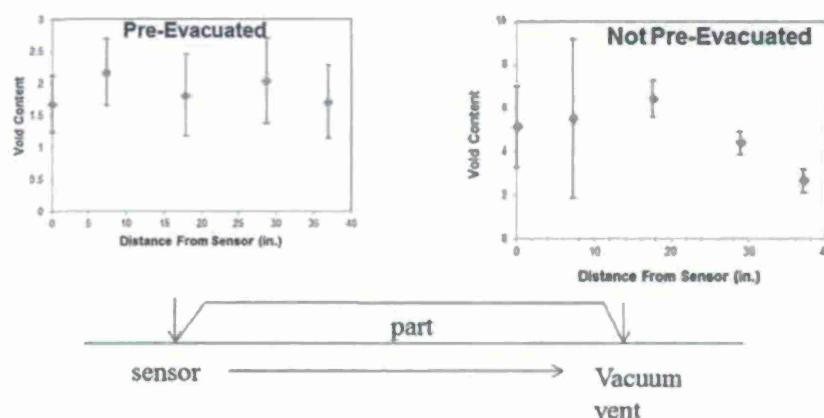


Figure 5- Void content as measured over length for the panels with and without air evacuation procedure prior to cure

Thermal stability of the core-cell P600

For high speedboat manufacturing, it is essential to know the dimensional stability of the core-cell during processing. In this effort, using LVDT's the real time thickness at different temperatures (RT, 40C, 60C and 80C) was measured, while the samples were under vacuum for 24 hrs. The 8"x8" core-cell samples size was used. From the results, the reduction in thickness of the foam P600 during heating cycle was ~0%, 4-5% at 40C and 60C. During heating cycle the foam showed compression up to 8% then expansion after 2 hrs. (densifying effect) reaching 5% change after 20hrs. Expansion behavior was due to the pressure increase in the cells of the foam. These results indicate the unstable behavior of the foam properties at 80C.

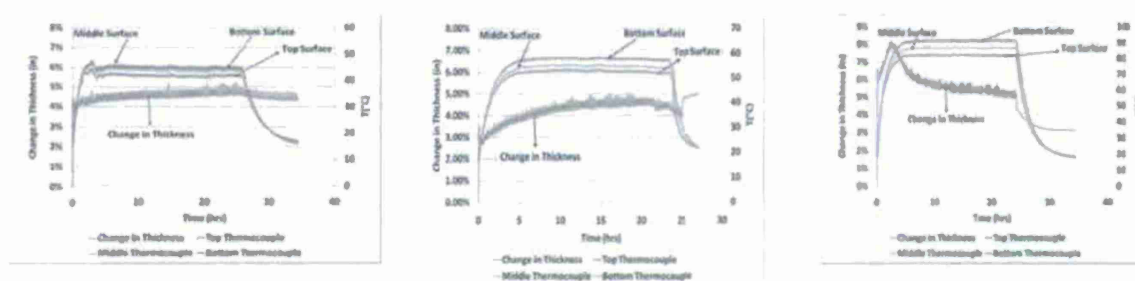


Figure 6: Dimensional stability of the core-cell P600 during heating cycles at 40C, 60C and 80C under vacuum for 24 hrs.

Summary and Conclusions

- 1) From isothermal test results, the resin of the ST94 prepregs exhibited decreasing trends of flow number (FN) and gel time with increased temperature. FN and gel time for both types of resins (ST94 and ST9) were significantly decreased after hygrothermal conditioning. For example, RT/90%RH conditioning reduced the flow number by 13% for ST94 and 46% for ST95.

- 2) Prepregs of VTM 264, ST94 and ST95 were isothermally cured at different temperatures (60-120C). Void content and Tg from DMA were measured for cured samples. From DMA results, Tg of the samples showed increasing trends with increased cure temperature. Void content in VTM and ST94 samples exhibit clear decreasing trends with increased temperature. ST 95 samples cured at all temperatures showed always higher void contents (~5%) than other types (1%-1.4%).
- 3) Effects of hygrothermal conditioning (RT/55%RH and RT/90%) for 30 days on degree of cure and void were investigated. Hygrothermal conditioning caused the resin of the prepreg to cure with ~70% for VTM, ~53% for ST94 and ~64% for ST95. Prepregs treated under ambient conditions exhibited an increase in the void content by a factor of ~1.63 for VTM and ~1.74 for ST samples and conditioned samples at RT/90%RH increased the void content by factor of 4.7 for VTM, 4.4 for ST94 and 17.7 for ST95.
- 4) From the study on core-cell P600, it was observed that the dimensions of the core-cell exhibited unstable behavior at 80C under vacuum. \

Task IB. Characterization of Epoxy Prepregs and Their Composites: Permeability Evaluation

This effort evaluates the relationship between the processing conditions of Out Of Autoclave (OOA) prepreg fabrication and laminate quality, in particular the ability of the material to properly evacuate to full vacuum in order to compact the laminate before and during curing and to ensure low void content laminates. In pre-impregnated fabric materials it is especially important to provide pathways for gas entrapped during lay-up or created during vacuum or temperature application to escape to minimize final porosity. In large structures, the time component for air evacuation can become critical. For one, large laminate stacks of low-permeability prepregs demand rather long evacuation cycles to remove all entrapped air before they can be cured into void-free laminates. Secondly, large lay-ups potentially require long periods of lay-up work itself, in which the resin components are subjected to ambient conditions and undergo partial curing.

For the purpose of establishing a quality baseline, the void contents of two 50" long laminates were determined at several locations. One 8-layer stack was subjected to application of vacuum pressure only during the curing cycle; the second one was pre-evacuated/consolidated for 24h hours prior to cure. In both instances, the vacuum port was connected on one side, while a vacuum sensor was connected on the opposite side, effectively creating a one-dimensional in-plane flow path of 50" length. The vacuum pressure on the opposite side of the vacuum port was recorded during the 24 hour 185°F cure cycle.

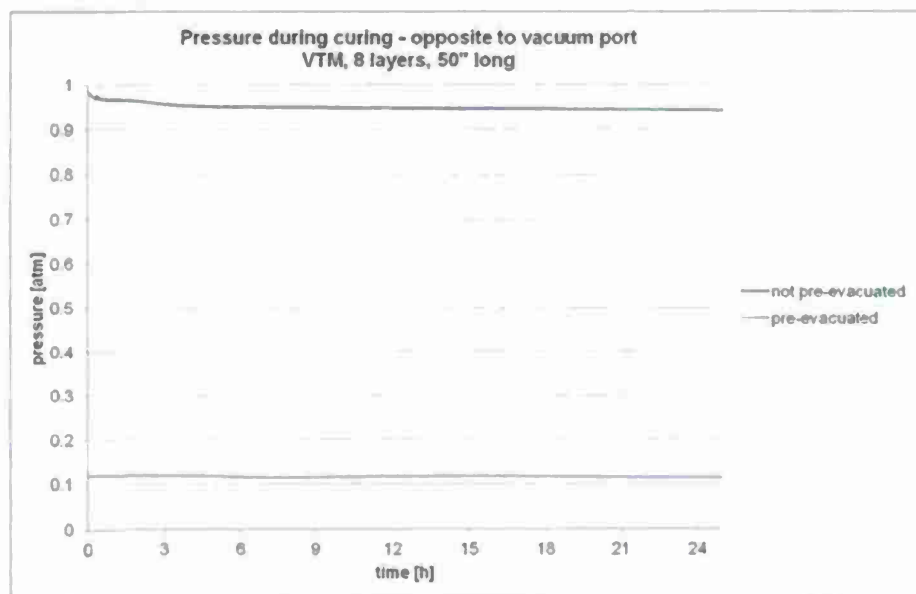


Figure 7: Pressure change at the inlet port during curing

As shown in Figure 7 above, the pressure stayed at the level reached during pre-evacuation (0.12 atm) for the respective panel. In case of the immediate cured panel, the vacuum level opposite to the vacuum port (inlet) barely changed over the curing period. This suggests that upon

subjecting the lay-up to cure temperature, evacuation pathways were immediately closed off by the viscous resin and extraction of trapped air and volatiles was made impossible.

Figure 8 illustrates the distribution of void content along the length of the cured panels. It clearly shows the even distribution of ~2% voids in the pre-evacuated laminate. The distance from the vacuum port did not significantly affect the level of air evacuation. It is also shown that the immediate cured lay-up resulted in a significantly higher void content overall and an uneven distribution of up to ~10% in particular. Assuming even air entrapment before the heating phase, it is likely that a certain amount of air flow over the length did take place in the beginning, but the viscous resin started penetrating the dry regions quickly and blocked off majority of air evacuation pathways in the center and towards the vacuum port.

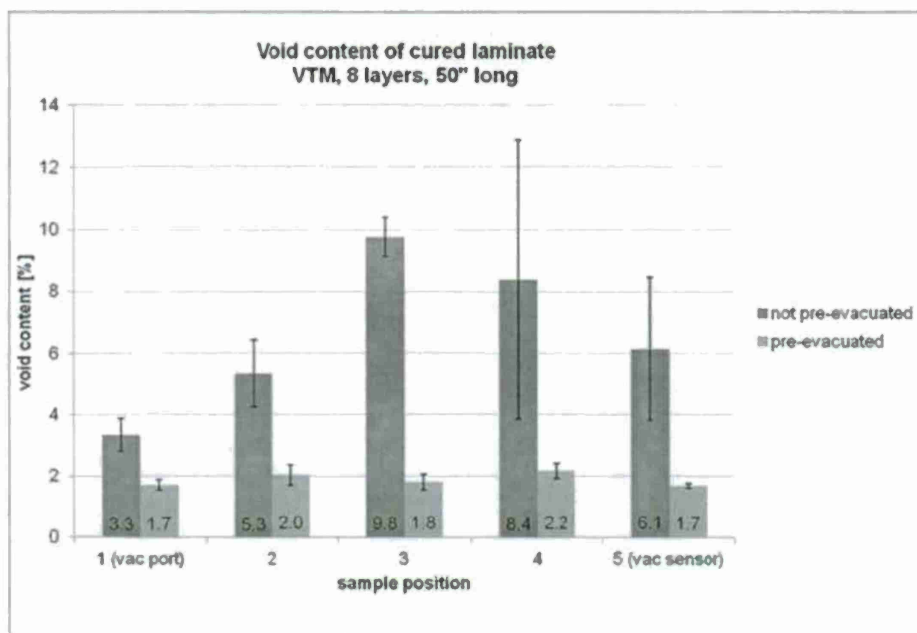


Figure 8: Void content of cured laminates with increasing distance from vacuum port

This initial experiment shows clearly the need for evacuating the prepreg lay-up before subjecting it to the cure cycle in order to assure evenly distributed low void contents in the laminate.

Effects of environmental conditioning

Further studies were carried out to investigate the effect of environmental conditioning on in-plane air evacuation (linked to in-plane permeability of the lay-up). Three different prepreg materials were tested in four different states of conditioning. The ST94 and ST95 are partially impregnated prepreps while VTM is a fully impregnated system. Single layers of prepreg were evacuated in-plane as received, dried, after 30 days under room temperature and after 30 days at room temperature and 90% humidity.

In this experiment, 12" by 12" layers of prepreg were connected to a vacuum source on one side and a vacuum sensor placed on the opposite side. The vacuum pressure was recorded once vacuum was applied to one side and the developing profile observed.

Figure 9 shows the differences in time needed for air evacuation between different materials and in as received condition. This is mainly due to differences in fiber architecture and resin distribution in the prepreg and ultimately the air permeability of the prepreg material. The evacuation time to 0.1atm will be used as point of comparison. It can be seen that VTM material takes significantly longer to evacuate to that level (ST94: 466s; ST95: 290s; VTM: 6300s). In-plane permeability is significantly higher in the partially impregnated prepreps as the dry fiber preform carries most of the air flow while the fully impregnated prepreg material relies on the pathways within the interface of two adjacent layers.

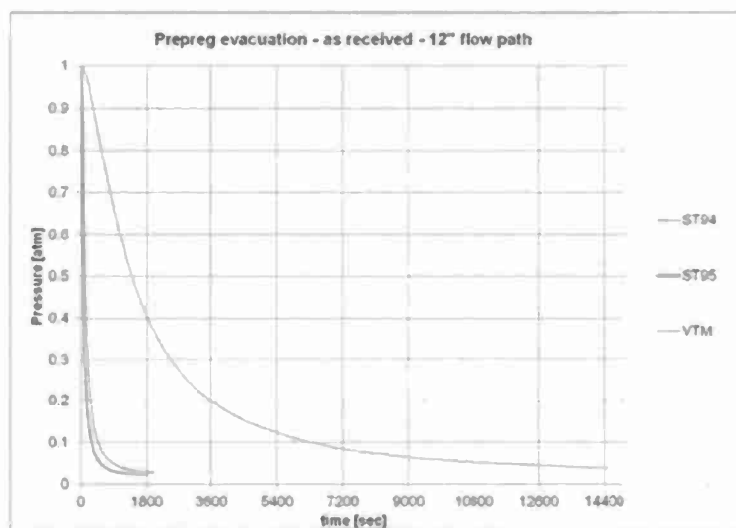


Figure 9: Pressure profile over time for prepreg material - as received

Figure 10 compares the air evacuation of the ST94 and ST95 materials after drying. The evacuation time is greatly reduced by approximately 50% and 30% respectively, and for VTM the reduction was 62%.

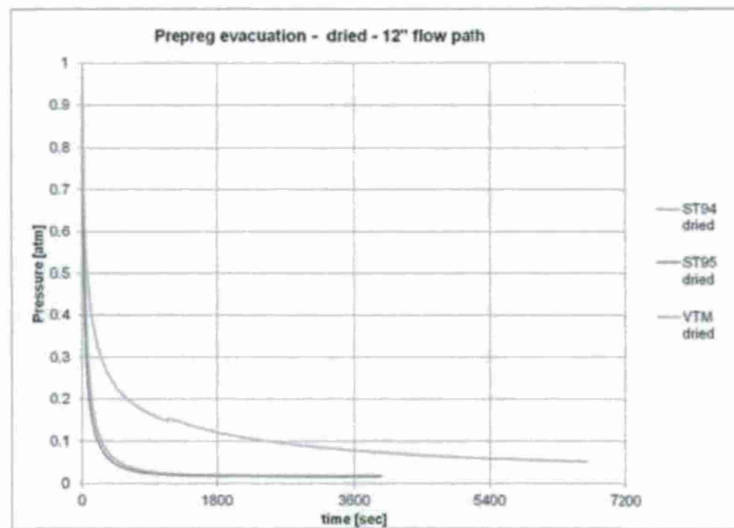


Figure 10: Pressure profile over time for prepreg material - dried

Conditioning at 23°C and 55% RH for 30 days caused an increase in evacuation time to 0.1atm for ST94 by 50% and for ST95 by 200%. VTM showed a much faster initial slope but never reached the 0.1atm threshold as shown in Fig. 11. This indicates that evacuation paths were most likely blocked by the resin.

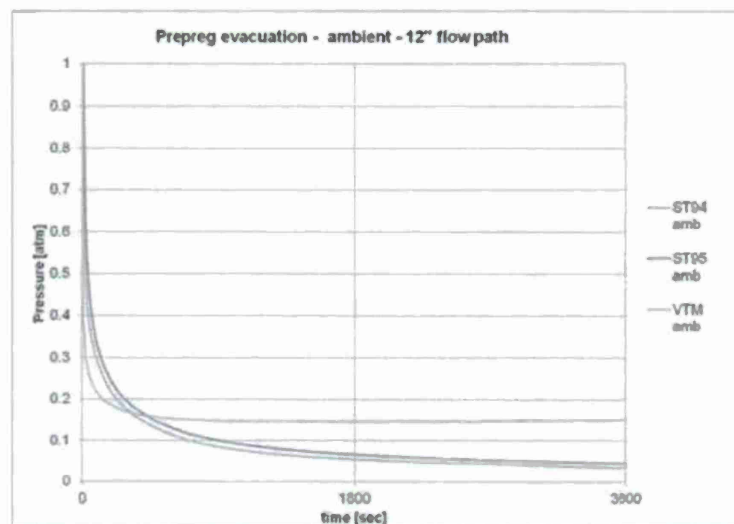


Figure 11: Pressure profile over time for prepreg material - 30 days at room temperature

For samples conditioned at 23°C and 90% RH for 30 days, thresholds of 0.1atm were never reached. It was observed that conditioning lead to much reduced resin viscosity (dilution by moisture), which increased resin flow resulting in faster blocking of evacuation pathways as can be seen from Fig. 12.

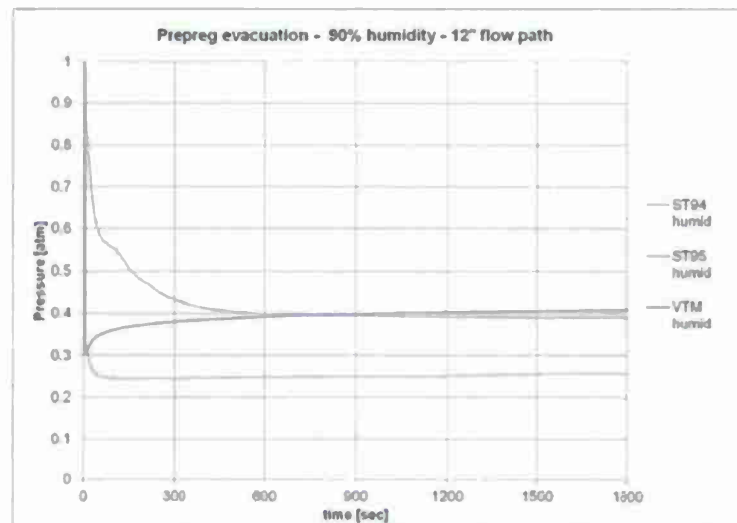


Figure 12: Pressure profile over time for prepreg material - 30 days at room temperature and 90% humidity

Effects of environmental conditioning on void content

In this effort the void content in cured prepregs after conditioning (23°C, 55% and 90% RH for 30 days) were measured. Results were compared to the as received samples. Environmentally conditioned samples exhibited an increase in the void content by a factor of ~1.63 for VTM and ~1.74 for ST94 and ST95 samples and conditioned samples at RT/90%RH increased the void content by factor of 4.7 for VTM, 4.4 for ST94 and 17.7 for ST95. During conditioning the resin of the prepregs can experience partial cure causing the moisture to be trapped by cured resin leading to void formation during final cure.

Through-thickness permeability

Most recently air evacuation experiments through-thickness (related to through thickness permeability) were conducted. This parameter plays a crucial role in predicting the final properties of large scale prepreg structures. Thus air evacuation times for different layer counts of ST94 have been recorded. In these tests air flow was guided through the thickness by placing a vacuum port on top and a vacuum sensor on the bottom. To facilitate even flow over the 10" by 10" sample area, breather cloth (high permeability) was placed between prepreg and vacuum port/sensor on both top and bottom. To eliminate in-plane flow in or around the prepreg the layers were also sealed with sealant tape on the edges.

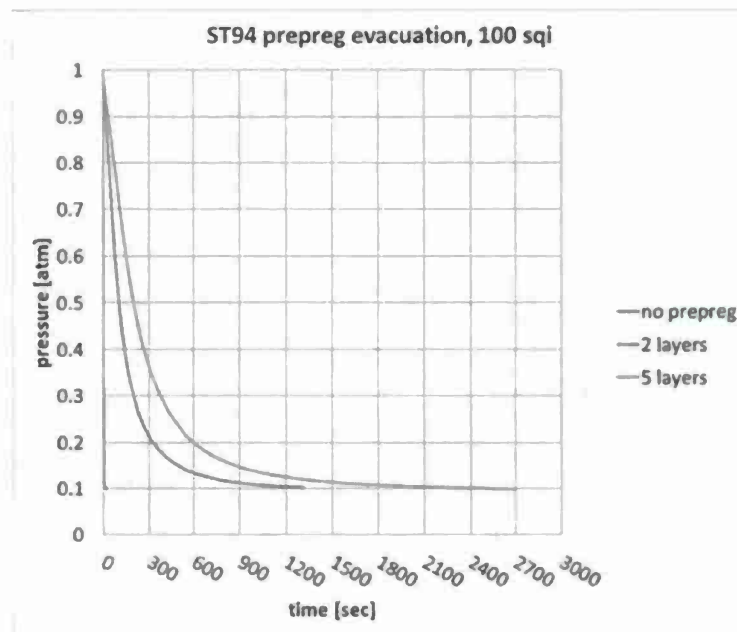


Figure 13: Pressure profiles for through thickness air evacuation test

Figure 13 shows the increased evacuation time with increasing number of layers and thickness. This reduction in flow rate is expected according to Darcy's Law. A modified experimental setup to include real time flow rate measurements is in progress. This method of keeping the pressure gradient constant and recording the flow rate will make it easier to calculate permeability values for the through thickness direction (k_{zz}).

Task II: Void Removal and Migration from Prepregs for Tape Placement and Out of Autoclave Processes

Introduction and Background

The elimination of defects such as voids is critical for the production of high quality composite parts. Voids are defined as areas of high matrix porosity that result from trapped or formed volatile gases during processing. Many high performance composites require void content to be less than one to two percent to prevent degradation of mechanical properties. Voids can degrade the mechanical properties of composites via encouraging microcracking due to void initiated stress concentrations (i.e. premature fatigue failures). It is desirable to link the formation, growth and movement of voids to process modeling and simulation for more realistic processing knowledge and prediction. Thus, any methodology that can be formulated to understand the formation and movement of voids and thereby control their behavior is valuable for increased cost savings and part quality.

Current Void Mitigation Strategies

During composites processing, manufacturers typically resort to three methods to reduce overall void content during processing: (1) degassing or heating the resin prior to infusion (i.e. LCM); (2) increasing processing time to allow voids to collapse or escape and (3) increasing consolidation pressure and temperature to compress the voids (i.e. OOA). Figure 14 displays a schematic that illustrates the highlighted void mitigation methods. Degassing resin involves applying a vacuum to a container of resin, which causes volatile gases within the resin to be drawn out. Preheating the resin requires elevating the temperature of the resin to decrease its viscosity and thus improve the probability of successful void migration during composite processing. The manufacturing infrastructure (i.e. molds, tubing, etc.) must use high temperature materials, which can increase overall manufacturing costs significantly. Also, elevated temperature can prematurely initiate resin curing. Increasing the resin infusion time allows for a longer time for voids to migrate out of the composite preform during processing. Operators may have to allow for long times for void removal, which can slow down production and increase material waste. Use of high pressure to collapse voids requires high pressure equipment and is not usually successful in completely eliminating them. Thus, there exists a need for ways to intelligently mitigate voids during composites manufacturing.

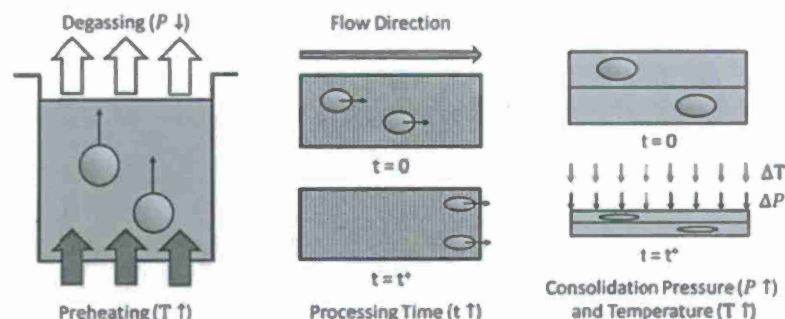


Figure 14. Schematic of common void mitigation methodologies

Approach

New Void Mitigation Strategy via Targeted Applied Vibrations

Trapped voids are observed in many different composite processing methods, such as liquid composite molding (LCM) or out-of-autoclave (OOA) prepreg processing. When voids are not successfully removed from a composite layup during processing, they can be trapped between fiber tows or inside a fiber tow. The application of external stimulus such as a pressure or temperature gradient is necessary to induce voids to move out of the entrapped zone. Thus, it is desirable to create an external stimulus to dislodge trapped voids to promote void migration and increase the probability that they can escape. There have been studies in which mold has been vibrated to break bubbles or dislodge them during mold filling [1, 2]. For this work, we investigate the use of low frequency vibrations (i.e. 1 – 15 Hz) to provide a targeted stimulus on selected areas of a prepreg preform. It is believed that these vibrations can change the void morphology such that local resistance to flow is reduced and thus voids can become dislodged from entrapping fiber regions and successfully migrate in a flowing fluid stream. Figure 15 highlights this concept schematically. One can observe in the top half of the figure that voids present in the prepreg material tend to migrate to vacuum pathways independently before the resin cures, otherwise the voids will stay trapped in the composite after cure and lead to premature part degradation. The hypothesis is such that with the application of vibrations, void migration from the layup during processing will be expedited. In addition, it is desirable to have the ability to apply vibrations in a targeted and localized manner to induce bubble movement.

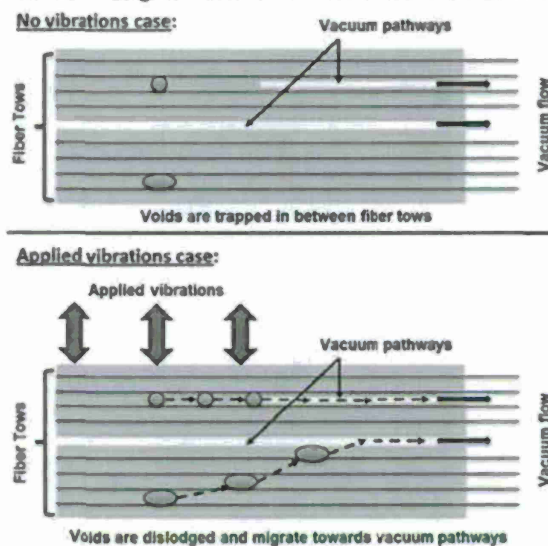


Figure 15. Void mitigation concept schematic for prepreg processing.

Techniques for Applying Vibrations

In the past, resin flow manipulation during resin infusion into a mold containing fabrics has been successfully addressed in Liquid Composite Molding processes [3-7]. Of these, two processes Vacuum Induced Preform Relaxation (VIPR) and Magnet Induced Preform Relaxation (MIPR) are potential candidates that will be explored to introduce repetitive localized disturbance in the

flow field in the vicinity of the voids. The goal of MIPR and VIPR is to identify regions without resin and create a pressure gradient to induce the resin to flow there. This is accomplished by relieving the external pressure on the fabric which relaxes the fiber preform underneath the bag in that region. The relaxation of the fiber preform causes the local permeability of the fabric to increase, thus making it easier for the resin to infuse that region. In VIPR, differential vacuum is created across the region of interest, whereas in MIPR, the bag is physically lifted to relax the preform. Since both processes have the ability to manipulate the resin flow front in real time, it is hypothesized that each process can also be adapted to induce and dislodge trapped voids via applied targeted vibrations (repetitive application of VIPR or MIPR in the region of interest) in composite processes such as LCM and OOA prepreg processing.

Experimental Goal

It is the primary goal of this work to investigate the use of MIPR to provide targeted and localized vibrations to OOA prepreg layups that have been placed under vacuum to remove the air from the system. The approach is to provide vibration energy into any trapped air or volatiles voids that are trapped in the layup. These vibrations will be used to dislodge trapped voids to migrate towards air removal pathways available in the partially cured prepreps as shown in Figure 15 before the layup is placed in an oven for consolidation and cure. In this work, we demonstrate the concept of MIPR for void mitigation in a model system as a prelude to implementation in oven based prepreg processing.

Experimental Setup

This work will explore the feasibility of using MIPR repetitively on a model system to dislodge trapped air bubbles into high permeability fluid pathways and investigate the sensitivity of the frequency and duration of MIPR application to dislodge the bubbles. Figures 16 and 17 show the experimental setup. The model setup uses dry fabric layers that are saturated with a simulated resin. The resin continues to flow out of the vent due to the application of vacuum as in a VARTM process. Voids are introduced underneath the saturated preform layup by removal of the inlet tube for a specific amount of time from underneath the setup. The presence of resin before the introduction of air simulates prepreg layups (i.e. resin and fibers with no moving flow front). Distribution media is placed on the layup located after the steel insert to model the permeable pathways within a partially impregnated prepreg to remove the air from the system. The introduced voids represent regions of trapped air or volatiles within a prepreg. If one can dislodge the voids from the model system towards the distribution media (air removal pathways), one can claim that vibrational energy will be able to induce void movement driving them towards evacuation pathways during prepreg layup before consolidation and cure in an oven.

The setup consists of two layers of plain weave carbon fiber and a clear distribution media. The distribution media is cut such that it spans the length just after the steel inert only as shown in Figure 16. The assembly is vacuum bagged and the simulated resin (corn syrup) is allowed to saturate the preform and the distribution media. This allows the resin to bleed through the vent creating continuous flow. Then voids were introduced and MIPR was applied at different frequencies from 1-15 Hz to induce void dislodging from underneath the preform towards the

distribution media as schematically depicted in Figure 16. The vibration amplitude is controlled via the piston pneumatic pressure at 207 kPa and the piston stroke length of 2.54 cm.

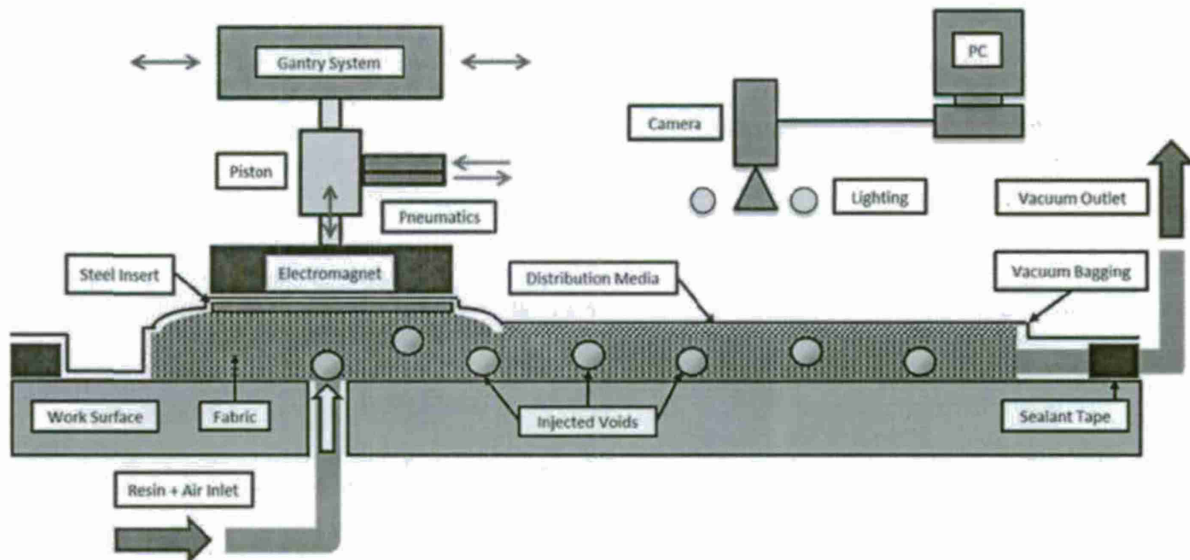


Figure 16. Experimental set-up for flow visualization of void migration due to MIPR application.

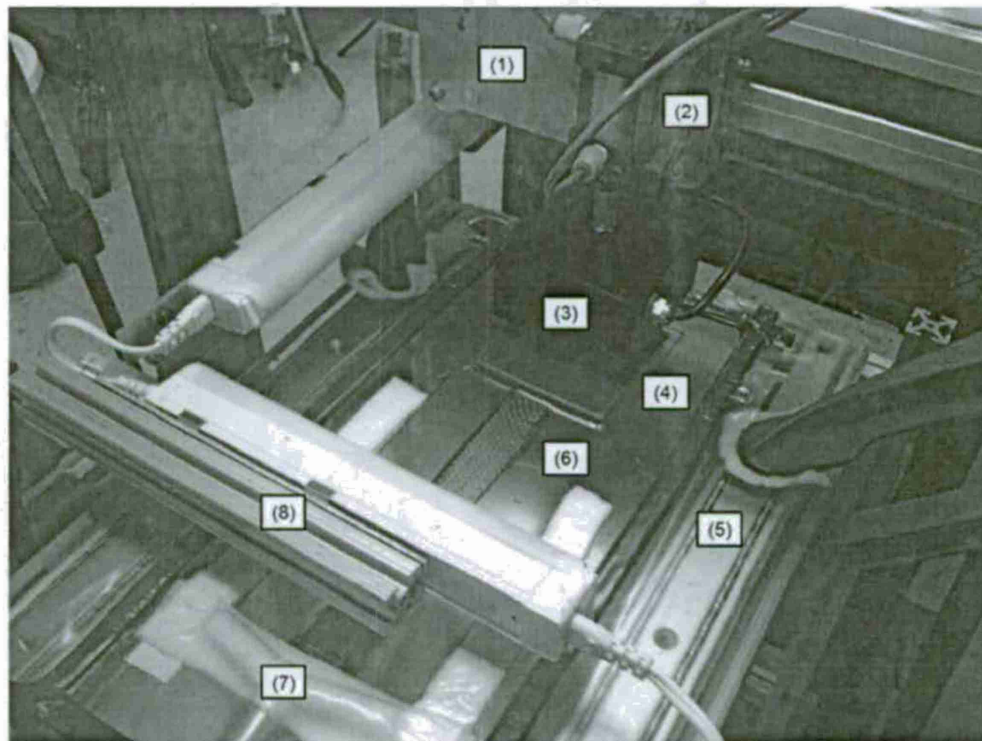


Figure 17. Experimental setup photograph showing preform layup and MIPR assembly with: (1) gantry support, (2) piston, (3) electromagnet, (4) steel insert with inlet and carbon fiber, (5) work surface, (6) carbon fiber and distribution media, (7) vacuum vent, (8) lighting.

The experimental schematic in Figure 17 shows voids being visualized via a camera system connected to a PC either from the top or the bottom of the work surface. The experiment permits voids to be tracked in real time with MIPR actions. Thus, one can quantify how modification of process variables affects the tendency for voids to migrate through the distribution media. The voids that are dislodged from the fabric can be seen by the flow visualization system and the time they take to appear in the distribution media from the injection time is recorded. This time interval is considered as the time for the voids to enter the vacuum pathways at that particular MIPR frequency can be quantified. With MIPR, one needs to apply a sinusoidal displacement to the pneumatic piston in order to introduce vibrations to the system.

An image processing scheme was developed to interrogate void movement and migration images and characterize them via void area fraction calculations. Note that in order for images to be processed properly, sufficient contrast is necessary to distinguish void areas from the background. We chose plain weave carbon fiber + dyed corn syrup as our test material system, because it can provide adequate contrast for distinguishing voids during imaging. Florescent lighting has been rigged orthogonally oriented to the viewing area to further enhance contrast. In addition, void migration is observed through clear distribution media, because the clear distribution media becomes translucent once infused with the corn syrup mixture and does not obstruct the view. Note the setup is designed such that the width of composite samples matches the viewing area of the camera system. The magnified viewing area of the camera system is 640 x 480 pixels, which corresponds to ~2.7 cm x 2 cm on the setup. This viewing area was positioned to be halfway between the edge of the steel insert and the vent. By matching the width of the viewing area to the sample width, one can image all the voids that travel lengthwise from the resin gate to the vent. This provides a 1D observational sense with respect to void migration. The camera viewing area can be modified such that a 2D observation sense can be viewed to track the 2D void migration through the distribution media.

Results and Discussion

Figure 18 displays a time lapse series of photographs of a large void that dislodged and migrated into the distribution media and was evacuated through the flow field. For this example, the resin flow is due to pressure difference of atmospheric condition at the inlet and vacuum at the vent. The MIPR action is applied at the rate of 10 times per second creating an applied vibration of 10 Hz. The viscosity of the corn syrup/water mixture was measured with a viscometer at 126 mPa s. Figure 18 shows the propagation of a void from left to the right of the viewing area. The void is introduced at the bottom of the preform which migrates into the distribution media pathway and is convected by the fluid. Note that the width of the images corresponds to the total width of the material sample such that all voids that move through the distribution media length are visible in the image area. From Figure 18, one can observe that it took 65.6 s for the void to enter the distribution media from the time it was injected into the bottom of the preform.

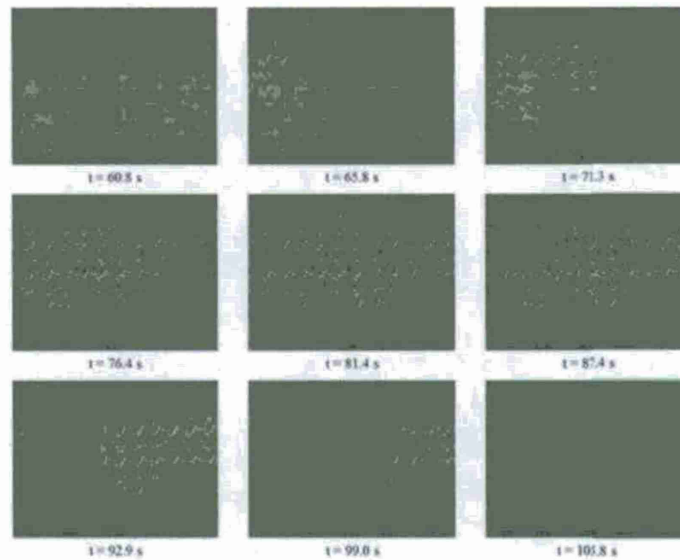


Figure 18. An experimental example of void migration at 10 Hz of vibration. The bright area in the distribution media is the void migrating from the left to right towards the vent.

Using our image processing capabilities we can also generate void area statistics of the images in Figure 18 as shown in Figure 19. The software allows one to distinguish void and resin areas with time. This data is useful for determining void size, void arrival time in the distribution media and void velocities as a function of MIPR frequency, fluid flow velocities and resin viscosity. For this work we limit our investigation to measuring void arrival time from the bottom of the preform into the distribution media (which represent the vacuum pathways) as a function of MIPR frequency and compare it to baseline case when no MIPR is applied.

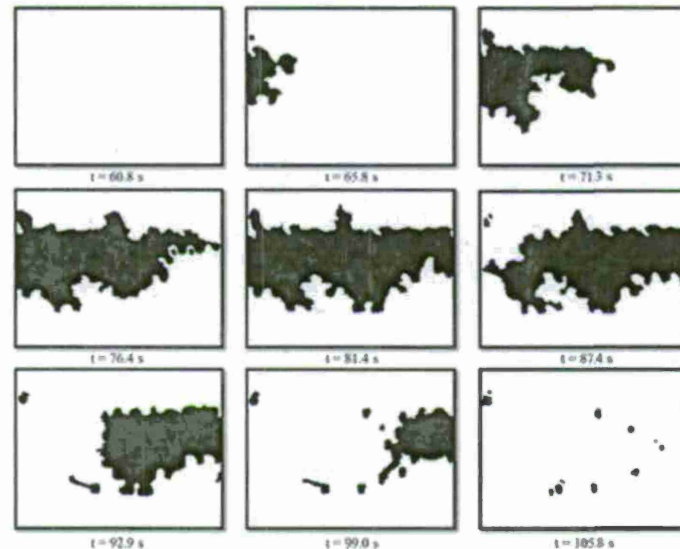


Figure 19. Void contrast images from Figure 18 allowing one to quantify the void migration.

Figure 19 shows the results in which the time it takes for introduced voids to arrive into the camera viewing area is presented as a function of the MIPR frequency. This time indicates the

effectiveness of applied vibrations in promoting void migrations within the fabric compared to the baseline case of no applied vibrations. Here, the average of five trials is plotted for each frequency along with standard deviation error bars. The layup and resin batch were kept the same for every test at every frequency for experimental control. Note, the viscosity for this resin batch was measured at 82.5 mPa s. For these trials, voids were injected by removing the inlet tube from the resin bucket for 2.0 seconds. Hence we expect the initial void diameter to be of similar magnitude.

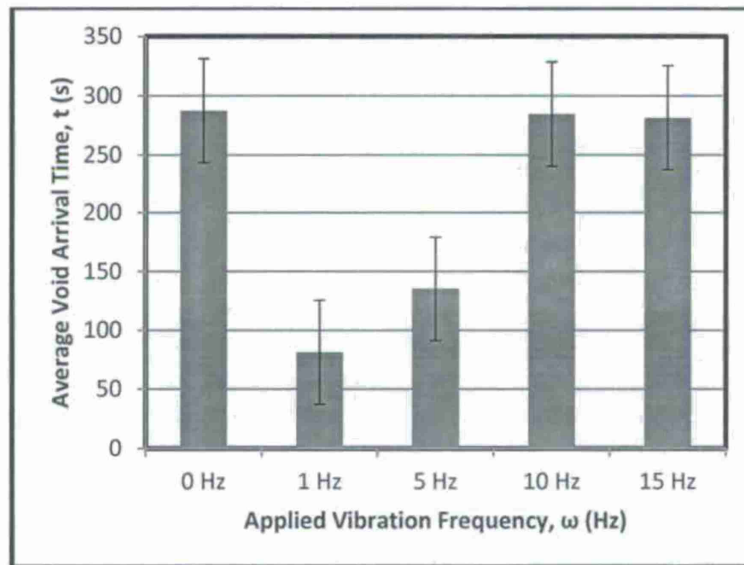


Figure 20. Void dislodgement time with MIPR as a function of applied vibration frequency.

Conclusions *and Path Forward*

The overall goal of this work was to explore and understand the use of repetitive preform relaxation to dislodge trapped voids during evacuation of air after prepreg layup before oven consolidation and cure. A flow visualization set-up was created for a model experiment to quantify the effect of vibration frequency on the time it took to dislodge the bubble from the bottom of the preform into the evacuation pathway represented by the distribution medium. From the model experiments, it was observed that MIPR changes the fabric permeability locally with each piston displacement cycle. It was observed that when the electromagnet is fully displaced downward, it compacts the preform and effectively reduces permeability by closing the gaps between the fibers. When the electromagnet is fully displaced upward, there is maximum preform relaxation and resin rushes to the site. The displacement cycling creates an effective pumping action that acts as the primary driving force and accelerates the void dislodging.

Based on the results of Figure 20, it was observed that the void arrival time is significantly reduced with vibration application of 1 – 5 Hz. With increasing frequency from 5 to 15 Hz, the applied vibrations do not seem to reduce the void removal times as compared to the no vibration case. This suggests that there is an optimal frequency range that promotes void migration. During applied vibrations, the void oscillates back and forth, each cycle increasing its displacement eventually reaching the distribution media which provided the pathway to escape. Thus, the lower frequencies were more effective in promoting void migration, because they created void

oscillations with the largest displacements moving the void towards the distribution media in less time.

Future work is focused on the study of viscous bubble migration through porous media applied to OOA prepreg composites processing. An experimental setup and computational model are in development to investigate what material and process parameters can be tailored for optimal void migration effects. Future experiments and computational modeling will seek to understand how to find these optimal values for different processing scales. Overall, the use of preform relaxation processes remains promising for void mitigation during composites processing.

References

1. J. Muric-Nesic, P. Compston, N. Noble, Z.H. Stachurski, Effect of low frequency vibrations on void content in composite materials, *Composites Part A: Applied Science and Manufacturing*. 40 (2009) 548-551.
2. J. Muric-Nesic, P. Compston, Z.H. Stachurski, On the void reduction mechanisms in vibration assisted consolidation of fibre reinforced polymer composites, *Composites Part A: Applied Science and Manufacturing*. 42 (2011) 320-327.
3. Alms, J. B., Catry, A., Glancey, J. L., & Advani, S. G., (2009). Flow Modification Process for Vacuum Infusion Using Port-Based Resin Flow Control. *SAMPE JOURNAL*, 45(2), 54-63.
4. Alms, J. B., Flow manipulation and control methodologies for vacuum infusion processes, University of Delaware, 2011.
5. J.B. Alms, S.G. Advani, J.L. Glancey, Liquid Composite Molding control methodologies using Vacuum Induced Preform Relaxation, *Composites Part A: Applied Science and Manufacturing*. 42 (2011) 57-65.
6. J. Alms, S.G. Advani, Simulation and experimental validation of flow flooding chamber method of resin delivery in liquid composite molding, *Composites Part A: Applied Science and Manufacturing*. 38 (2007) 2131-2141.
7. J.B. Alms, J.L. Glancey, S.G. Advani, Mechanical properties of composite structures fabricated with the vacuum induced preform relaxation process, *Composite Structures*. 92 (2010) 2811-2816.
8. Rasband, W.S., ImageJ, U. S. National Institutes of Health, Bethesda, Maryland, USA, <http://imagej.nih.gov/ij/>, 1997-2011.
9. S. G. Advani, E. M. Sozer, *Process Modeling in Composites Manufacturing*, New York: Marcel Dekker, Inc., 2003.
10. V. Frishfelds, T.S. Lundström, A. Jakovics, Bubble motion through non-crimp fabrics during composites manufacturing, *Composites Part A: Applied Science and Manufacturing*. 39 (2008) 243-251.
11. T. Sadiq, Experimental investigation of transverse flow through aligned cylinders, *International Journal of Multiphase Flow*. 21 (1995) 755-774.
12. K. Kang, K. Koelling, Void transport in resin transfer molding, *Polymer Composites*. 25 (2004) 417-432.
13. J.J. Gangloff Jr., R. Readdy, and S.G. Advani, "The Effects of Targeted Applied Vibrations to Promote Void Reduction during Composites Processing", *SAMPE Conference & Exposition*, Baltimore, MD. May 21-24, 2012.

Task III: Consolidation Modeling Of Prepregs under Tape Placement

Introduction and Background

The objective in this task was threefold:

1. Provide a tool to characterize changes in resin distribution of partially impregnated prepregs during consolidation, including *partial* consolidation.
2. Obtain analytic tools to predict these changes under varying process parameters, such as temperature or applied loads.
3. Map the prepreg air permeability to the resin/reinforcement configuration. This would allow one to obtain the allowable processing window that will maintain prepreg sufficiently permeable to evacuate volatiles for the final consolidation.

To achieve these objectives, experimental technique was developed to track the resin progression as the prepreg is subjected to roller pressure. A set of experiments was conducted to characterize consolidation of ST94 prepreg under different load and temperature conditions. Numerical model was implemented to evaluate effective prepreg permeability by matching the model and experimental flow-front progression.

These prepregs configurations are separated into fabric geometry (tow dimensions and tow spacing) and initial resin distribution. This research is currently focused on characterizing Gurit® Single Sprint© ST94 Out-of-Autoclave prepreg for Marine applications. ST94 is a woven fabric with a layer of precast, pre-catalyzed epoxy resin applied to one side of the fabric. The resin film layer only penetrates the fabric layer minimally so the resin film and the fabric layer can be thought of as separate regions of the prepreg. This is advantageous for processing characterization because the initial resin/fabric configuration is well defined. ST94 is sold with a variety of resin film thicknesses and fabric geometries. This research utilized ST94-RC200T and ST94-RC303T. Both prepregs are twill weave carbon fabric with a 42 weight percent resin film. The ST94-RC200T has a fabric aerial weight of 200g/m^2 with 3000 fibers per tow and a tow width of approximately 2mm, where the ST94-RC303T has a fabric aerial weight of 303g/m^2 with 12000 fibers per tow and a tow width of approximately 6mm. The ST94-RC202T has a rounder tow cross-section while the ST94-RC303T has a flatter tow cross-section. The images of the 2 fabrics are shown in Fig. 21 below.

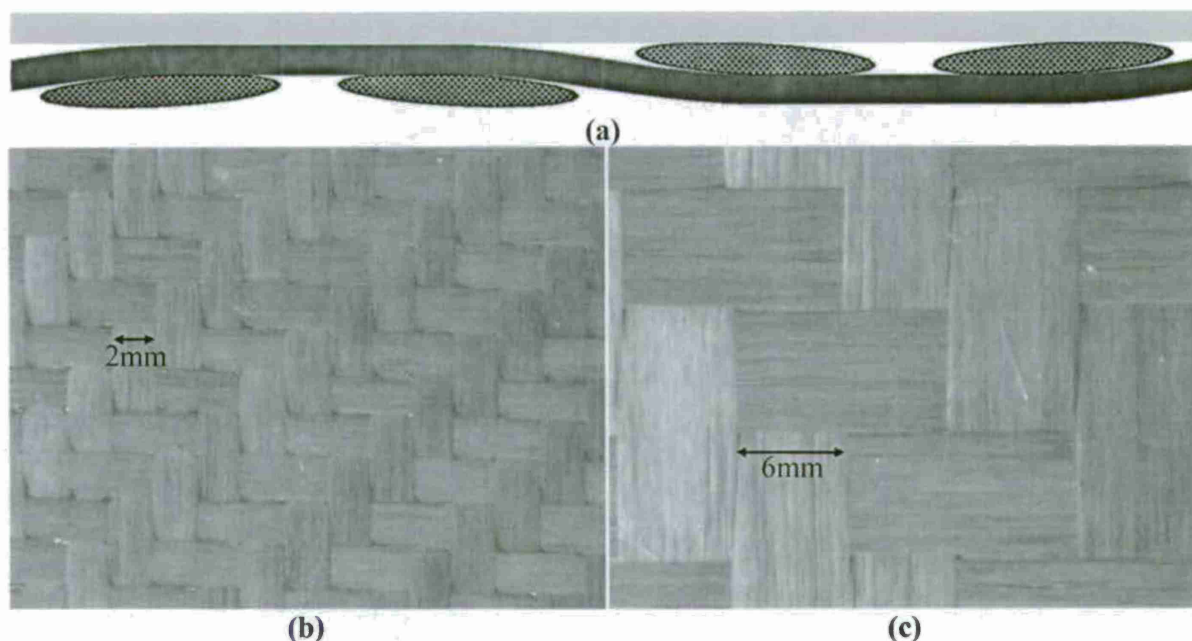


Figure 21: Both (a) and (b) are images of the fabric dry side of the prepreg showing an area approximately 25mm wide by 20mm (b) ST94-RC200T: fabric aerial weight of 200g/m^2 , 3000 fibers per tow, and tow width of approximately 2mm. (c) ST94-RC303T: fabric aerial weight 303g/m^2 , 12000 fibers per tow, and tow width of approximately 6mm.

Experimental Technique

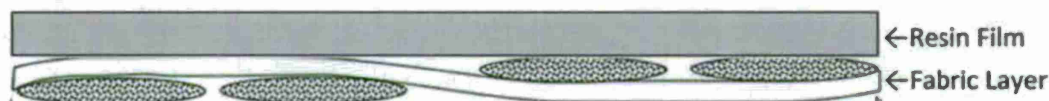


Figure 22. Schematic of ST 94 cross-section.

A single layer of partially impregnated ST94 prepreg (Figure 22) is cut and placed between 2 clear plastic release films and placed on an acrylic table with the dry side of the prepreg facing down on the table. A heated weight of known pressure and temperature is added on top of the prepreg sample to simulate the roller pressure. Weight is added on top of the block to vary the pressure (Figure 23). The resin starts saturating the prepreg, emerging at the originally dry bottom surface. The flow patterns are recorded and transferred to MATLAB as a matrix of pixel brightness values (0-255).

All images are subtracted from the image of the initial dry fabric at time equal zero to obtain the change in pixel brightness for each pixel in the matrix over time. By setting a threshold, pixel values that become darker below the threshold value are considered to be filled. Adding up the total number of filled pixels and dividing by the total number of pixels gives the fraction of area filled at the bottom for each image as a function of time.

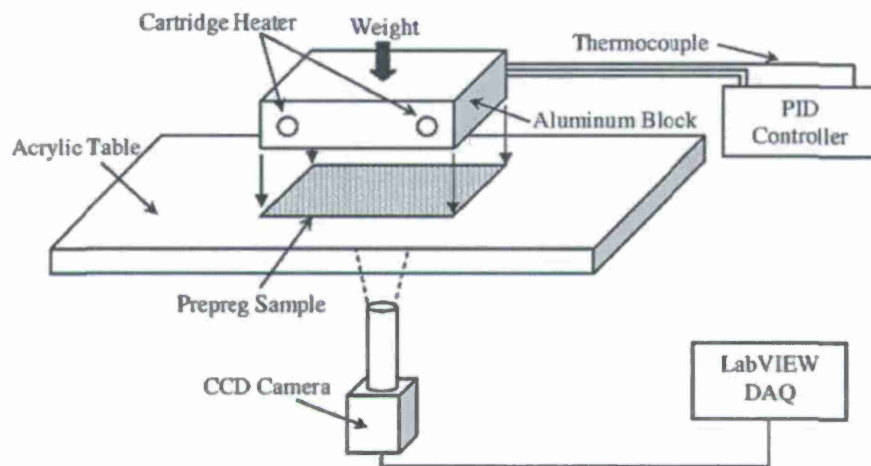


Figure 23. Experimental Setup for resin impregnation visualization.

The flow front development can be characterized in terms of the fraction bottom surface area covered with resin as shown in Figure 24. The resulting filled area could be correlated with the semi-consolidated prepreg properties, such as air permeability (needed for volatile evacuation during the final consolidation).

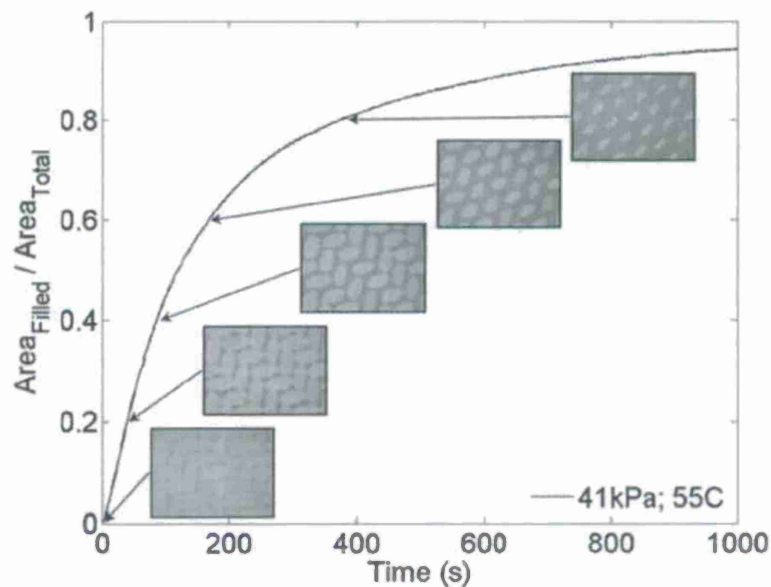


Figure 24. Images of ST 94 prepreg corresponding to the graph of the quantified area of resin observed over time at 55C and 41kPa of applied pressure.

The flow behavior will depend on applied temperature and load, as shown below in Figure 25a.

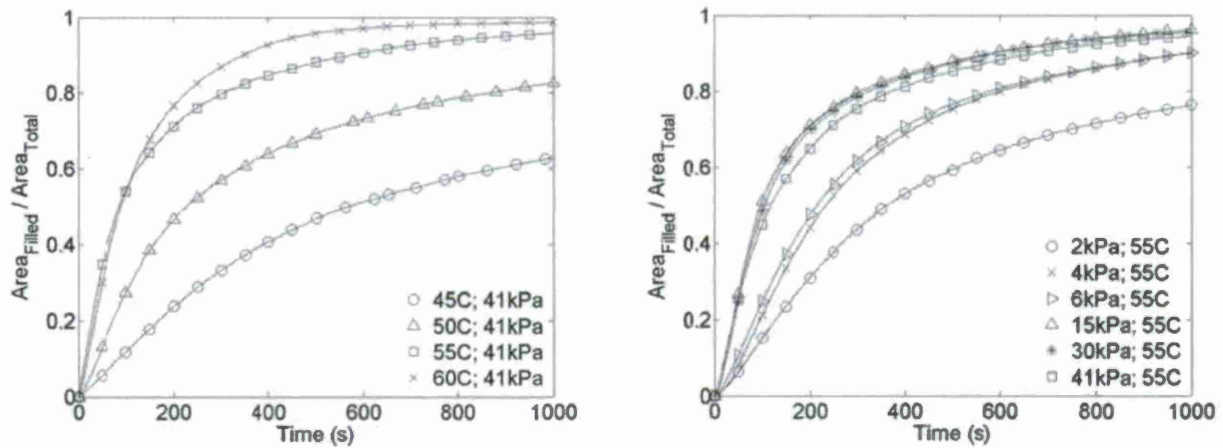


Figure 25. (a) Effect of temperature and applied consolidation load on the area filled area over time in ST 94 prepreg.

The attempts to fold these curves on a master line using non-dimensionalization and temperature dependent viscosity were successful for varying temperature but could not describe the effect of load variation. To do this, the changes in fiber-tow structure caused by the applied load must be considered. (Figure 25b).

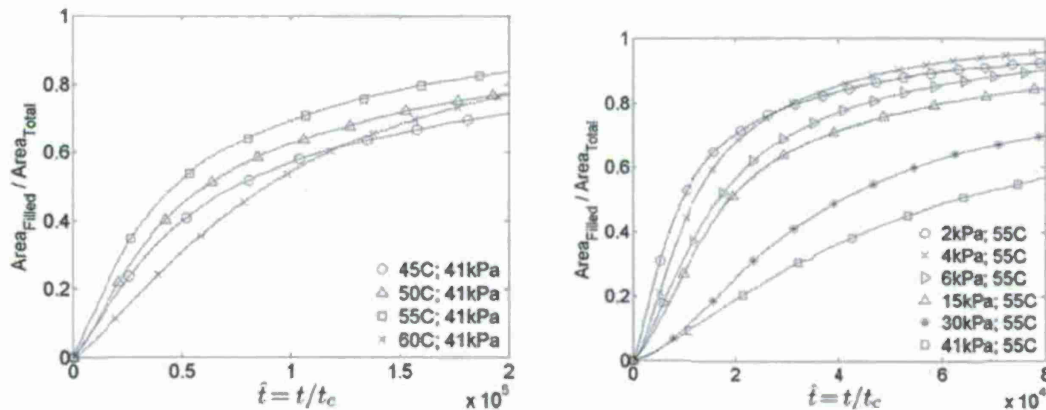


Figure 25 (b) Effect of temperature and applied consolidation load on the area filled area over time in ST94 prepreg when time is non-dimensionalized by $t_c = \text{viscosity (PA*s)}/\text{Pressure(Pa)}$

Analytical Model

The analytical model describes the flow as a linear flow through a series of two blocks of porous media (or channels). First one of these will have the permeability K_1 typical for pinholes and the channels between fiber tows, the later one will represent the flow entering the fiber tows with permeability K_2 . By matching the filled area – time curve these values may be evaluated for individual load/temperature cases as shown below (Figure 26).

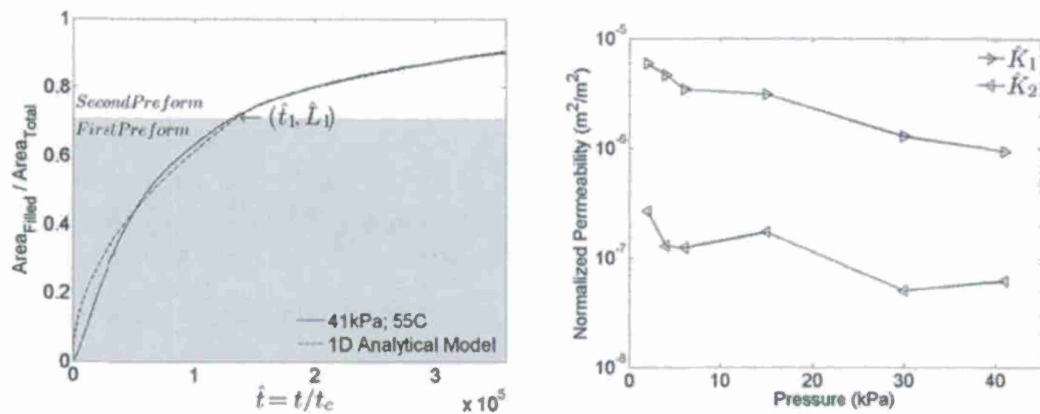


Figure 26. (a) Fitting the experimental filled area to estimate the prepreg permeability values (left) and the dependence of prepreg permeability on applied load.

The model results underline the effect of the applied load on prepreg structure. Once the load dependent permeability is included in non-dimensionalization, the prepreg saturation behavior can be determined from the master curve by scaling (Figure 27).

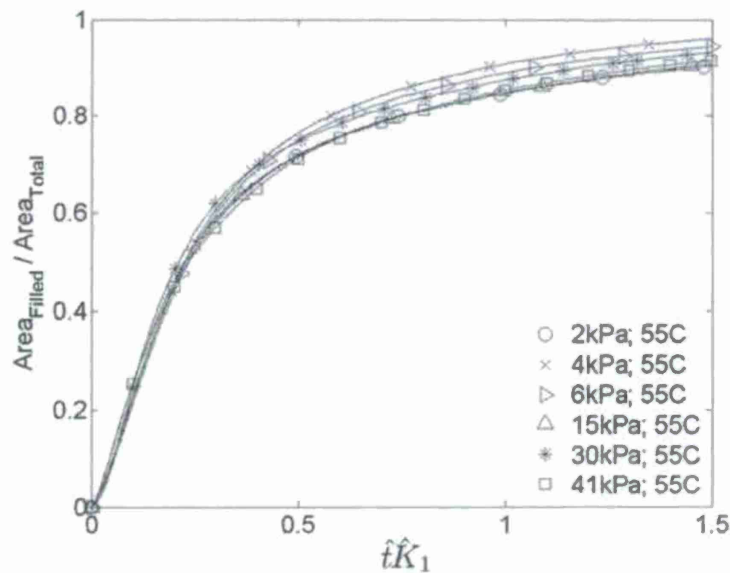


Figure 27. By scaling the results from Figure 25 by non-dimensional \hat{K}_1 from the 1D model, the curves at different applied loads coincide. Thus, one set of experimental data can be used to predict behavior at different compacting load.

Summary

A method was developed to characterize a partially impregnated prepreg by quantifying the area filled over time as the resin is heated and pressed into the fabric. The effect of temperature on the rate of fill is shown to scale with viscosity while pressure applied is shown to have a nonlinear effect on the fill characteristics. A 1D analytical model of an RTM process consisting of a

constant injection pressure into two preforms in series is used to fit the data to show how applied pressure to the prepreg affects the permeability of the fabric. By scaling the non-dimensionalized experimental results by the normalized preform permeability one can predict the filled state of the fiber network during a resin film infusion.

The results allow one to predict the progressing prepreg resin saturation based on applied load and temperature. Successful non-dimensionalization means that the model can be applied for pressure/temperature combinations that were not tested.

Several issues were realized during this work. Applying higher consolidation loads in limited time is not effective, as the prepreg permeability decreases as the driving pressure increases. The full saturation cannot be achieved during on-line consolidation and it may be desirable to restrict this so that the volatiles can be evacuated during the final consolidation. One of the current goals is to develop a setup and measure and predict (with a model) the time needed to bring a preform to full vacuum.

Model for Evacuation of Voids

As a part of permeability measurement of prepregs, experiments were conducted with the evacuation of the prepreg panel by applying vacuum along one edge in task (i). The experimental results suggest this is rather a lengthy process. Hence an evacuation model has been developed to simulate this scenario. Based on the ideal gas law for the volatiles, the governing equation for the pressure distribution was found to be

$$\dot{p} = \frac{K}{\eta \cdot \phi} \cdot p \cdot p''$$

where K represents the prepreg permeability, η the air viscosity and ϕ the prepreg porosity. With judicious non-dimensionalization,

$$\begin{aligned}\tilde{x} &= \frac{x}{L} \\ \tilde{p} &= \frac{p}{p_{atm}} \\ \tilde{t} &= \frac{t}{\frac{L^2 \cdot \phi \cdot \eta}{K \cdot p_{atm}}}\end{aligned}$$

(L being the panel length) the equation folds into a parameter independent equation

$$\frac{\partial \tilde{p}}{\partial \tilde{t}} = \tilde{p} \cdot \frac{\partial^2 \tilde{p}}{\partial \tilde{x}^2}$$

which can be solved to provide dependence between non-dimensional pressure and non-dimensional time. For example, at the location furthest from the vent line, the development of pressure with time can be plotted as shown in Figure 28.

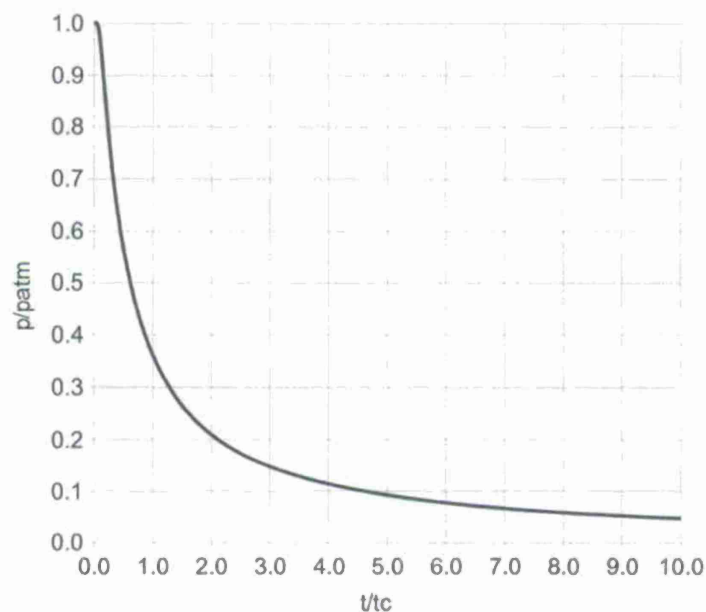


Figure 28. Development of non-dimensional volatile pressure with non-dimensional time. Actual time scale may be obtained by multiplying the non-dimensional time by the characteristic time value provided above.

The model can be used to evaluate the prepreg permeability easily. The value of prepreg permeability obtained by this method is around $1 \times 10^{-14} \text{ m}^2$, low but much higher than the value obtained by other experimental methods. As the characteristic time scales with L^2 and for 3" long panel the value is in the order of 1,000 s, the time needed to evacuate large structure must be carefully evaluated and taken into account when process is designed, as substantial increase in the distance between vent and any part location may easily result in extreme time requirements.

The further development of the model should include release of moisture or volatiles from prepreg with pressure reduction. Due to the omission of this physics, the current estimates can be seen as lower bound for time estimates. This part of the task supplements the experimental component of task I.

Previous evacuation analysis revealed a significant time requirements to evacuate large parts by using one-dimensional in-plane air flow. This is the effect of limited in-plane permeability and large part size. The obvious remedy to this issue might be evacuating the volatiles through the thickness direction through the distribution media to the part edges, or close to them, as the distribution media may not extend to the part edge. Governing equations were developed for fairly general model. The modeled cases include linear and radial volatile evacuation under prepreg partially covered by distribution media as shown in the Figure 29. Note that the radial evacuation is, due to the lack of edge effects which is much more suitable for experimental characterization than linear case.

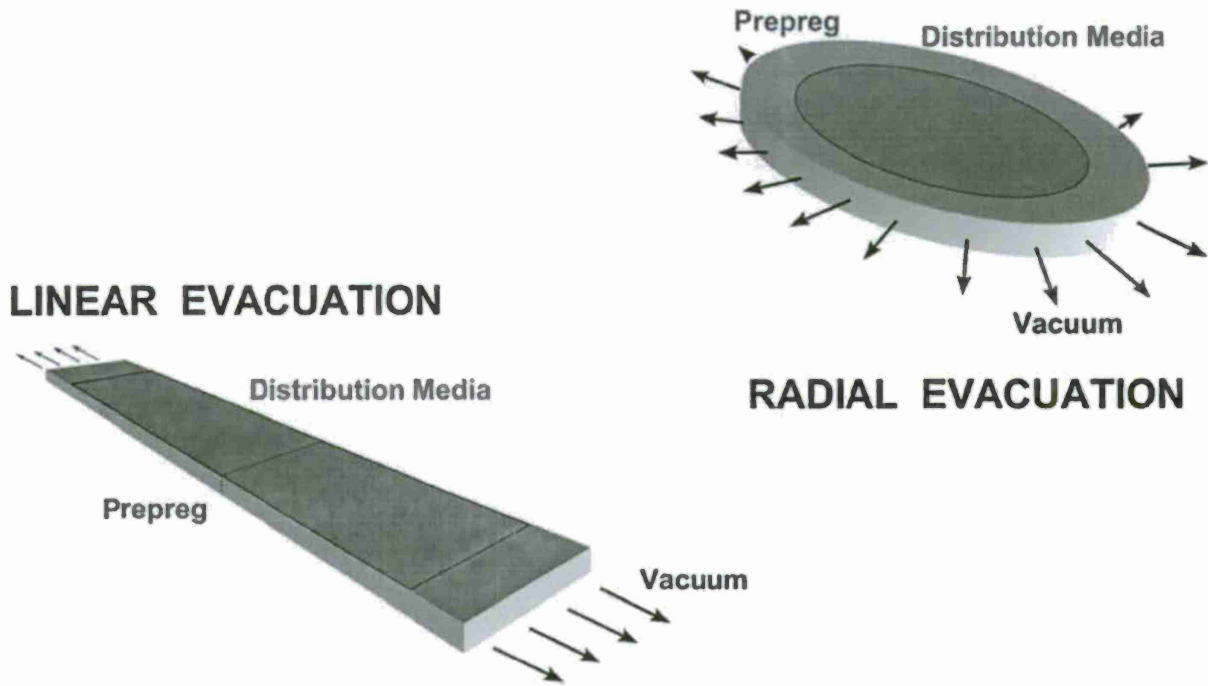


Figure 29. Simple cases of volatile evacuation combining in-plane and through-the-thickness volatile flow.

During the model development, we also relaxed the constraint on prepreg deformation during the vacuuming, though this option has not been exercised and needs some additional material characterization. Thus, the model includes:

1. Compressible volatile expansion and evacuation.
2. Flow both in-plane and through the thickness
3. Transient change in material porosity, permeability and thickness, characterized by the strain ε .
4. Similar change in distribution media (ε_{DM}).

The governing equation for the volatiles flow in the prepreg is

$$\dot{p} + \dot{\varepsilon} \frac{p}{\phi(1 + \varepsilon)} = p \frac{1}{\eta \phi(1 + \varepsilon)} (\nabla \cdot \mathbf{K} \cdot \nabla p)$$

For non-deformable preform and one-dimensional flow this reduces to the previous relation. However, even for a non-deformable preform this equation by itself produces two or more characteristic numbers because of the multiple permeability components.

As the flow within the distribution media can be assumed in-plane only, the distribution media presence can be accommodated in complex boundary condition:

$$\dot{p} \phi_{DM}(1 + \varepsilon_{DM}) h_{DM} + \dot{\varepsilon}_{DM} p h_{DM} = p \frac{h_{DM}}{\eta \phi_{DM}} (\nabla^p \cdot \mathbf{K}_{DM} \cdot \nabla^p p) - p \frac{1}{\eta \phi_{DM}} K_{zz} \frac{\partial p}{\partial z}$$

In this case, the gradient and divergence operators are in-plane only. And z is the through-the thickness direction. Note that to solve this system in general settings one also needs to provide proper constitutive relations for transient prepreg and distribution media deformation:

$$\dot{\varepsilon} = \dot{\varepsilon}(\varepsilon, p, t)$$

$$\dot{\varepsilon}_{DM} = \dot{\varepsilon}_{DM}(\varepsilon_{DM}, p, t)$$

These relations are currently under investigation.

Geometric cases presented in the Figure 29 lead to two-dimensional governing equation and one-dimensional boundary condition. The solutions presented was obtained for no transient deformation. Nonetheless the number of similarity parameters goes from 1 to 5. Simple master curve solution is therefore not feasible and the problem has to be solved for particular set of parameters numerically.

The numerical solution is, however, straightforward and has been tested for the cases without material deformation. Figure 30 shows the volatile pressure in cross section of radially evacuated part after 100 s. The radius is 0.61 m (2') and thickness is 0.0127 m (0.5"). Distribution media used is a circular section of 0.305 m radius. It is quite clear that the radial vacuuming and presence of distribution media speed up the evacuation dramatically.

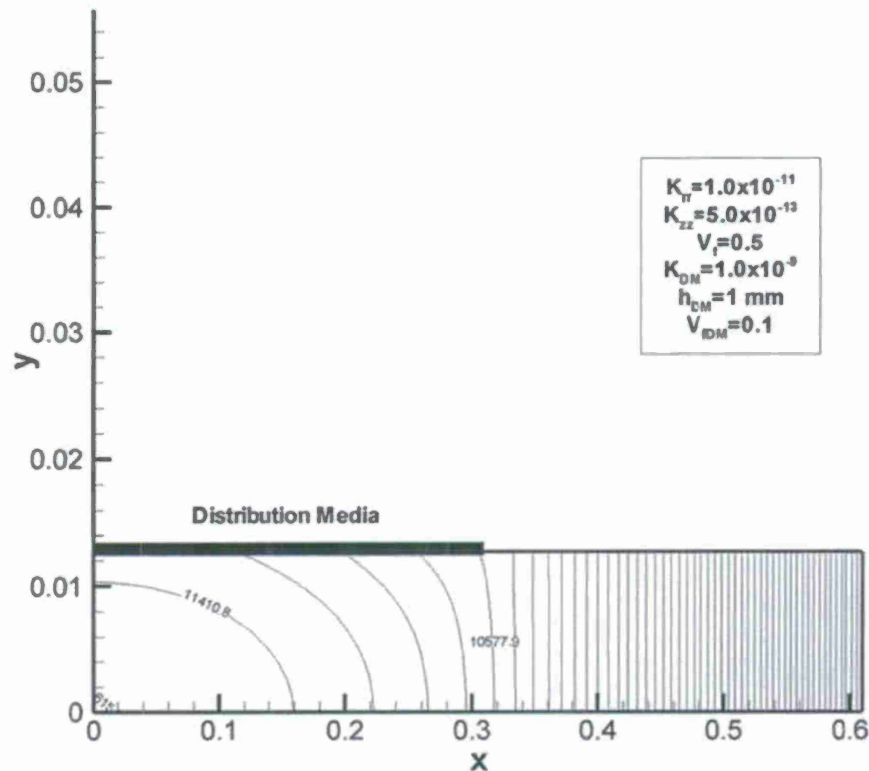


Figure 30. Two-dimensional pressure profile at 100s within a radial part being evacuated.

Note however typical prepreg permeability values are often far lower than those in the example and the time scales linearly with permeability as long as the ratios remain the same. Also, the part is relatively small.

The development of the pressure at the region across the inlet is shown in Figure 31. The path forward is to develop and model schemes that will allow us to evacuate air from large parts relatively quickly by placing the distribution media strategically.

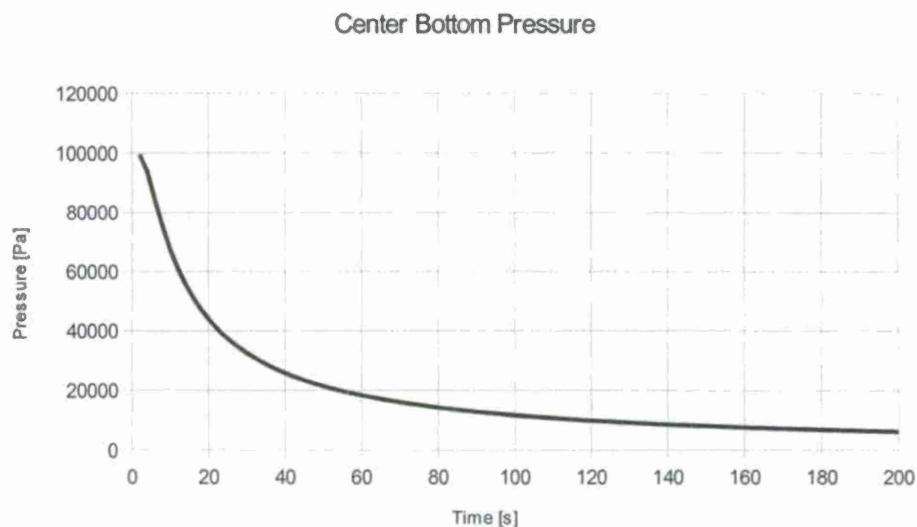


Figure 31. Change in air pressure in the region opposite the distribution media during evacuation with time for the geometry shown in Fig. 30.

Task IV Modeling And Design of Prepreg Tape Placement Process

Introduction and Background

Suppliers of composites processing equipment are offering a greater variety of machines and have made significant advances to automated tape laying (ATL) and automated fiber placement (AFP) technologies. Companies are moving beyond standard thermoplastic and thermoset prepregs and are looking at placing OOA prepregs as well as dry fabrics. Today, Automated Tape Laying (ATL) and Automated Fiber Placement (AFP) machines are in use in the manufacture of almost every modern commercial (Boeing's 7XX and Airbus' A3XX) and military (C17, A400M, V22, F/A-18E/F, F35, Typhoon) aircrafts [1-7]. Typical parts made with these processes are the fuselage, wing skin panels, wing box, tail and other structures. These technologies have made it possible to incorporate composites in commercial aircrafts in excess of 50% of a plane's structural weight as shown in Figure 32. These technologies are also being evaluated in other areas such as boat hulls, wind blades production and medical components. Because of their background in aircraft production, most of today's available ATL/AFP machines are very large and complex with costs in excess of several million dollars [8]. As a result, most companies cannot afford this equipment and have to "rely on lower-tech processing methods like hand layup" [9]. But there is a "demand for automated technology that enables series production" especially for "small- to medium-sized, relatively simple composite structures" [10]

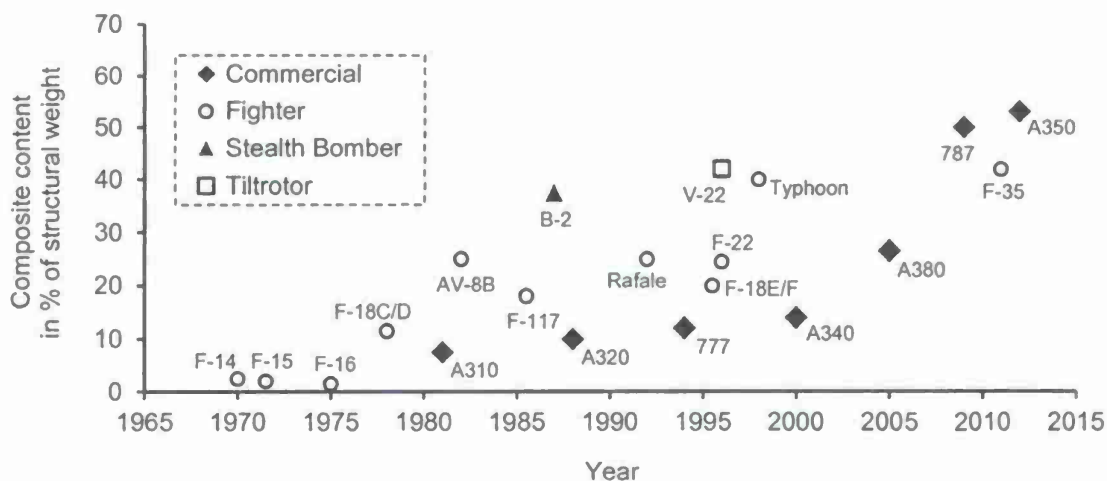


Figure 32: History of composite use in aircrafts [2-7]

Different approaches were made recently to fulfill this demand for more affordable and smaller ATL/AFP equipment. Companies like Automated Dynamics (Schenectady, NY, USA) or Accudyne Systems (Newark, DE, USA) design purpose-built machines "to meet a customer's specific need" [11]. Other vendors, shown in Figure 33, use standard off-the-shelf articulated robots which with custom swappable heads that can reduce the cost of an ATL/AFP system [12,13]. Either way, future ATL/AFP systems "will be key to high-volume production of composite items, promising reliable, consistent and cost-effective fabrication" [12]. Even with

the current systems that exist for automated manufacturing, there are limitations to the use of this commercial equipment in a research environment. These limitations include the fact that:

- The hardware is 'hard coded' and designed specifically for processing certain materials and forms thus limiting flexibility in design.
- The systems are unavailable to academic institutions due to proprietary hardware and process data.
- The equipment is continuously in use and is unavailable for 'downtime research'
- The capital cost is prohibitive to academic institutions.

Because of these limitations the decision was made to design and build a custom machine that would serve as a legacy research tool for evaluation, design and optimization of ATL, ATP, AFP processes as well as other novel processing methods for composites structures.

In addition, new materials such as out-of-autoclave (OOA) prepreg composite tapes have been developed during the last decade and are now being considered for use in automated manufacturing. These materials are usually vacuum-bagged and cured in an oven without the need of an expensive autoclave. At the same time, they deliver "less than 1 percent void content and autoclave-quality mechanical properties required for aerospace" [14]. Incorporating these materials in ATL type processes could lead to significant cost and cycle time reductions for large structures. Direct use of these materials in existing equipment is difficult, however, due to the lack of research to defining optimal process conditions and limitations to modifying existing hardware. In summary having a custom built work cell will allow exploration of these new materials combined with novel processing methods.

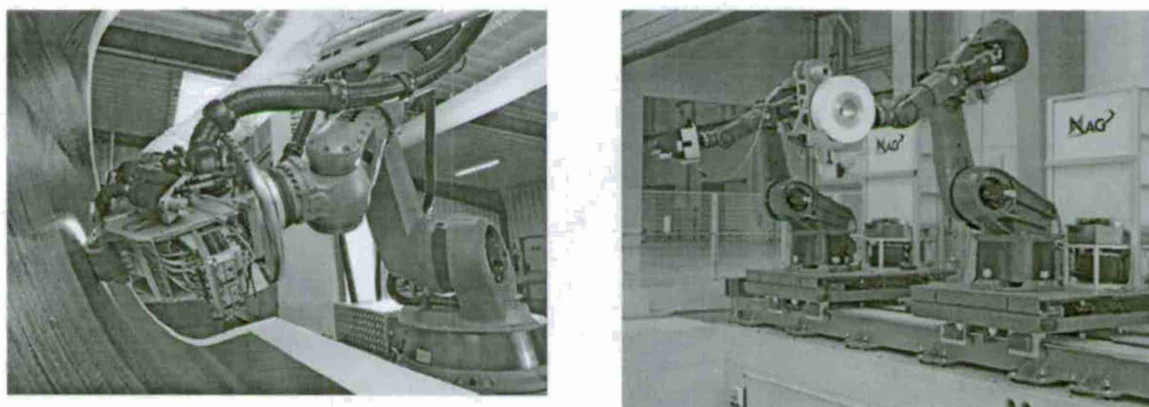


Figure 33: Automated systems for processing PMC prepreg tapes: AFP system (Coriolis Composites, France) [12] ; AFP/ATL system (DLR, Germany and MAG, USA) [13]

The Automated Materials Placement (AMP) System

The Automated Materials Placement (AMP) system designed and built at the University of Delaware's (UD-CCM) Composite Manufacturing Science Laboratory is a custom designed IRAD funded system for conducting innovative research in automated composites manufacturing. The AMP system, shown in Figure 34, is designed to be flexible for research, modular for multiple projects and adaptable as new materials and processing techniques emerge. The system was designed with Dassault Systèmes CATIA software utilizing the assembly design, wireframe and surface design, part design, and cable harnessing module. The system is designed to process thermoplastic and thermoset prepreps, dry fabrics, neat films, metal matrix

and hybrid composite materials. The AMP is also designed to facilitate modules for stitching, power coating, film coating and a post-process sprayable bagging system. The system is built on a 6-axis articulated ABB IRB 6640-180/2.55 robotic system run by an IRC5 controller. An extra axis (IRBP D 2009 positioner, not shown) is also available for filament winding.

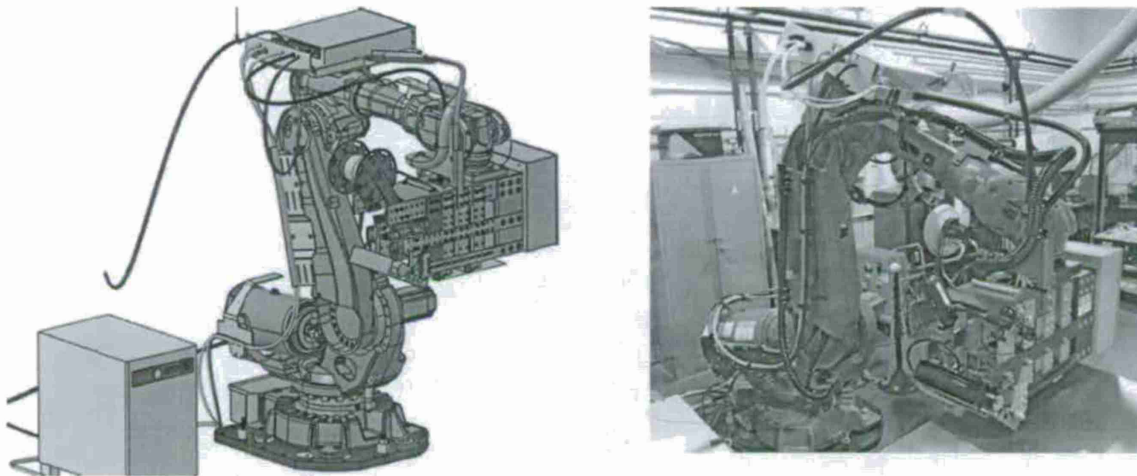


Figure 34: The custom designed AMP system developed at UD-CCM

The system is built with a 'plug and play' framework with swappable modules for process design and optimization. A number of these modules with specific functionality are shown in Figure 35. These modules use a common strut design, which slides directly into the AMP frame. The modules have infinite adjustment in the material travel direction and can be swapped, rearranged or upgraded without large capital expense or downtime. Components for heating modules include infrared, hot gas, laser and flame modules. Modules to apply pressure include rigid rollers, flat shoe and soft rollers. Additional modules currently being developed include an automated feed system, spray bagging system, UV cure module, fabric stitching, film coating and in-line NDE system. Some of these modules have already been built and installed while others are still in the development and fabrication phase. Each module is designed to have a minimal profile so that they can be stacked in close proximity. The modules are also equipped with a single air, power and electronics connector to allow for quick installation and removal. A comprehensive reach and cable harness design was carried out with CATIA to maximize robot turn and extension. The workstation was designed to allow access to a flat tool surface and extra axis (not shown). Some figures showing these simulations are given in Figure 36 A 200° rotation is necessary at the head location to allow placement of 0° to 180° ply orientations on the tool surface. The following sections describe some details about the various modules currently built into the AMP system.

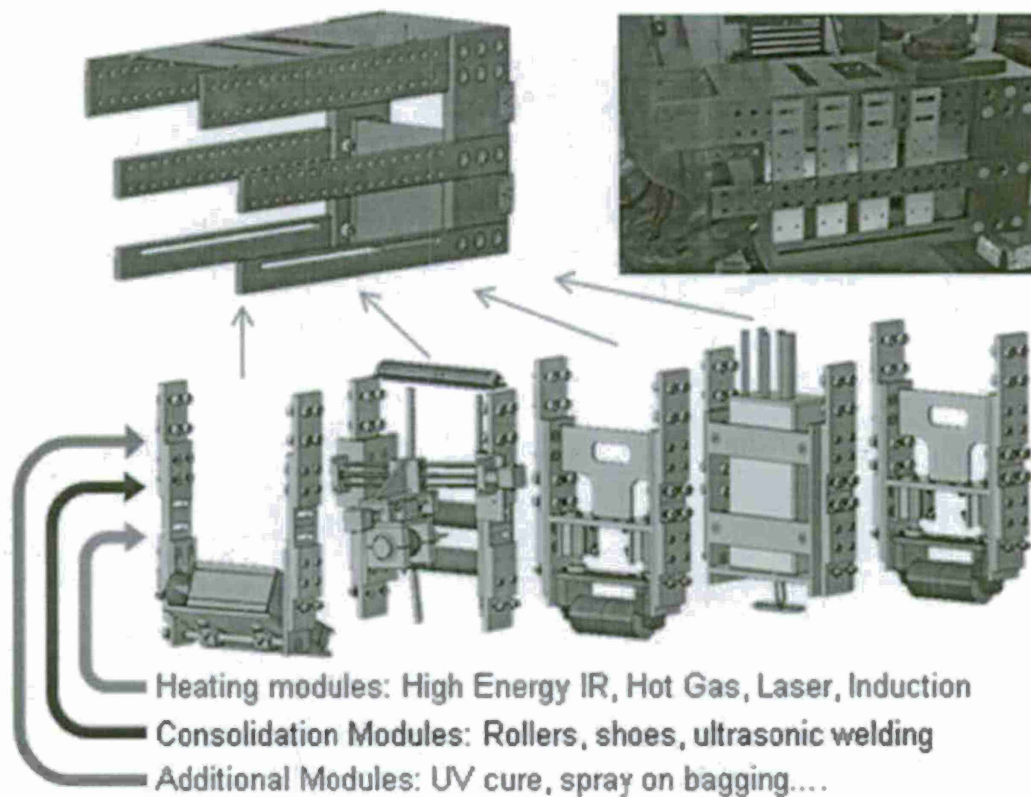


Figure 35: Various process modules that slide into the AMP chassis.

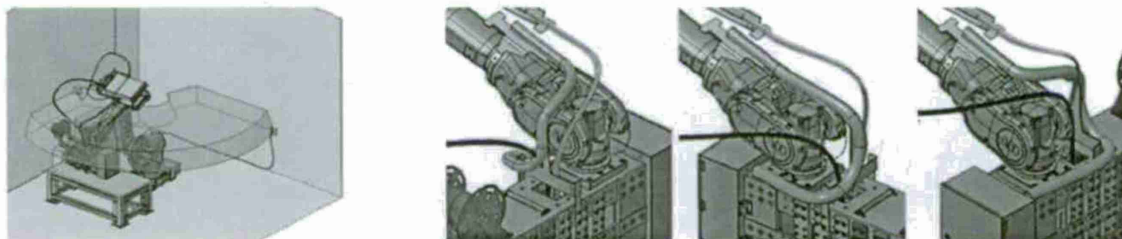


Figure 36: Robotic reach and cable harness design and optimization

Consolidation Modules

The consolidation modules shown in 37 are comprised of two pneumatic actuators with in-line load cells that apply force to a subassembly mounted on two linear guides. The sliding subassembly, shown as the darkened components in Figure 37, can be swapped out and replaced with a sliding shoe or compliant roller assembly. The current rollers are comprised of 165mm wide stainless steel material but can be swapped out for narrow rollers to provide higher pressure or ceramic rollers for induction consolidation. Two 250lb Futek load washers measure force during processing. The entire module is 75mm in depth so that heater and cooling modules can be placed in close proximity to this module during processing. To date, two consolidation modules have been built to allow for nip point-post induction consolidation and a swap out for different assemblies.

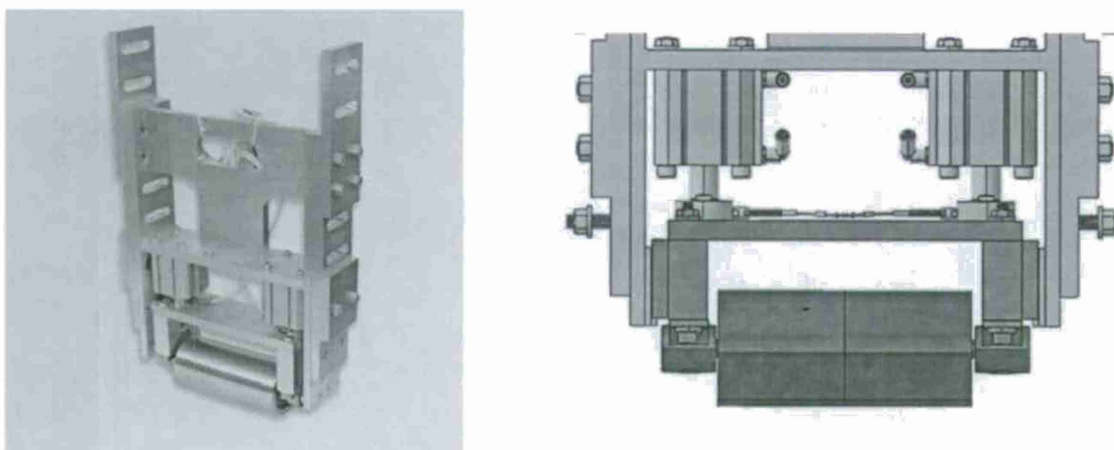


Figure 37: AMP Consolidation Module

Infrared Heating Module

A 350W IR radiant heater (2KH-L0285 by Kubota Research Associates Inc., Hockessin, DE, USA) is used in the AMP-system as a surface heat source during processing of most PMC tapes and as preheating for MMC tapes and certain carbon fiber reinforced PMC materials. The module, shown in 0 38, can process materials up to 250mm in width and can be equipped with an optical IR filter to provide radiation of a fixed wavelength. The unit is mounted on a rotating stage that also includes vertical motion and horizontal translation. This allows the module to function both as a nip point heater and for general use surface heating.



Figure 38: IR module and power supply (with Kubota Research Associates IR System)

Induction Heating Module

UD-CCM has done extensive work in the past on volumetric induction heating and consolidation of carbon fiber composites. This work resulted in the development of the Rapid Automated Induction Lamination (RAIL) process which was implemented for high-volume production of 8-ply AS4/PEI laminates. [15,16]. The process takes advantage of susceptorless induction heating to generate the volumetric heating necessary for rapid multi-layer consolidation for high throughputs. The benefits of this technology for volumetric heating is realized here by incorporating a Huettinger TIG 5/300 5kW induction welding system as a module within the

AMP system (Figure 39). The unit is mounted vertically for compactness with available vertical adjustment. The HF-generator is mounted on top of the robot's upper arm with two solid thick copper wires protected by a thick plastic shielding and supported by a tool retractor cable. Various coil designs will be utilized with the AMP to apply volumetric heating on preconsolidated laminates.

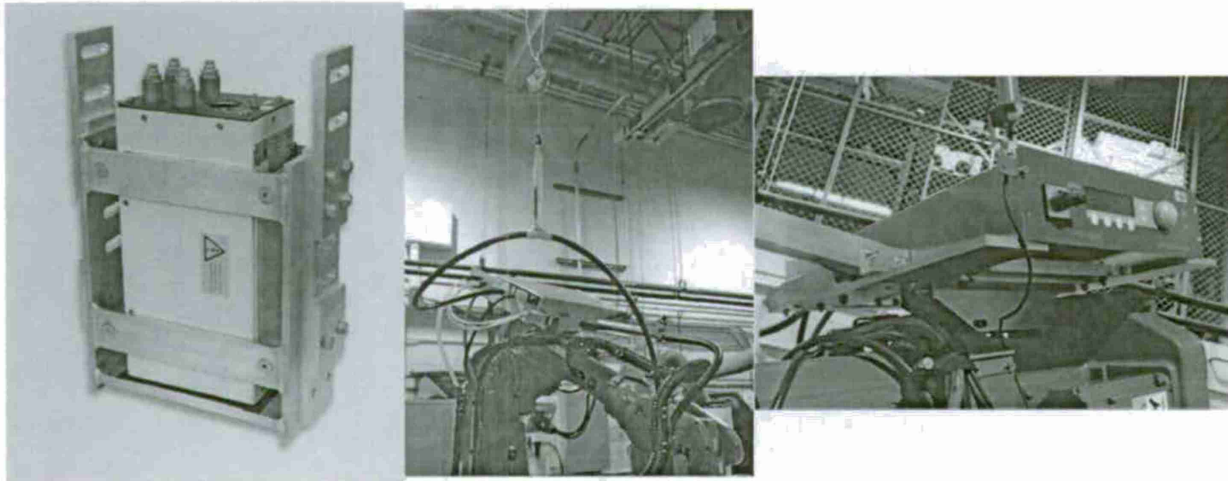


Figure 39: AMP Consolidation Module (with Huettinger TIG 5/300 5kW welding system)

Material Handling Module

The main purpose of material handling system is to supply material to the surface in a continuous and controlled manner with integration. The system must seamlessly integrate into the overall framework without compromising flexibility for new materials and processes. To achieve this, a series of electrically driven rollers are combined with an ultrasonic transducer to cut and feed material to the surface for processing. The system, shown in Figure 40, utilizes internal motors that reduce external components such as motors and gears, which require frequent maintenance. These rollers also incorporate directional control through an internal gearbox that can be used to optimize speed and torque. The 500W ultrasonic transducer is mounted on a linear guide that is positioned at an angle with respect to the material feed direction. This allows the material to be cut while in motion by matching the relative vertical velocity of the cutter with the process velocity. Traversing at speeds higher or lower than the material velocity, results in angular cuts that can help reduce material waste for off axis plies. Two sets of motorized rollers are used in tandem to allow feed of the cut material as well as ensure material tension during the cutting process.

The ultrasonic transducer is fitted with a double edged blade that can also cut the incoming material in both directions. The material is supplied from the top down by a supply spool with magnetic brake (shown in later figures). Adjustable guide rails are used to ensure material alignment to the part surface. The feeder is designed to handle material from 6.35mm (1/4") wide up to 203.2mm (8") and can cut thermoplastic and thermoset prepreg as well as dry fibers, neat polymer films and MMC tape. The ultrasonic transducer is mounted on a z-axis linear guide to allow the knife to retract while material is fed to the surface. The entire assembly fits above the

IR module so as to maximize the use of available volume. The material feed system is currently being built and will be incorporated into the AMP in the coming months.

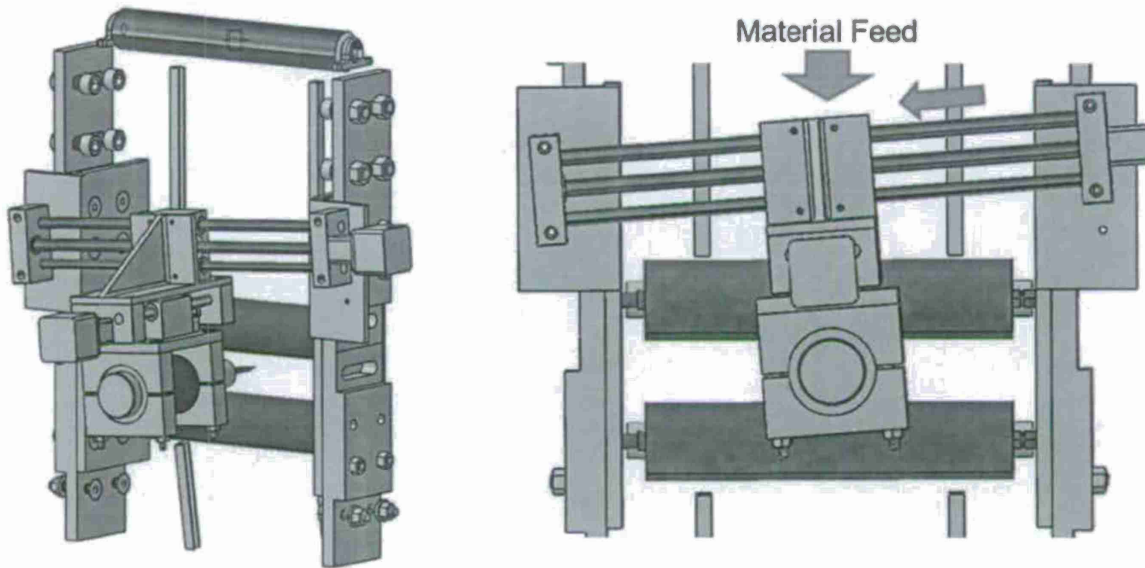


Figure 40: AMP Material Feed System

Wiring and Control Systems

All wiring within the head is fed through two central conduits that channel to the rear of the unit into a manifold and electronics enclosure. A schematic of this wiring scheme is shown in Figure 41. All feedback and control data is fed to and from a PC workstation through a National Instruments PXI chassis. This chassis houses two M-series multifunction DAQ boards connected to two SCB-68 I/O connector blocks, one of which is mounted in the AMP. The ABB IRC5 controller is also fed instructions from the control PC through a dedicated Ethernet connection. System motion is built using ABB's RobotStudio software shown in 0 41.

The entire system is controlled and monitored with a custom built National Instruments LabVIEW interface that communicates directly to the controller, FLIR A615 industrial IR camera, IR heater and induction control system. The GUI for this interface is shown in Figure 42 and utilizes a menu tree to define all elements on the AMP. The tree allows the end user to drag-drop elements to match the position of the physical modules as shown in Figure 43.. This flexible environment is designed to easily allow for incorporation of new modules and processes as they are developed and incorporated into the AMP system.

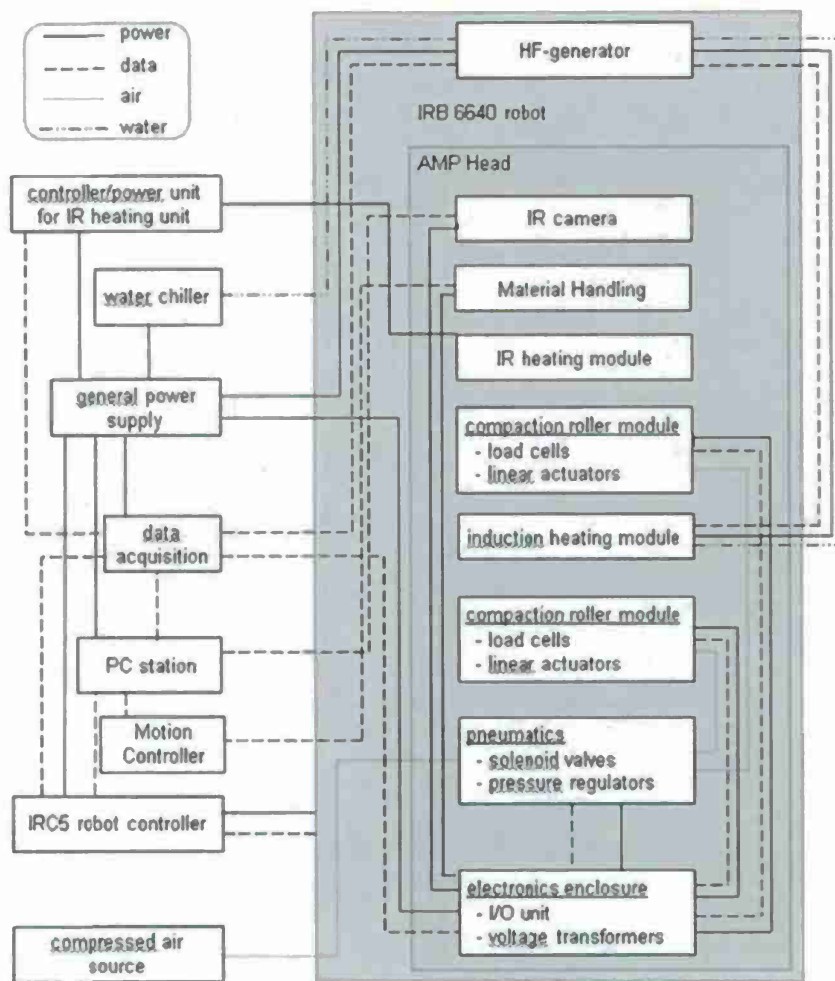


Figure 41: Schematic of data, air and water connections for the AMP-system

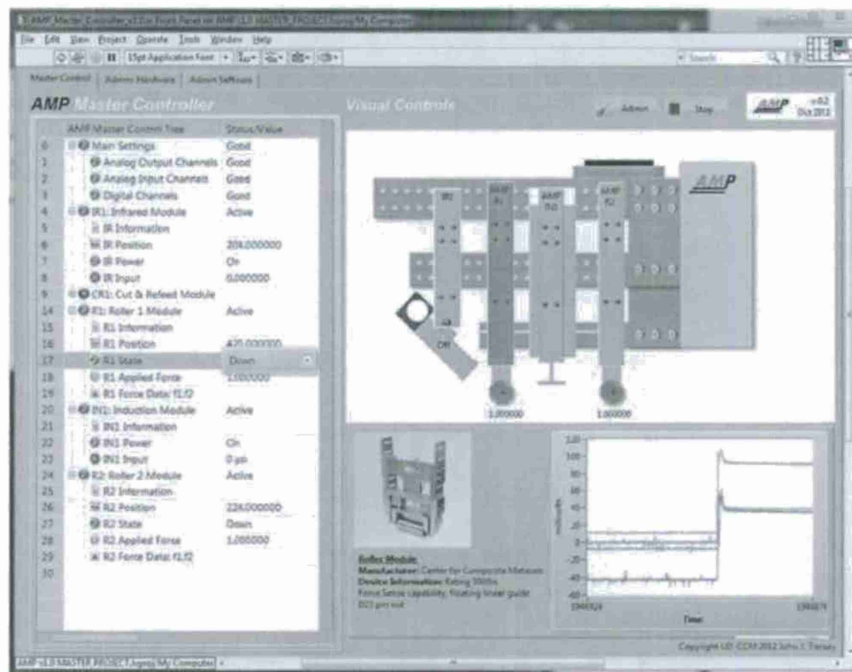


Figure 42: AMP master control software written in NI LabVIEW

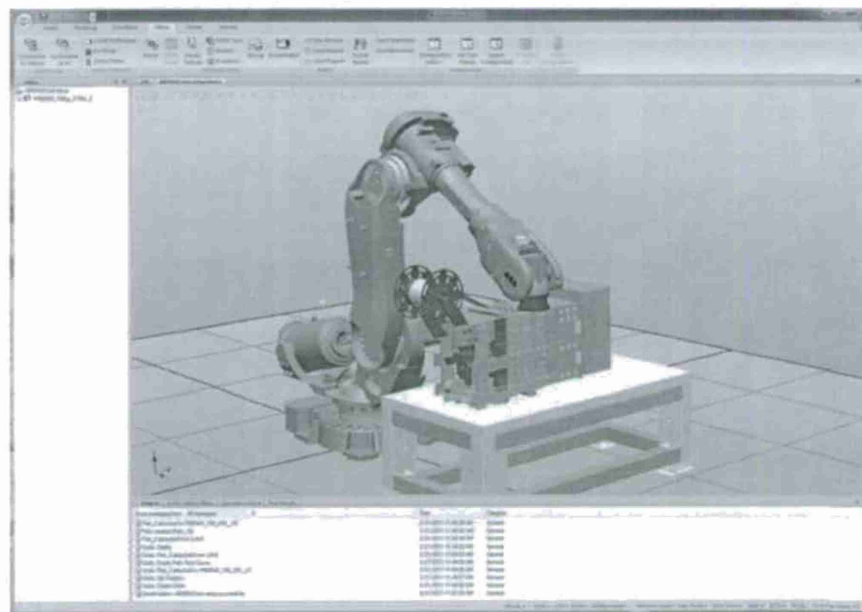


Figure 43: RobotStudio is used for virtual process simulation.

Thermal Measurements

An IR camera (FLIR A615 from FLIR Systems, Inc., Wilsonville, OR, USA), shown in Figure 44, is used to measure surface temperatures during processing. The IR camera is attached to the AMP using a five axis articulated holder (MA61003 from NOGA Engineering Ltd.). The holder

is attached to an end fastener that can be mounted at any location on the AMP system to observe heating from, infrared, induction or both sources. The LabVIEW toolkit from FLIR is used to extract data from the camera and is used in a PID control method within the master control environment.

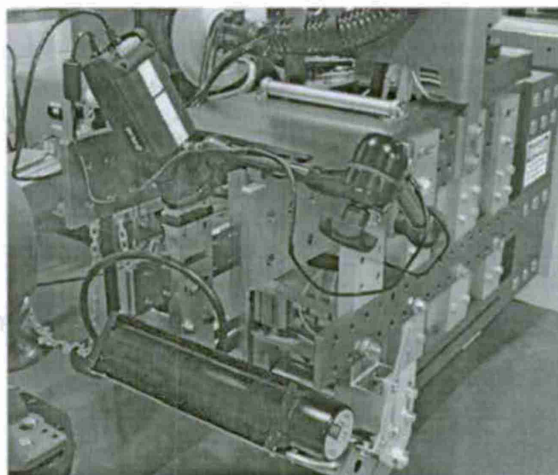
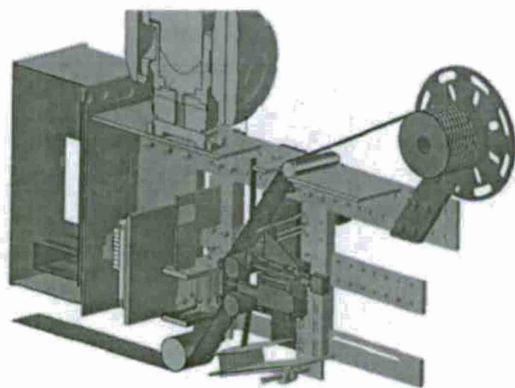


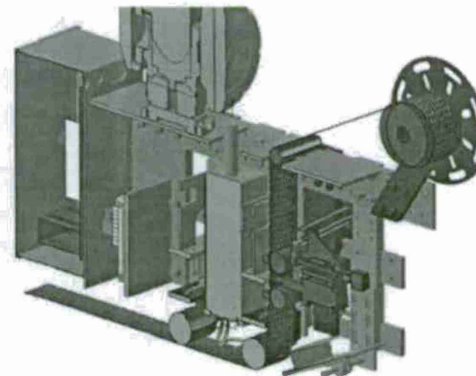
Figure 44: A615 FLIR Industrial IR camera mounted on a Noga flexible arm.

AMP Design Configurations

The flexibility built into the AMP system allows for a wide range of process configurations. Examples shown below in Figure 45a: IR assisted tack and consolidation and (b): IR tack followed by volumetric induction heating to progress ply by ply in-situ cure. The AMP system will be instrumental at examining novel ways to rapidly place and process these materials. Part of this effort also includes novel experiments to evaluate consolidation of partially impregnated prepreps by use of a transparent table shown in Figure 46.



(a) IR assisted thermoset tape placement



(b) IR placement followed by volumetric induction heating.

Figure 45: Various module configurations for the AMP System.

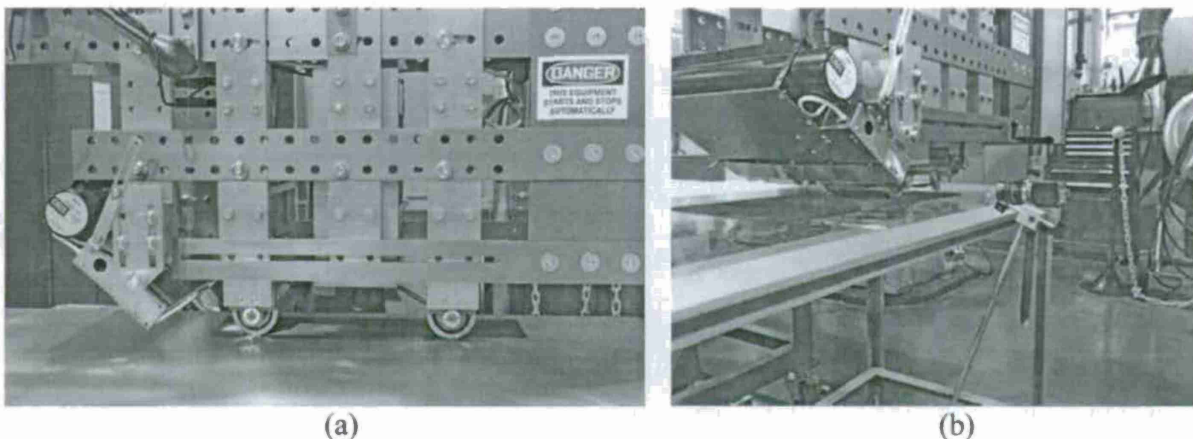


Figure 46: (a) IR heating and consolidation of carbon prepreg (b) consolidation of partially impregnated preregs on a transparent table

Conclusions and Path Forward

To aid in Out of Autoclave and Oven Cured manufacturing developments, a custom built Automated Materials Placement (AMP) system has been fabricated at the University of Delaware's Center for Composite Materials that can place thermoset and thermoplastic preregs and dry fabrics on flat or cylindrical surfaces. The AMP is designed to be modular so that various heating and consolidation methods can be studied and optimized with low risk on hardware investment. These flexible modules can be swapped or reordered to include high energy infrared heating, volumetric induction heating, roller or shoe consolidation, a sprayable bagging module, ultrasonic welding, powder impregnation system or in line fabric stitching module. The system is fully instrumented with thermal and modular force measurement capabilities as well as visual inspection and laser position sensors.

A number of projects have already begun utilizing this hardware that include OOA processing, novel consolidation experiments and sprayable bagging techniques. Having this equipment in-house will also allow model experiments to be conducted that aids in validating theoretical models developed for various materials and processes.

References

- [1] Michael N. Grimshaw, "Automated Tape Laying," in *ASM Handbook Vol. 21 Composites*.: ASM International, 2001.
- [2] Obaid Younossi, Michael Kennedy, and John C. Graser, *Military Airframe Costs: The Effects of Advanced Materials and Manufacturing Processes*. Santa Monica, CA: RAND Corporation, 2001.
- [3] Alan Baker, Stuart Dutton, and Donald et.al. Kelly, *Composite Materials for Aircraft Structures*, Joseph A. Schetz, Ed. Reston, VA, USA: American Institute of Aeronautics and Astronautics, Inc., 2004.
- [4] Ravi B. Deo, James H. Jr. Starnes, and Richard C. Holzwarth, "Low-Cost Composite Materials and Structures for Aircraft Applications," *NATO RTO AVT Specialists' Meeting on "Low Cost Composite Structures" held in Loen, Norway*, no. Published March 2003 in RTO-MP-069(II), ISBN 92-837-0026-0, 7-11 May 2001.

- [5] W. T. Freeman, "The use of composites in aircraft primary structure," *Composites Engineering*, vol. 3, pp. 767-775, 1993.
- [6] George Marsh, "Airbus A350 XWB update," *Reinforced Plastics*, pp. 20-24, November-December 2010.
- [7] N.N., "JSF contracts," *Reinforced Plastics*, p. 12, May-June 2011.
- [8] Jeff Sloan, "ATL and AFP: Signs of evolution in machine process control," *High-Performance Composites*, September 2008.
- [9] Carroll Grant, "Addressing the cost of aerospace composites," *High-Performance Composites*, March 2004.
- [10] Jeff Sloan, "ATL and AFP: Defining the megatrends in composite aerostructures," *High-Performance Composites*, pp. 68-71, July 2008.
- [11] Carroll Grant, "Status update on composites automation," *High-Performance Composites*, March 2011.
- [12] George Marsh, "Automating aerospace composites production with fibre placement," *Reinforced Plastics*, pp. 32-37, May-June 2011.
- [13] Christian Boge, "Robotic unit for the automated production of composite components," *JEC Composites Magazine*, pp. 33-35, January-February 2011.
- [14] Ginger Gardiner, "Out-of-autoclave prepregs: Hype or revolution?," *High-Performance Composites*, January 2011.
- [15] J. J. Tierney, S. Yarlagadda, D. Heider, N. Shevchenko, and B. K. Fink, "Rapid Automated Induction Lamination (R.A.I.L.) for High-Volume Production of Carbon/Thermoplastic Laminates," , Long Beach, 2001, pp. 393-402.
- [16] J. J. Tierney, S. Yarlagadda, N. Shevchenko, D. Heider, and J. W. Gillespie, "Rapid Automated Induction Lamination (RAIL) of Carbon/Thermoplastic Laminates: Process Optimization and Prove-out," , Europe, 2001, pp. 193-206.
- [17] Frédérique Mutel, "The significance of innovation in driving composites growth in Asia," *JEC Composites Magazine*, p. 3, October 2011.
- [18] D.H.-J.A. Lukaszewicz, C. Ward, and K. D. Potter, "The engineering aspects of automated prepreg layup: History, present and future," *Composites: Part B*, 2012, DOI: 10.1016/j.compositesb.2011.12.003.
- [19] Carroll Grant, "Automated processes for composite aircraft structure," *Industrial Robot: An International Journal*, vol. 33/2, pp. 117-121, 2006.

Task V Scaling Of Bagging And New Bagging Concepts For Vacuum Consolidated Oven Cure

Motivation and Background

Low-cost and scalable bagging concepts are being investigated to meet the next generation composite boat manufacturing process. The current state-of-the-art requires a manual bagging after the lay-up of the prepreg material into the mold. A variety of bagging materials exists with nylon film being the most commonly used in the composite industry. They are often selected depending on the processing conditions requirements of the lamina they are used with. The manual layup is not only extremely labor-intensive and but it also often results in leaks and bridges (back pressure created from bags not seating well) in bags during the bagging process leading to poor quality parts. Lately new alternatives such as reusable and single use spray-on bags have emerged. Those bagging materials are currently tested to determine their performance and the influence of their properties on the laminate quality. A better understanding of the relationship between the bag permeability and part quality has to be developed in particular as the composite structure becomes larger. This task is investigating a combination of sprayable bagging coating with integrated membrane to allow continuous venting of the total surface during processing. The entire system could then be applied using a robotic placement system.

Establishment of bagging requirements

Various films (Nylon, PTFE, ETFE,) demonstrated great performance in the vacuum bagging application; however none of them could really be used in an automated process. The consistency and reliability of composites parts made using those processes are often a factor of the experience and knowledge of the operators. Hence, the development of a consistent and reliable bagging alternative was needed. Based on the virtual simulation for cost reduction, a spray on bag system is seen as a good alternative for large structure boats. The main reason for which a spray on bagging is a valuable alternative is the fact that it could be automated. Combining the precision and the reliability of a multiple axis robot to a spray mechanism (as developed in task (iv), would allow us to reach a great level of consistency and efficiency.

A finite element analysis was conducted to relate bag permeability and part size to the leak rates and pressure drop under the bag as the permeability of vacuum bags can become an important parameter during composite manufacturing. The bag is used to provide a barrier between the laminate and the outside environment and any leak will result in an air flow within the preform potentially reducing consolidation and increasing the amount of internal voids lowering composite properties. Every bag has a finite permeability / diffusion coefficient and thus allows an air volume flow over time. Requirements on the permeability are different for various processes such as autoclave prepreg processing where positive pressure is applied or the vacuum assisted resin transfer molding process where the internal vacuum is used to compact the fabric and draw resin into the reinforcement.

In addition, increasing the surface area of the structure will increase the total air flow into the laminate requiring better barrier properties of the bag. This in turn will determine the number and

location of vents and the overall capacity of the vacuum pumps required for parts of different sizes. To be able to develop a new bagging method and/or bagging material that will meet the future requirements of the industry it is critical to understand both the fundamental understanding of the role of the bag and be able to create the characterization equipment to analyze its properties.

Establishment of bagging requirements

A standard composite prepreg layup is shown in Figure 47. The prepreg layers are placed on the tool and a breather cloth is placed between the laminate and the vacuum bag. The breather is used to allow extraction of any volatiles coming from the prepreg or through the bag. The pressure drop on the laminate surface is governed by the permeabilities of the bag ($K_{zz,bag}$) and the breather cloth ($K_{xx,breather}$), the thickness of the bag (d_{bag}) and breather ($d_{breather}$), and the size of the panel (x_0).

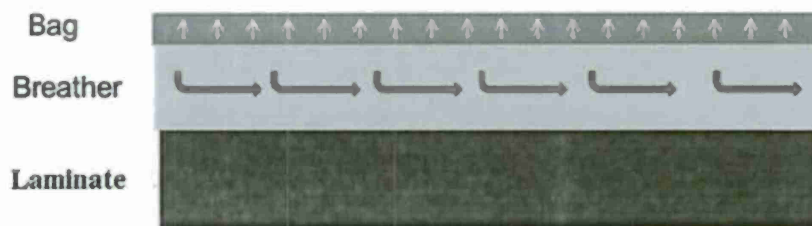


Figure 47: Schematic of a typical prepreg layup

The system above can be modeled using the Liquid Injection Molding Software (LIMS) developed at the University of Delaware Center for Composite Materials [5]. The system assumes flow in porous media and a non-compressible fluid. The model can provide insight into the pressure drop behavior of the breather material. Prepreg permeability is not considered in this parametric study. The flow rates in the breather cloth and thus pressure drop under partial vacuum will be smaller than predicted due to the air compressibility. Thus, the calculated requirements of the bag permeability will be more stringent than necessary. Multiple simulations were run with typical material properties for the breather cloth ($K_{xx, breather} = 1.0 \times 10^{-6} m^2$, $d_{breather} = 5.0 \times 10^{-3} m$) and for panel lengths of 1m and 5m. The permeability and thickness of the bag is varied and the pressure drop under the bag is calculated. Figure 48 shows examples of the pressure drop for a low (pressure drop of less than 100Pa) and high permeability (pressure drop of almost 1bar) bag. The good barrier properties of the low permeability bag reduces the air flow resulting in a very small pressure drop in the breather cloth while a high permeability bag shows almost 100% of the pressure drop in the breather cloth.

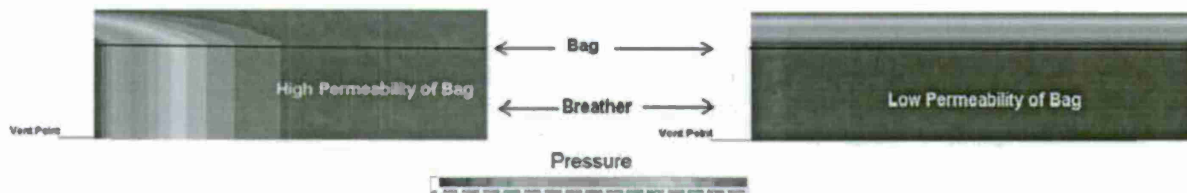


Figure 48: LIMS prediction of pressure drop under the vacuum bag

Figure 49 summarizes the LIMS results for varying bag permeability thickness ratios. It can be seen that in the case of low permeability bags the pressure drop under the bag is small. A 1% pressure drop ($\sim 100\text{Pa}$) may be considered acceptable and would require a permeability thickness ratio of no more than 10^{-17}m for a 5m long component and 10^{-16}m for 1m long component. High permeability bags above a permeability thickness ratio of 10^{-17}m will leak significantly and will not result in a total pressure drop under the bag. Increasing the panel size requires improved barrier properties of the bag by either increasing the bag thickness or selection of a lower permeability bag. Consequently, a high sensitivity permeability cell is required to characterize the effectiveness of bagging materials.

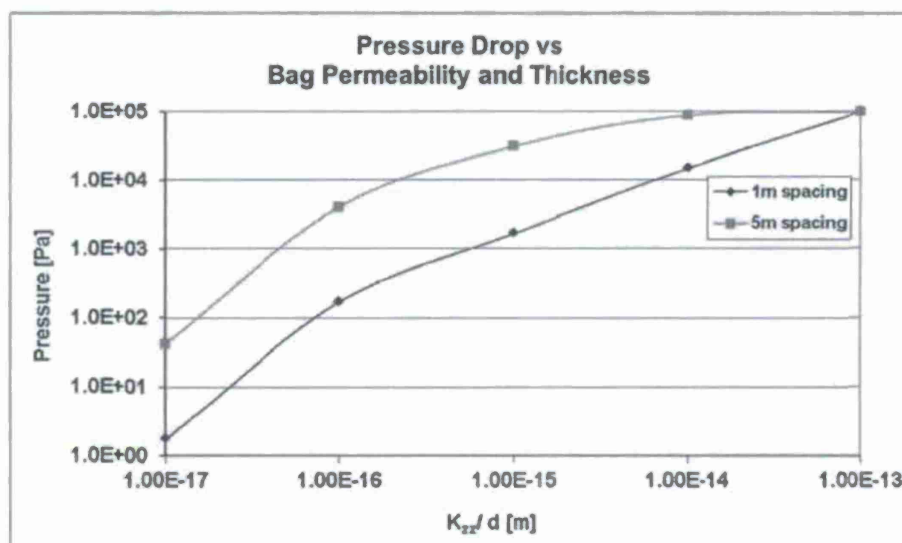


Figure 49: Relationship between bag properties and pressure drop

Development of a permeability cell

A permeability cell with a heating capacity was developed as shown in Figure 50 in order to measure the permeability of different bagging materials versus temperature. Based on an isochoric configuration (constant volume, variable pressure), the cell was pressurized and the air flow through the semi-permeable bag due to the difference in pressure between the cell and the atmospheric pressure is measured [6]. The volume of air passing through the porous bag results in a pressure drop in the cell which can be used to calculate the gas permeability using ideal gas law and Fick's second law of diffusion.[1,4,7].

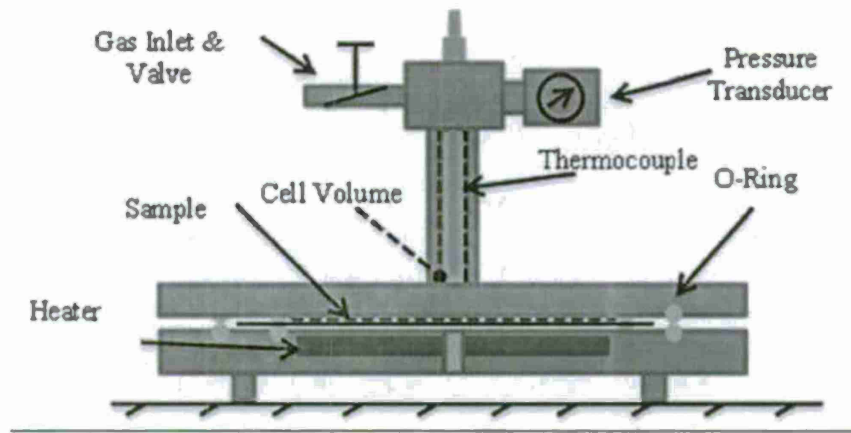


Figure 50: Schematic of the Permeability Cell

An example of a typical data set recorded is shown in Figure 51. An initial pressure of approximately 6.7atm was applied in the pressure chamber and the pressure drop and air volume leaking into atmosphere versus time is measured. It can be seen that for small pressure ranges, the flow rate is almost constant and the volume loss increases linearly (i.e. volumetric flow rate is constant).

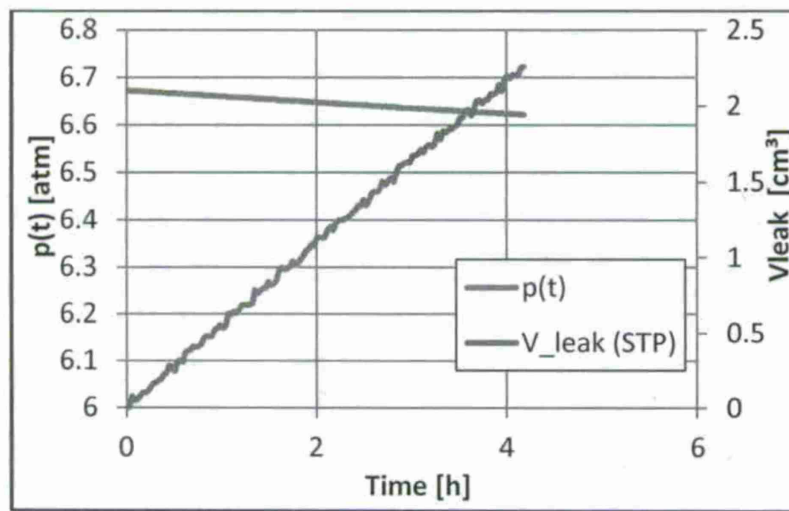


Figure 51: Raw pressure and vacuum leak data

Combining constant cell and air properties as well the pressure differential recorded allows in situ measurement of the permeability ($K_{z,bag}$) using Equations from [8, 9, 10]:

$$K_{z,bag} = \frac{V_{Cell} \cdot d_{Bag} \cdot T_{STP} \cdot (p(t) - p(0)) \cdot \mu}{A \cdot P_{atm} \cdot \left(\int_0^t p(t) dt - p_{atm} t \right) \cdot T_{Sample}} \quad [m^2]$$

$p(t)$...	[Pa]	Pressure in cell at time t
p_{atm}	...	[Pa]	Atmospheric pressure outside of cell
A	...	[m ²]	Surface area of sample
V_{Cell}	...	[m ³]	Volume of cell
d_{Bag}	...	[m]	Thickness of sample
T_{Sample}	...	[°K]	Sample temperature
T_{STP}	...	[°K]	Standard temperature (295.15 K)
μ		[Pas]	Dynamic viscosity of air

It is important to note that during the data reduction the inherent leak rate of the device was quantified and the leak rate through the bag was adjusted accordingly.

Results and Discussion

Various materials used in the industry were tested in order to build an initial database of various bagging materials. The results are shown in Figure 52. Those materials can be classified in two groups. The first group being the films made of nylon and ethylene while the second is comprised of the polyureas and silicone materials being considered for spray bag applications [11].

	Thickness (m)	Material Type	Vendor
Silicone Bag	5.73e-4	Silicone	Smooth-On
APU	2.19e-3	Polyurea	Air Products
Baytec 3695	1.90e-3	Polyurea	Bayer Material Science
Baytec SPR	2.0e-3	Polyurea	Bayer Material Science
ETFE	1.20e-04	Ethylene	Arlon STD
Vacu Pak	9.73e-4	PTFE	Airtech
Whrighton	5.08e-5	Nylon	Airtech

Figure 52: Data for various candidates for bagging materials

The pressure data was reduced using Equation 1 and the bag permeability was calculated and is presented in Figure 53. The films used in the composites industry demonstrated a significant lower permeability compared to any of the spray films alternatives being developed. The ETFE film had the lowest permeability of approximately 10^{-23} m^2 . From Figure 48 one can conclude that even a 0.1mm thick bag would meet the bag requirement to reduce pressure gradient below 1% vacuum for a 5m structure. The polyurea alternatives (BAYTEC and APU) showed better permeability values ($\sim 10^{-21} \text{ m}^2$) than the reusable silicone bagging material. These bagging materials would require a film thickness of 1mm for 1m long structures and 10mm for 5m long structures.

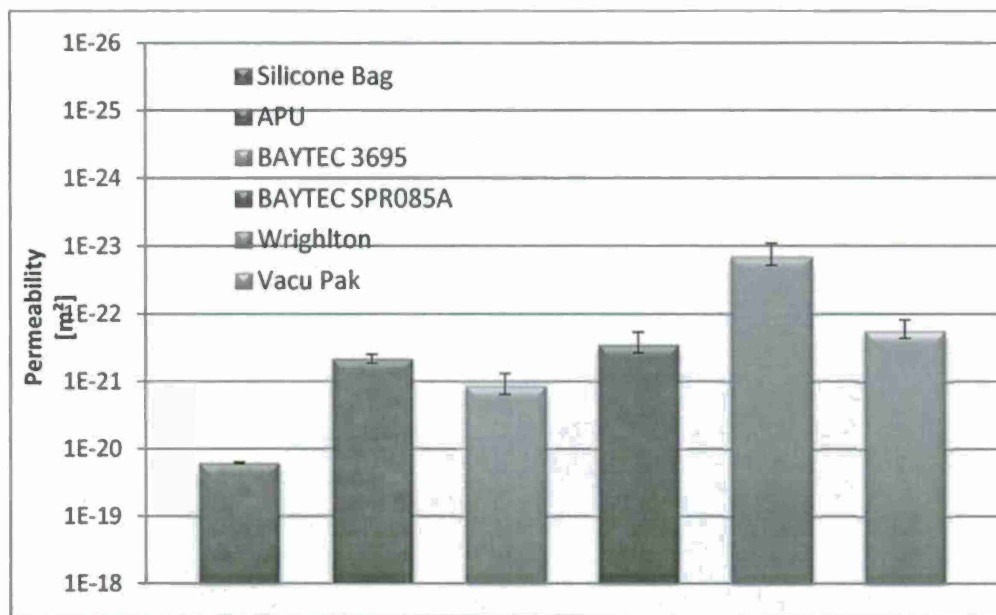


Figure 53: Bag Permeability of different candidate bagging materials

The cell was used to evaluate seven different bags including foil films and reusable bags. The commercially available films showed a nearly 2-order of magnitude lower permeability compared to the reusable silicone bag. The information can now be used to optimize the selection of bag material and thickness as a function of vacuum pressure process requirements and part size.

This task established the barrier requirements for bagging structures using a modeling approach. It relates the bag permeability and thickness to the pressure drop under the bag as a function of breather properties and part size. In addition, a bag permeability cell was developed which measures the pressure drop in an air cylinder as the gas flows through the bag. A data reduction is implemented to evaluate the bag permeability. Various commercial available bagging films and newly developed reusable bagging structures were evaluated. The films show a 2-order lower permeability compared to the reusable bagging approaches. Current reusable bagging materials must be significantly thicker to provide equivalent barrier properties or they should be limited to applications for smaller size structures.

The path forward consist into developing our spray on bag using the ABB six axis robotic arms presented in task IV. By combining the robotic arm and the industrial spray on equipment we will be able to replicate large scale bagging process at a smaller level. The process will then be optimized and tailored to obtain a film meeting our bagging requirements.

References

- [1] Crivellivisconti, I., & Langella, a. (1992). Analytical modelling of pressure bag technology. *Composites Manufacturing*, 3(1), 3-6. doi:10.1016/0956-7143(92)90176-U
- [2] Brouwer, W. D., van Herpt, E. C. F. C., & Labordus, M. (2003). Vacuum injection moulding for large structural applications. *Composites Part A: Applied Science and Manufacturing*, 34(6), 551-558. doi:10.1016/S1359-835X(03)00060-5

- [3] Fernlund, G. (2010). Risk reduction in composites processing using prototype data, process simulation, and Bayesian statistics. *Composites Part A: Applied Science and Manufacturing*, 41(2), 295-303. Elsevier Ltd. doi:10.1016/j.compositesa.2009.10.021
- [4] Buckingham, R. (1996). Automating broad goods the manufacture of composite. *Composites*, 27(3), 191-200.
- [5] Correia, N. C., Robitaille, F., Long, C., Rudd, C. D., Šimáček, P., & Advani, S. G. (2005). Analysis of the vacuum infusion moulding process: I. Analytical formulation. *Composites Part A: Applied Science and Manufacturing*, 36(12), 1645-1656. doi:10.1016/j.compositesa.2005.03.019
- [6] Correa, C., & Klein, a. (1990). Measurement of permeability, diffusion and solubility coefficients. A testing method. *Polymer Testing*, 9(4), 271-277. doi:10.1016/0142-9418(90)90013-4
- [7] Moore, T. T., Damle, S., Williams, P. J., & Koros, W. J. (2004). Characterization of low permeability gas separation membranes and barrier materials; design and operation considerations. *Journal of Membrane Science*, 245(1-2), 227-231. doi:10.1016/j.memsci.2004.07.017
- [8] Paul, D. R., & DiBenedetto, a T. (2007). Diffusion in amorphous polymers. *Journal of Polymer Science Part C: Polymer Symposia*, 10(1), 17-44. doi:10.1002/polc.5070100105
- [9] Schowalter, S. J., Ñ, C. B. C., & Doyle, J. M. (2010). Nuclear Instruments and Methods in Physics Research A Permeability of noble gases through Kapton , butyl , nylon , and “ Silver Shield ’.” *Nuclear Inst. and Methods in Physics Research, A*, 615(3), 267-271. Elsevier. doi:10.1016/j.nima.2010.01.041
- [10] Modi, D., Johnson, M., Long, A., & Rudd, C. (2009). Analysis of pressure profile and flow progression in the vacuum infusion process. *Composites Science and Technology*, 69(9), 1458-1466.
- [11] Applications 5469686. (n.d.). , 1110-1110.
- [12] Li, H., Jiao, J., & Luk, M. (2004). A falling-pressure method for measuring air permeability of asphalt in laboratory. *Journal of Hydrology*, 286(1-4), 69-77. doi:10.1016/j.jhydrol.2003.09.013
- [13] Meindersma, G. W., Reith, T., & Haan, A. B. D. (2002). Method for experimental determination of the gas transport properties of highly porous fibre membranes: a first step before predictive modeling of a membrane distillation process. *Science*, 147.

Task VI: Smart Prepregs and Composite Materials

Motivation and Background:

Advances in the understanding of nanocomposite structure/property relations have enabled scientists and engineers to produce functionally tailored matrix and fibers which have coupled electromagnetic and mechanical properties. In particular, carbon nanotubes can form electrically conductive networks at small concentrations in a polymer matrix and displays piezo resistive behavior [1-3]. Due to their vast difference in scale carbon nanotubes can form networks around the structural fiber reinforcement (Figure 54) and be utilized to sense damage based on breaking-up of the nanotube network (Figure 55). Nanotubes impart inherent damage sensing capabilities to probe the bulk of the material [4-6]. Typically, this measurement method relies on relating the bulk changes of the DC conductivity and low frequency dielectric properties of the composite doped with carbon nanotubes to provide insight into the overall material behavior and damage accumulation. Due to its capability to detect micro cracks, non-invasiveness and potential for scaling up, the technology to detect damage using carbon nanotubes is by far the most promising technique for Structural Health Monitoring (SHM) of composite materials. Hence incorporating carbon nanotube networks inside composite materials is the key towards the development of future smart composite materials. The present research is geared towards utilizing high frequency electromagnetic measurement techniques discussed in the next section to monitor the change in CNT networks inside the composite matrix. This is an extension of DC based measurements.

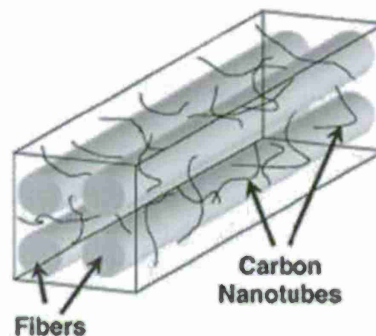


Figure 54: Three-dimensional model showing the penetration of nanotubes throughout a fiber array due to their relative scale ([7])

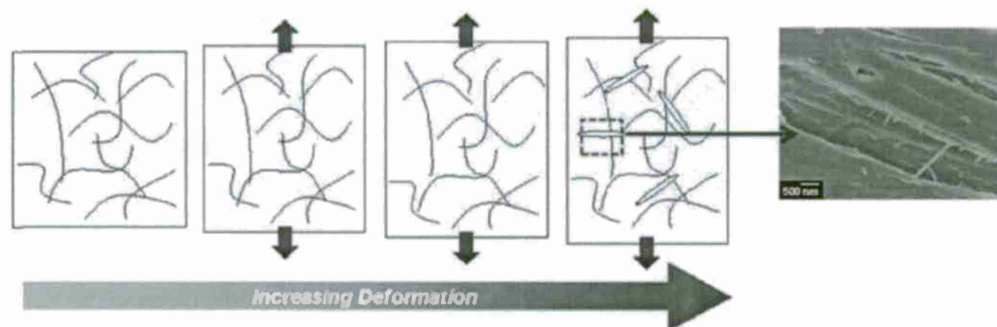


Figure 55: Sensing of damage due to piezoresistive behavior of CNT networks

Electric time domain reflectometry (TDR)

Electric Time Domain Reflectometry (TDR) is a high-frequency electrical measurement technique that can detect spatial changes in dielectric properties. TDR system consists of a Giga Hertz range signal generator which generates a picoseconds rise time pulse and detects the reflection of the pulse in intervals of nano seconds. Based on the incident pulse and the reflected pulse, the system under observation is analyzed. Figure 56 shows the basics of a TDR measurement system.

A key advantage of the TDR technique is in the potential for distributed measurement as the TDR signal provides time-domain feedback as a function of the local dielectric material property and transmission line geometry. The TDR approach has been utilized for fault detection in printed circuit boards and cables [8] and also for geological measurements to monitor soil moisture content and faults in rock [9]. In addition, TDR approaches have been used for flow monitoring in liquid composite molding [10], distributed strain sensing [11] and as a test method to measure the crack length in the double cantilevered beam (DCB) fracture toughness tests [12]. Recently, TDR has been used to study defects in concrete structures [13,14] but the scale of faults in these structures is macroscopic as opposed to microscopic scale damage which initiates in composites.

For fiber composites the scale of damage ranges from the scale of microns (microcracks, fiber/matrix debonding) to centimeters or larger (ply delamination). The length scale resolution of the TDR measurement is directly proportional to wavelength of the electromagnetic signal, which in turn is inversely proportional to the frequency. With recent advances in microwave engineering and the advent of picoseconds rise time and Gigahertz frequency pulses, TDR has been used to probe length scales providing high enough resolution to measure many of the damage modes observed in composites. Through nanoscale hybridization and localized tailoring of the dielectric properties it is likely that the scale can be extended to detect microcracks. The TDR approach also overcomes some challenges for SHM since the sensors are non-invasive; they can be surface mounted yet detect sub-surface damage *in situ*. Furthermore, the technique is not affected by vibration and other acoustic events.

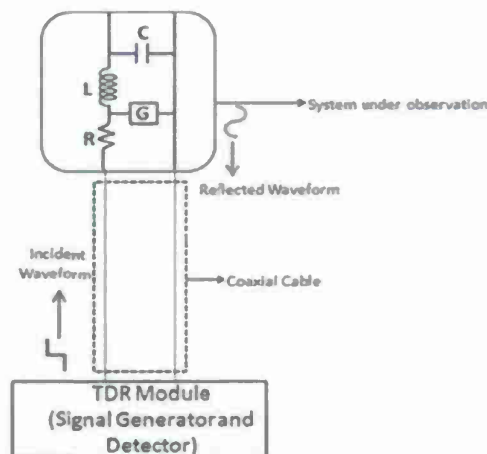


Figure 56: Basics principle of a TDR system

In case there is only one discontinuity in the transmission line, it is easy to compute the magnitude of that discontinuity using TDR module parameters and the parameters of the cable connecting the TDR module to the system under observation. But in case of multiple discontinuities, a 'TDR inversion' algorithm must be used to take into account multiple reflections. While several TDR inversion algorithms to interpret the TDR data have been developed ([15-18]), these algorithms are not meant for real time *in-situ* application due to the long time taken to analyze the data. In the present research, an attempt will be made to come up with efficient algorithms for TDR inversion.

Objectives and Goals:

The objective of present research is to develop self-sensing smart composite material systems for structural applications. In particular, the sensing capabilities to sense strain, damage and degree of cure are being emphasized on. The research objectives can be broken down into following major areas: material and process development, experiment design, sensing and instrumentation, modeling and simulation

1. Materials and process development: The present research is aimed towards conceptualizing and manufacturing smart material systems, and fabricating coupon level or larger test specimen and evaluating their self-sensing capabilities using laboratory tests. The effect of process parameters, for example: the effect of dispersion of CNTs on self-sensing properties will be explored. The processes have to be scalable to enable structural application of the smart material system developed.
2. Experiment design: For evaluating the SHM capabilities of smart materials thus developed, experiments will be designed to induce changes in the material system (micro cracks, transverse cracks, delamination, failure) due to applied environmental loading (stress, impact etc). For evaluating the cure monitoring capabilities, proper environmental conditions (isothermal, temperature ramp etc) will be figured out and implement in laboratory.
3. Sensing and instrumentation: Real time sensing and instrumentation to enable *in-situ* sensing of strain, damage and degree of cure of the smart material system will be implemented. Instead of traditional point sensing, TDR based sensing will be implemented. LabView® will be used for real time data acquisition.
4. Modeling and simulation: Electromagnetic modeling is essential to optimize sensor configuration. Analytical models and commercial electromagnetic modeling software will be used to model and optimize the sensor output. A TDR inversion algorithm suitable for real time implementation to model and invert a transmission line with multiple discontinuities will be developed.

Approach

Once a self-sensing smart composite material has been conceptualized and developed, the system response to environmental loading was evaluated experimentally. Existing sensing systems such as load measurement, strain measurement, acoustic emission, C-Scan, optical microscopy, differential scanning calorimetry, thermometry etc were used to compare the existing sensing methods with present research. Smart materials were compared to baseline materials to observe the effect of nano-scale reinforcements. Parallel work in sensing/instrumentation and

modeling/simulation was continued to enable real time sensing and optimize the sensor response respectively. Figure 57 shows the generalized methodology for both SHM and process monitoring. Design, evaluation and optimization was implemented with a feedback between the evaluation and design loops through optimization loop. In the design loop, baseline composite precursors are combined with nanoscale reinforcements to form multifunctional composites. Novel sensing techniques, for example, TDR, resistance monitoring etc. are selected depending upon the characteristics of multifunctional materials designed. The evaluation loop consists of experimental data acquisition and its comparison with traditional sensing techniques such as strain monitoring, acoustic emission, C-Scan, optical microscopy, differential scanning calorimetry, thermometry etc. If the multifunctional materials designed in the design loop satisfy the sensing requirements, the optimization loop is used to design and optimize both the sensor configuration and nanoscale reinforcements using electromagnetic simulations; for example, sensor geometry and/or CNT loading in the multifunctional composite can be varied using the output from electromagnetic simulations. Using the feedback from the optimization loop, the improved multifunctional composites will be fabricated and tested using the optimized TDR sensors. The evaluation loop will again be used to experimentally validate the performance of the sensors designed in the previous step.

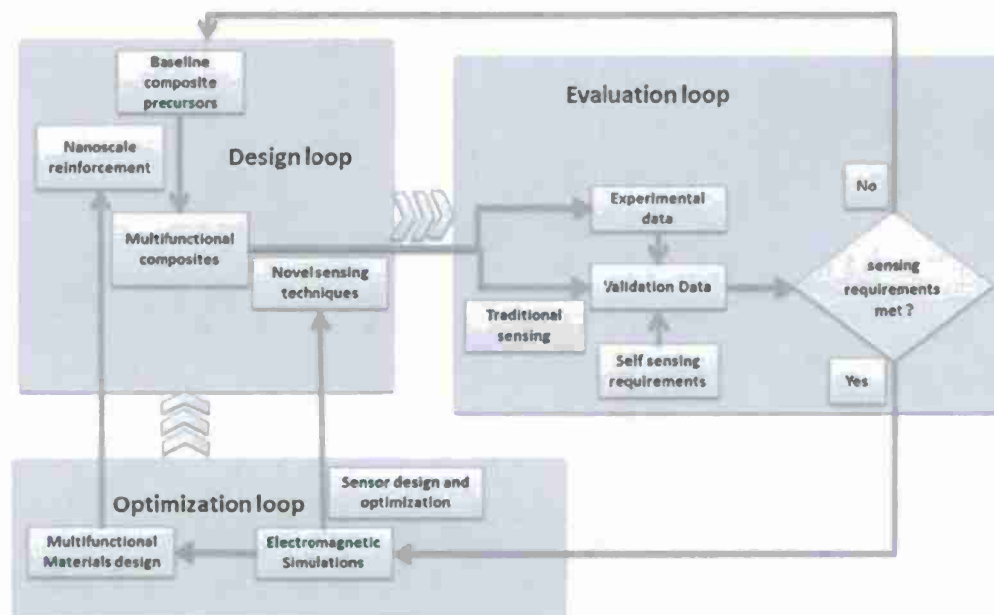


Figure 57: Research methodology

Figure 58 shows the outline of experimental validation to access the performance of multifunctional composite materials coupled with the novel sensing techniques. Acoustic emission, optical microscopy, strain & stress monitoring and microscopy are used to access the structural health monitoring characteristics. DSC, thermometry and visual flow monitoring (using digital image processing) will be used to access the manufacturing process monitoring characteristics of multifunctional composite materials developed in this research.

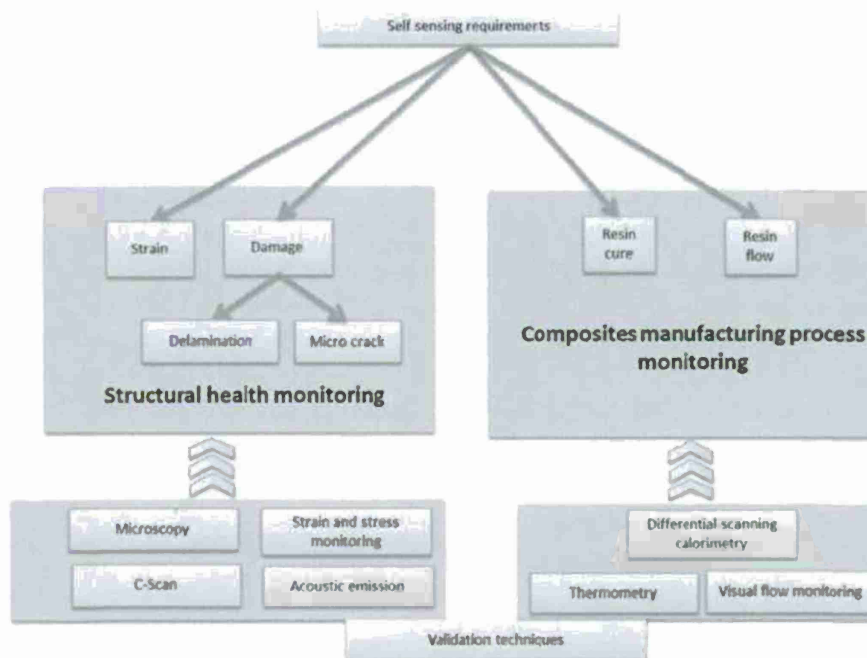


Figure 58: Outline of experimental validation

Results and Discussion:

TDR based of SHM of CNT modified composite

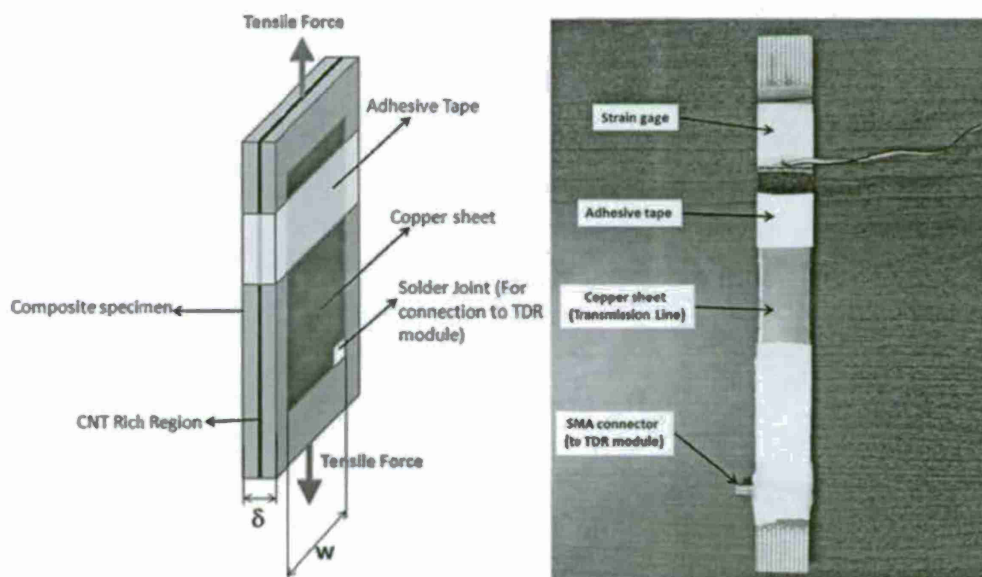


Figure 59: Parallel Plate transmission line with carbon nanotube sized sample (Similar copper sheet on other side of the specimen). More adhesive tapes were used, fully covering the copper sheet.

A custom data acquisition system was developed to track the TDR signals and compute the difference between the original baseline TDR trace and all subsequent traces. Load, strain and the TDR signals were further integrated to assess the real-time response. The TDR module

acquired an incident/reflected signal approximately every 1 second. Standard strain gauges were mounted on the specimen surface as shown in Figure 59 and continuously monitored using a National Instruments DAQ system.

In addition, conventional damage detection and assessment techniques were utilized for validation of the observed TDR sensing response. Acoustic Emission (AE) measurements were used to non-invasively monitor the progression of damage due to micro-cracking. An AE sensor (35–100 KHz, Physical Acoustics, Princeton Junction, NJ) was placed on the surface of the specimen and measures the number of elastic wave pulses generated during each crack. Microscopic edge replication was utilized to track the state of damage in the specimen at different stages of loading.

Tensile testing under a progressively increasing cyclic loading profile with step size of 1000 N was applied using a displacement controlled load frame (Instron 5567) at 1.26 mm/min. At each loading step the machine was stopped for approximately 2 minutes and the load was subsequently released with the same rate. During the hold under tension, microscopic edge replicas were acquired by applying an acetate replica tape to the specimen (Ted Pella, Inc.). Optical micrographs of edge replicas of the laminate were taken at various loading steps and reveal the progressive micro crack damage accumulation.

Stepwise cyclic loading in steps of was applied to both specimens (Figure 60a). Figure 60 b summarizes the stress-strain behavior. An almost identical stress-strain response is observed for all loading cycles, indicating that the carbon nanotubes did not change the overall elastic properties as compared to the baseline. The slope of the stress-strain curve decreases slightly after the 4th loading cycle (4000N or approximately 150MPa) indicating a reduced stiffness after the loading has been applied. The stiffness reduction is due to damage accumulating in the sample, in particular, micro-cracking in the 90° layer.

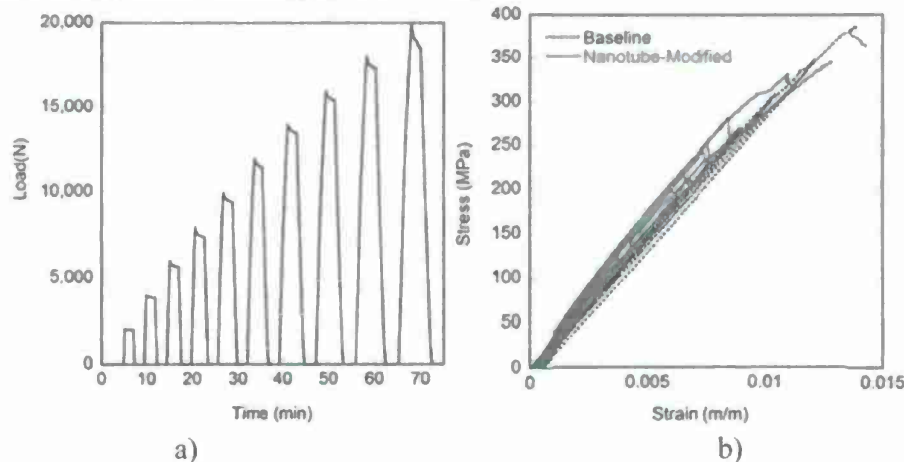


Figure 60: a) Applied loading to both the specimen and b) stress strain behavior for both samples.

The effective impedance change between 150 ns and 153 ns was calculated (Figure 61). At the peak of 9th loading cycle prior to total failure of the specimen, an impedance change of approximately 5.5Ω in the carbon nanotube specimen is seen versus 2Ω in the specimen without carbon nanotube indicating significantly higher sensitivity in the carbon nanotube specimen. The standard deviation of the measurement of the TDR system is approximately 0.039Ω and 0.034Ω

for carbon nanotube introduced and baseline specimens respectively. Two observations can be made from the Figure 61. First, the TDR data seems to follow the loading cycle. Increasing the specimen stresses or strain increases the effective impedance of the specimens, while reducing the tensile load reduces the impedance. Secondly, a hysteresis behavior is seen where the TDR response does not reach original impedance values when the specimens are unloaded. This is particularly true for the carbon nanotube modified specimen and for higher peak loads.

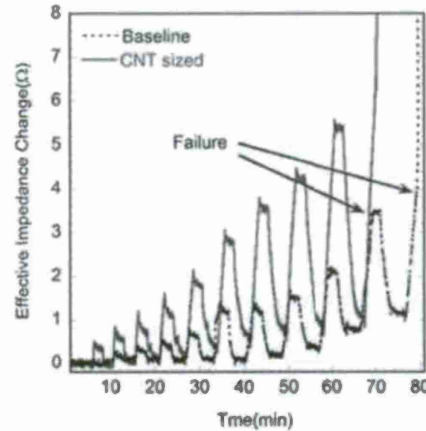


Figure 61: Effective impedance change for carbon nanotube sized and baseline specimen under progressively increasing cyclic loading.

Figure 62 illustrates this behavior in more detail. The maximum impedance change is plotted for each loading cycle during the peak (Figure 62a) load hold stage and unloaded/unstrained stage (Figure 62b). At a higher peak load, higher impedance is observed for both the baseline and the carbon nanotube introduced specimen. However, the carbon nanotube introduced specimen shows higher impedance sensitivity due to the fact that carbon nanotubes have coupled electrical and mechanical properties [1-3]. The peak data suggests a linear relationship between stresses/strain and the TDR signal until the 3rd to 4th load cycle, with an increasing TDR response afterwards.

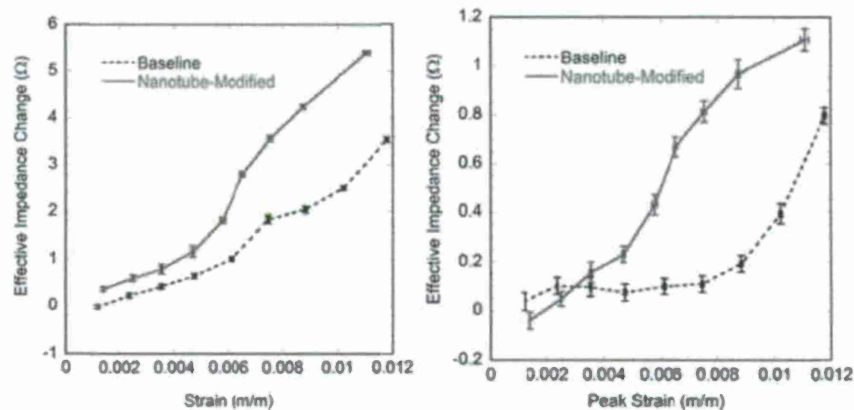


Figure 62: Impedance Change for each consecutive loading step a) at peak load plotted with peak strain and b) during unloaded stage plotted with previous peak strain

The unstrained baseline and Carbon nanotube modified specimen show a different TDR response (Figure 62 b). In Figure 62 b, the permanent impedance change is plotted against the peak strain

undergone by the specimen in previous cycle. The impedance of the specimen without carbon nanotube falls back to its original value as the specimen is unloaded until the 6th to 7th cycle while a significant impedance change is observed in the carbon nanotube introduced specimen starting with the 4th cycle. The hysteresis behavior can be attributed to permanent breakage of carbon nanotube interconnects within the sizing layer [19]. After the seventh loading cycle, the micro cracks coalesce to form delaminations between the plies. At this stage of higher damage, even the baseline composite shows a permanent impedance change. Increasing the load further does lead to permanent damage in both specimens and significant impedance residuals.

The test specimens were designed to introduce micro-cracking in the center ply even at intermediate loading conditions. In the previous section, several observations of the TDR and strain sensor data suggested damage accumulation after the 3rd loading cycle for the carbon nanotube sized specimen or 4th loading for baseline specimen. AE tests and micrographic tests were conducted to validate the damage mode. Figure 63 (a) and (b) show the accumulated AE Counts versus time for baseline and carbon nanotube modified specimens respectively.

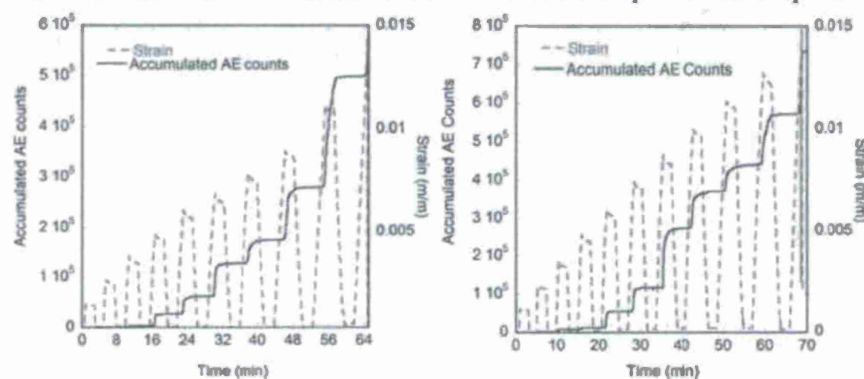


Figure 63: Acoustic emission studies of: a) CNT sized specimen b) Baseline specimen.

It can be seen that after the 3rd loading cycle for the carbon nanotube sized specimen or 4th loading for baseline specimen, the acoustic hits significantly increase. This suggests development of damage due to transverse cracking. As a consequence the permanent change observed in the impedance of unloaded impedance of carbon nanotube introduced specimen during 3rd-4th loading step onwards is micro-cracking. The micro-cracking results in transverse cracking which shows a large number of acoustic hits for higher loading cycles. An important observation is that even though the acoustic emission plots are similar for both the baseline and the carbon nanotube introduced specimen, the unloaded impedance changes observed are markedly different. While the carbon nanotube introduced specimen enable a much earlier indication of damage, the baseline specimen show a significant impedance changes only at the delamination stage.

Visual inspection of the specimens using micro graphs of edge replicas further validate the occurrence of micro cracks in the specimens. Figure 64 shows micrographs of edge replica of both the specimens at 2nd, 4th and 7th loading cycle. The micrographs indicate similar progressive damage accumulation in both the carbon nanotube introduced and baseline specimen.

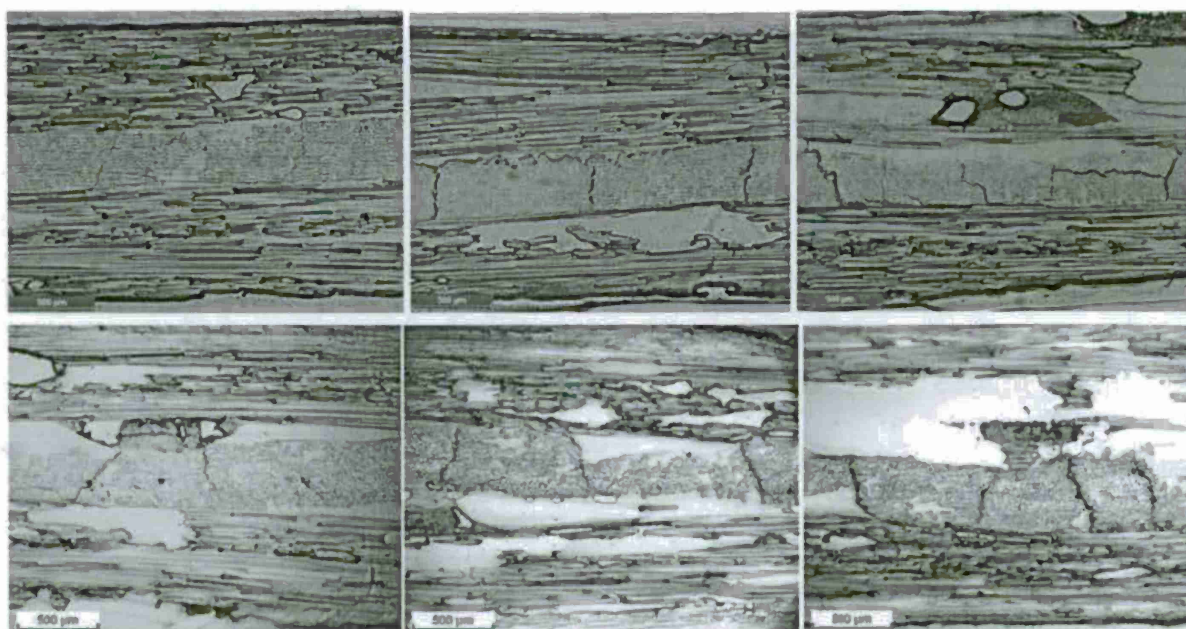


Figure 64: Micrographs of Edge Replicas of baseline (a) and carbon nanotube loaded (b) laminate at various loading stages: (left) 2nd loading step (4000N). (center) 4th loading step (8000N). (right) 7th loading step (14000 N)

It can be seen that during the 2nd loading step, microscopic damage is initiated. At the 4th loading step, the specimen has a significant accumulation of transverse cracks. The formation of these transverse cracks results in higher acoustic hits observed around 3rd - 4th loading cycle. The formation of microscopic cracks as well as transverse cracks results in permanent impedance change of carbon nanotube introduced specimen. Finally, at near failure loading cycles (7th loading step and beyond), these transverse cracks start coalescing to form delamination's which results in a permanent impedance change of both carbon nanotube introduced and baseline specimen.

All sensor and image data suggest that the accumulation of micro-cracking starts around the 3rd or 4th cycle, leading to delaminations and stiffness reduction and ultimately total failure of the specimens. Nevertheless, the TDR system provides this feedback non-destructively with the integrated sensor at a significantly higher sensitivity compared to the stiffness reduction measured by the attached strain gauge system. In addition, at zero load level the TDR system provides a change in signal which can be related to the permanent damage of the specimen. For the specimen with the carbon nanotube layer, small-scale damage is detected significantly earlier with the TDR system compared to the baseline. The TDR sensor is also sensitive to strain and thus provides multi-functional feedback of the state of the specimen.

TDR based composites manufacturing process monitoring

Figure 65 shows the smart tooling and Figure 66 illustrates the experimental details of the setup used for flow and cure monitoring experiments conducted with the smart tooling. Preform consisted of two layers of E-Glass, 20"X6" dimensions. Infusion was done in the direction of the longer side of the preform. Distribution media of dimensions 15"X4.5" was placed on top of the

preform. A CCD camera was placed above the setup to monitor flow front on the top. A digital image processing based flow monitoring system programmed in LabView® was used to estimate flow front location using images acquired by the CCD camera.

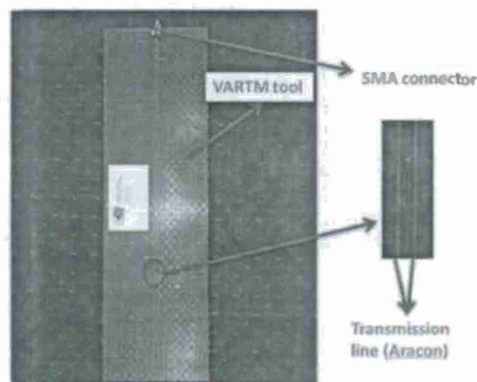


Figure 65: Smart tooling with embedded ARACON® transmission line

The bottom flow was monitored by the TDR transmission lines embedded in the tooling. Flow and cure monitoring experiments were conducted using the following resin systems: i) Derakane with MEKP(2%) as curing agent and Cobalt-Naphthenate(0.3%) as initiator ii) Derakane with Trigonox(1.5%) as curing agent, Cobalt-Naphthenate(0.2%) as initiator and Acetyl Acetone (0.05%) as inhibitor.

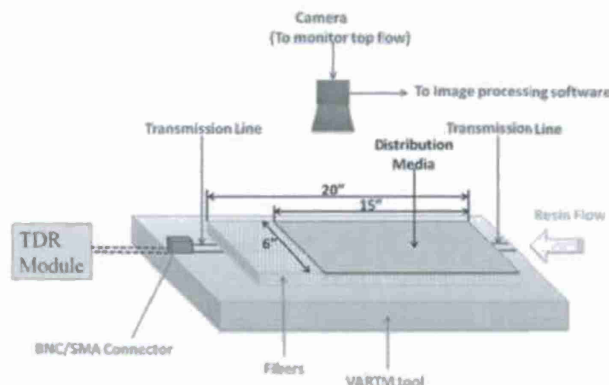


Figure 66: Experimental setup for online flow and cure monitoring using smart tooling.

Figure 67 shows the experimental results for flow monitoring conducted using Epoxy SC-15 resin system. It can be seen that flow monitoring using the smart tool gives close correlation with the camera data. Good correlation was found for Derakane as well. As the distribution media of length 15" was used, it can be seen that the flow speed decreases once the flow reaches past 15" from the infusion point.

For evaluating the capability of smart tooling for cure monitoring purpose, the composite part fabricated on the smart tooling was allowed to cure at room temperature (23°C). A thermocouple was used to monitor temperature data during the curing of resin to make sure that the temperature remained near 23°C. Isothermal differential scanning calorimetry (DSC) experiments at 23°C were conducted to verify the cure behavior as predicted by the TDR measurements. Results of the cure monitoring experiments are shown in Figures 68.

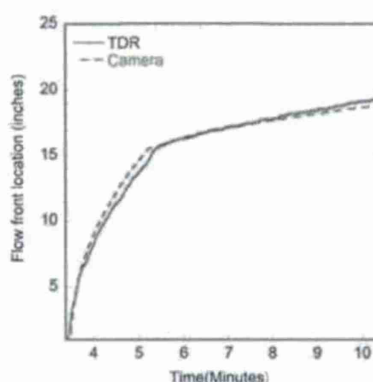


Figure 67: Results of flow monitoring for Epoxy SC-15 resin.

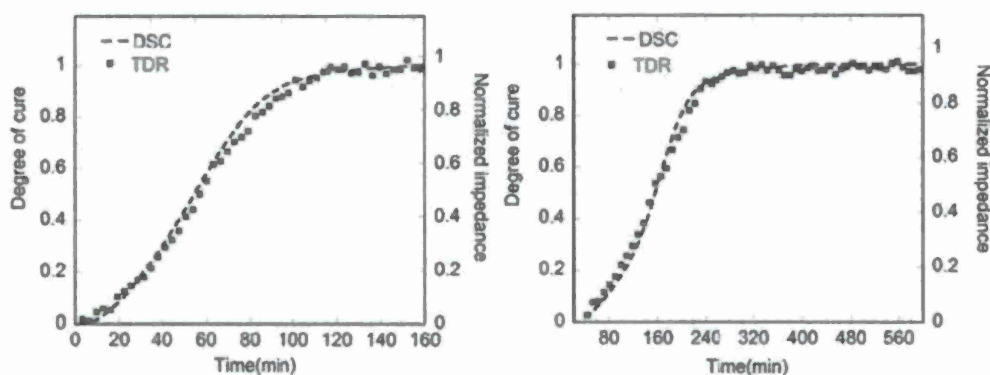


Figure 68 Comparison of cure monitoring data obtained from DSC and TDR for (a) Derakane with MEKP(2%) as curing agent and Cobalt-Naphthenate(0.3%) as initiator. (b) Derakane with Trigonox(1.5%) as curing agent, Cobalt-Naphthenate(0.2%) as initiator and Acetyl Acetone (0.05%) as inhibitor.

It can be observed from Figure 68 that smart tool with embedded transmission line can be used a reliable method to monitor flow front progress and cure as well. The dielectric constant is expected to change only as the composite part cures. Once the part has fully cured, the dielectric constant will not change further. A similar trend is observed in Figure 68. As the normalized impedance is a function of dielectric constant, it changes only as long as the resin cures. A remarkable similarity in degree of cure and normalized impedance is observed. Hence the cure time predicted by DSC and TDR are identical (140 minutes for system i), 320 minutes for system ii) and 2200 minutes for system iii)).

Whereas DSC is a very reliable method for studying resin cure in a controlled environment, it cannot be applied for online cure monitoring during composites manufacturing. Smart tooling with embedded transmission lines, however can be utilized for both flow and cure monitoring during composites manufacturing. It has the advantage of being completely non-invasive, low in cost and robust. The accuracy compares reasonably well with DSC experiments, which are considered as benchmark for cure monitoring. Even the point sensors (dielectric/thermocouple/DC) have some degree of invasiveness, however small, which can interfere with vacuum bagging (for VARTM experiments). However smart tooling with embedded transmission lines does not interfere with vacuum bagging at all. Also, multiple

sensors are replaced by a single transmission line, thus further lowering instrumentation complexities and hence increasing response time in case a control action has to be performed. The concept can be easily scaled up for large composite parts as well and can be coupled with process control systems.

Path Forward

Research work till now has explored the use of TDR for damage sensing in baseline composite materials, the increased strain and damage sensitivity resulting from CNT modification, scalable selective CNT modification and smart tooling for TDR based flow and cure monitoring. The following key research areas, building up on the present work have been identified

1. **Two dimensional damage sensing using embedded transmission lines:** Only one dimensional TDR based techniques were applied till now. Future work will explore 2 dimensional damage sensing. Figure 69 below shows the concept of two dimensional damage sensing using embedded transmission lines in fiber composites. Using parallel transmission lines and sending TDR pulses from both the ends of each transmission line, it should be possible to create a two dimensional map of the damaged area in a composite. This could be especially helpful for detecting impact damage. If successful, the technique would result in automated damage zone identification. C-Scan will be explored to validate the TDR based damage sensing.

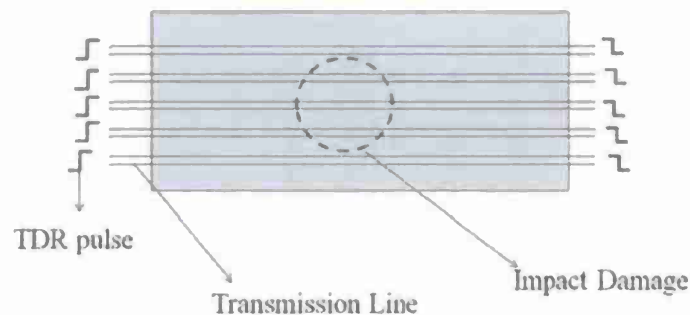


Figure 69: Concept of smart composite structure for 2-D damage detection

2. **Data processing technique for multiple TDR reflections:** TDR data processing techniques used in the preliminary work neglect the multiple reflections when there are multiple discontinuities on a transmission line. Future work will explore data analysis techniques taking into account multiple reflections. This will enable sensing of dry spots during composites manufacturing.
3. **Role of dispersion in TDR sensitivity of CNT based nanocomposites:** Role of Carbon nanotube dispersion on TDR sensitivity will be explored. This will contribute towards not only damage sensing but also re-configurable smart structures for antennae. It is well known fact that dispersion affects the DC conductivity of CNT based nanocomposites. Better dispersion results in greater percolation and hence higher conductivity. The effect of dispersion on high frequency dielectric properties of CNT based nanocomposites has

yet not been investigated. This research task will investigate this phenomenon. Coupling between mechanical and electromagnetic properties will also be explored. Since the transmission line equations are very similar to electromagnetic wave propagation equations, it is envisaged that mechanically altering a structure will result in a different impedance characteristics and hence different electromagnetic characteristics if the structure is used as an antennae. This could be the starting point for mechanically reconfigurable smart antennae systems. Mechanical vibrations could also be used to encrypt the transmitted signal. The complete antennae implementation of such a system is out of the scope of present work as it involves in depth electrical/communications engineering. But the present work will lay a foundation for such systems by demonstrating coupling between mechanical loading and impedance using tensile tests.

4. **CNT based smart sandwich structures:** Sandwich composites are widely used in aerospace, marine and numerous other applications where light weight load bearing structures are required. Hence smart sandwich structures with self-sensing capabilities will be explored. CNT introduction into the core of foam materials will be explored. Figure 70 shows a typical foam core with microspheres and epoxy matrix. While the micro spheres provide weight reduction, they also act as damage initiators due to stress concentrations. CNT networks within the epoxy matrix can be used for automated damage sensing of the foam. Also the effect of micro sphere concentration on electrical properties of the foam will be studied.

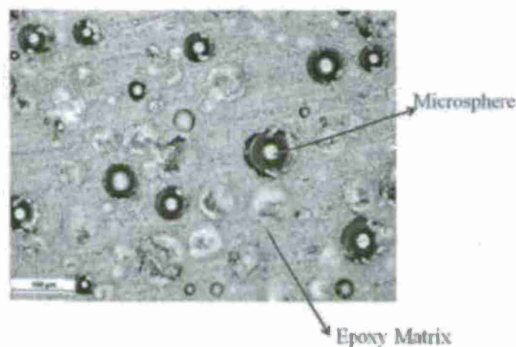


Figure 70: Micrograph of foam with microspheres.

References

1. Koerner H, Price G, Pearce N, Alexander M, Vaia R. Remotely actuated polymer nanocomposites - stress-recovery of carbon-nanotube-filled thermoplastic elastomers. *Nature Materials* 2004;3(2):115-120.
2. Ahir S, Terentjev E. Photomechanical actuation in polymer-nanotube composites. *Nature Materials* 2005;4(6):491-495.
3. Rochefort A, Avouris P, Lesage F, Salahub D. Electrical and mechanical properties of distorted carbon nanotubes RID A-5124-2010. *Physical Review B* 1999;60(19):13824-13830.

4. Thostenson ET, Chou T. Carbon nanotube networks: Sensing of distributed strain and damage for life prediction and self healing RID B-8587-2008. *Adv Mater* 2006;18(21):2837-+.
5. Thostenson ET, Chou T. Real-time in situ sensing of damage evolution in advanced fiber composites using carbon nanotube networks RID B-8587-2008. *Nanotechnology* 2008;19(21):215713.
6. Gao L, Thostenson ET, Zhang Z, Chou T. Sensing of Damage Mechanisms in Fiber-Reinforced Composites under Cyclic Loading using Carbon Nanotubes. *Advanced Functional Materials* 2009;19(1):123-130.
7. Li C, Thostenson ET, Chou T. Sensors and actuators based on carbon nanotubes and their composites: A review. *Composites Sci Technol* 2008;68(6):1227-1249.
8. Smolyansky D, Corey S. PCB interconnect characterization from TDR measurements. *Electronic Engineering* 1999;71(870):63-+.
9. O'Connor KM, Dowding CM. *Geomeasurements by Pulsing TDR Cables and Probes*. Boca Raton: CRC Press, 1999.
10. Dominauskas A, Heider D, Gillespie JW, Jr. Electric time-domain reflectometry distributed flow sensor. *Composites Part A-Applied Science and Manufacturing* 2007;38(1):138-146.
11. Yoon M, Dolan DF, Gabriel S. Time domain reflectometry as a distributed strain sensor. 2008;6932(1):69321R.
12. Obaid AA, Yarlagadda S, Yoon MK, Hager NE, Domszy RC. A Time-domain Reflectometry Method for Automated Measurement of Crack Propagation in Composites during Mode I DCB Testing. *Journal of Composite Materials* 2006;40(22):2047-2066.
13. Lin M, Thaduri J. Structural Damage Detection Using an Embedded ETDR Distributed Strain Sensor. *Sensing and Imaging: An International Journal* 2005;6(4):315-336.
14. Chen G, Mu H, Pommerenke D, Drewniak JL. Damage Detection of Reinforced Concrete Beams with Novel Distributed Crack/Strain Sensors. *Structural Health Monitoring* 2004;3(3):225-243.
15. Bänninger D, Wunderli H, Nussberger M, Flühler H. Inversion of TDR signals?revisited. *Journal of Plant Nutrition and Soil Science* 2008;171(2):137-145.
16. Ching-Wen Hsue, Te-Wen Pan. Reconstruction of nonuniform transmission lines from time-domain reflectometry. *Microwave Theory and Techniques, IEEE Transactions on* 1997;45(1):32-38.
17. Schlaeger S. A fast TDR-inversion technique for the reconstruction of spatial soil moisture content. *Hydrol Earth Syst Sci* 2005;9(5):481-492.

18. Platt IG, Woodhead IM. A 1D inversion for non-invasive time domain reflectometry. *Meas Sci Technol* 2008;19(5):055708.

19. Gao L, Chou T, Thostenson ET, Zhang Z. A comparative study of damage sensing in fiber composites using uniformly and non-uniformly dispersed carbon nanotubes. *Carbon* 2010;48(13):3788.

Task VII Dynamic Response and Damage Tolerance of Sandwich Structures Subjected to Impulse Loading from Sea States and Foreign Object Impact

Motivation and Background

A ship structure experiences impulsive hydrodynamic loading in the severe sea environment. Wave slamming is a crucial concern in the structural design of a high-speed composite marine craft. Idealized slamming pulse has a pressure peak with a very short rise time followed by a relative low plateau pressure with a long tail before returning to zero-pressure. The high pressure peak causes local material or structural degradation. Even if a single slam event is not critical, the high frequencies for many cycles over the lifetime can increase fatigue failures of hull structures. Composite vessels are potentially exposed to structural damages under operation in extreme wave condition.

The analytical solutions predict hydrodynamic loads on a rigid structure for the water impact. Fluid-Structure Interaction (FSI) is however required to be considered to predict resulting structural responses of composite sandwich structures. Numerical modeling techniques have been adopted for calculations including the FSI of the wave slamming in recent years. This task focuses on developing the FEA model of a typical composite sandwich hull shape for water slamming problem.

Objectives and Goals

Slamming pressure on an impacted surface can be predict by analytical solutions, stress waves however propagate inward and might decay until reaching a foam core surface. Pressure pulse can vary as it propagates inside from the face sheet to the core as shown in Figure 71. It is therefore necessary to predict effect of the moving impulsive pressure on the actual foam core stresses. The objective is to determine the actual foam core stresses/strains when the slamming pulse is loaded on the composite sandwich structure.

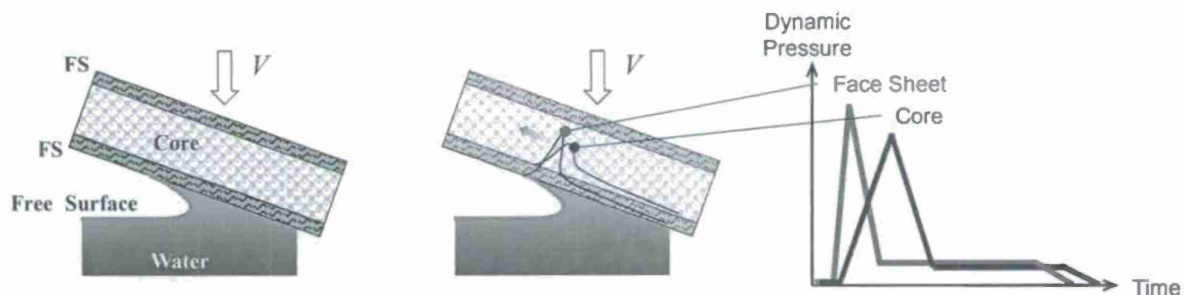


Figure 71: Prediction needed for Effect of Moving Impulsive Loading on Foam Core

Approach

The commercial explicit FEA code, LS-DYNA, is used to study the FSI in the water slamming analysis. The FSI simulation utilizes Arbitrary Lagrangian Eulerian (ALE) Method to couple the interaction between Lagrangian formulation of a structure and Eulerian formulation of fluids. The fluid parts are modeled with Eulerian solid meshes and Gruneisen equation of state. The water domain is filled with the material, while the air domain is defined as initial void region because the effect of air is negligible. The structure representing a V-shaped hull section is modeled with Lagrangian solid meshes. This task started with assuming the structure as rigid in order to validate the modeling against the analytical solutions. **Error! Reference source not found.** 72 shows the FSI model for the water impact in LS-DYNA. The model is a two-dimensional model which defines thin geometry with one element along y-direction and constrains all nodes in this direction. Nonreflecting boundary conditions are defined on the bottom of the water and the side surface of the fluid domains. The structure enters vertically into the water with a constant velocity. Gravity effect is not included.

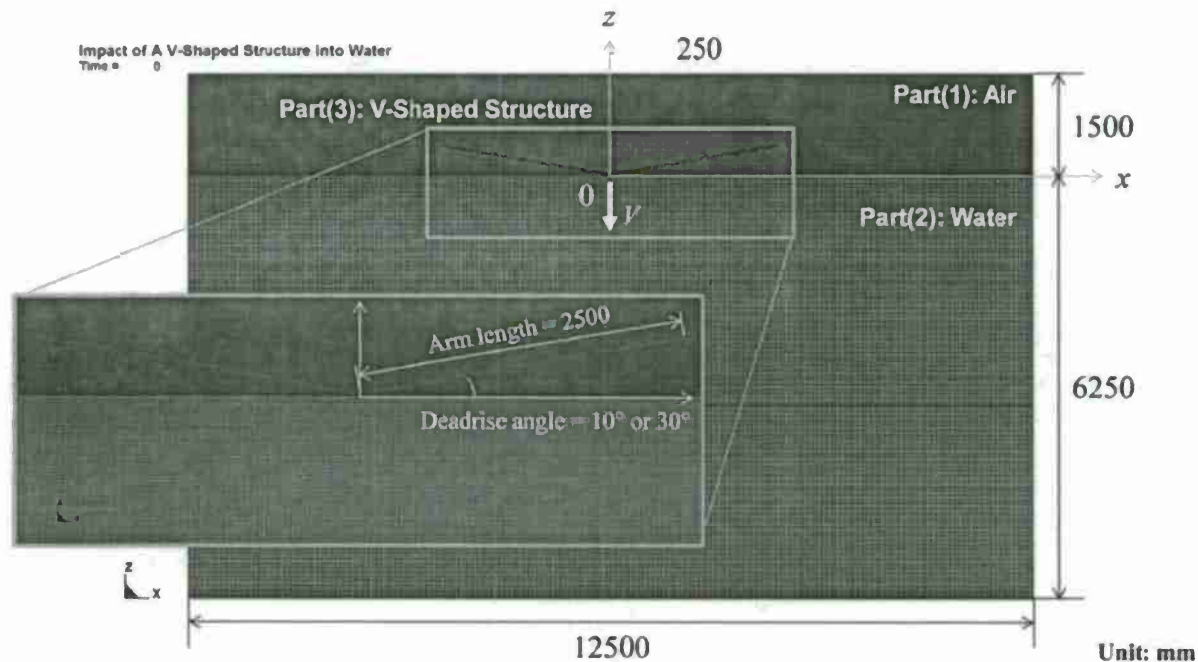


Figure 72: 2-D Fluid – Structure Interaction Model for Slamming Problem

Composite sandwich model will be developed after the validation by the rigid model. The baseline composite sandwich configuration is shown in Figure 73 . Carbon / epoxy face sheets use CF0100/VTM264 prepreg system [1] available from Advanced Composites Group Inc. (ACG). The carbon reinforcement is a 4×4 twill woven fabric with T300 fibers. Eight layers of quasi-isotropic layup are used for both face sheets to form a symmetric sandwich construction, with a stacking sequence of $[((0/90)/(+45/-45))_4/\text{core}/((-45/+45)/(90/0))_4]$. Its nominal thickness is 2.4 mm approximately.

Core material is a styrene acrylonitrile (SAN) polymer base foam with a nominal density of 122 kg/m³ which is designated as Corecell P600 [2] supplied by Gurit. The Corecell P600 is one of the leading structural core materials, and was selected as a representative core material suitable for the usage in marine composite construction. The baseline configuration selected a 38 mm [1.5 in.] thick for hull application. Basically, no adhesive is included at the interface between core and facing. Figure 74 provides a representative stress – strain curve of the P600 under static compressive loading.

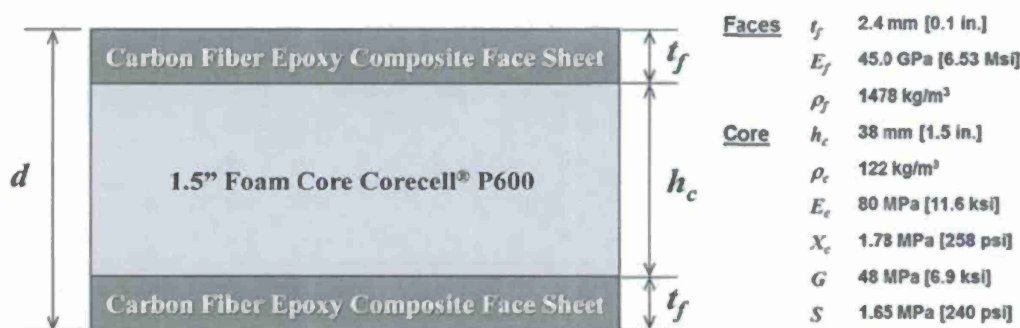


Figure 73: Baseline Composite Sandwich Construction

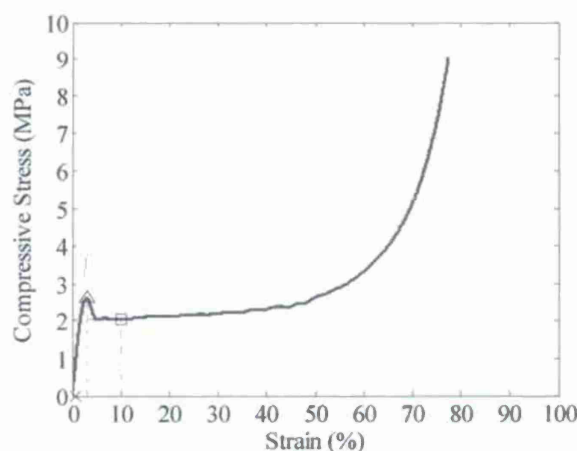


Figure 74: Stress – Strain Curve of P600 SAN Foam Core

Results and Discussion

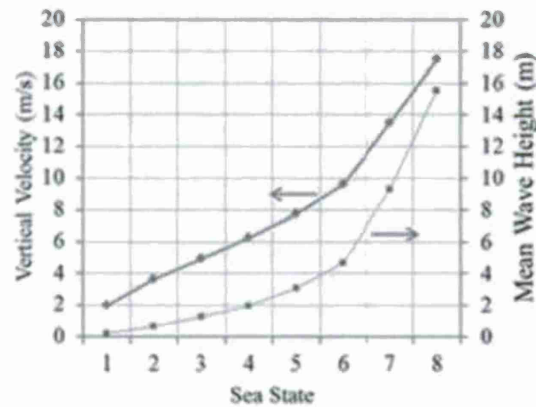
Vertical impact velocity was approximated by the sea state which classifies statistically the wave height as shown in Table 8. The impact velocity can be calculated by the energy conservation in dropping freely from a crest against a trough as

$$V = \sqrt{2gH}$$

where H is the significant wave height depending on the sea state number. The approximation of vertical impact velocity is shown in Figure 75.

Table 8: Sea State Parameters

Sea State	Probability of sea state (%)	Significant Wave Height (m)	Average wave period (sec)	Average wave length (m)
1	0.7	0.20	1.9	4.07
2	6.8	0.66	3.4	12.09
3	23.7	1.23	4.3	19.81
4	27.8	1.98	5.3	28.80
5	20.64	3.05	6.3	41.15
6	13.15	4.67	7.4	57.30
7	6.05	9.27	9.7	97.80
8	1.11	15.54	12.0	149.35

**Figure 75 Approximation of Impact Vertical Velocity**

The 2D water slamming analysis has been performed on a rigid structure. The impact velocity was 9.58 m/s in the negative z-direction corresponding to Sea State 4. The deadrise angle was considered to be 10°. The mesh size for the fluid domain was chosen as 25 mm, and that for the structure is set the same along its span direction as fluids.

Figure 76 shows the predicted slamming pressure histories at different positions of the structure compared with the analytical solution by Wagner (1932) method. The FEA results were filtered by Butterworth filter with cutoff frequency of 1kHz. The predicted pressures reasonably agree with the analytical solutions until the flow separates on the edges of the structure at approximately 0.03 sec. The numerical results however have some high-frequency oscillations which could be reduced when the mesh size is finer. Figure 77 depicts the volume fraction of the fluids before and after the flow separation. Deformed fluid regions can be seen by fringing volume fraction of ALE elements. A volume fraction of 1.0 indicates that an element is completely filled with the water, while a volume fraction of 0.0 means the complete void region corresponding to the air in this model.

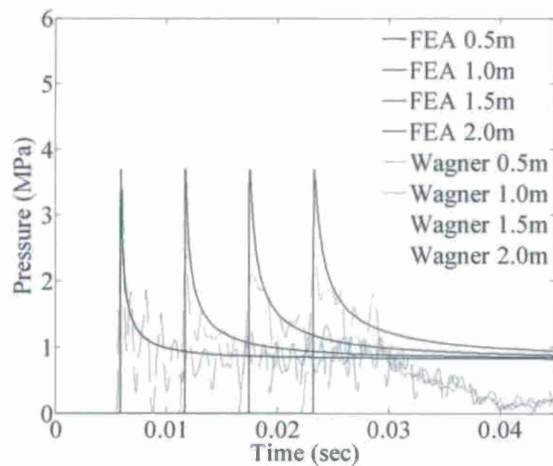


Figure 76: Pressure Time Histories at Different Positions

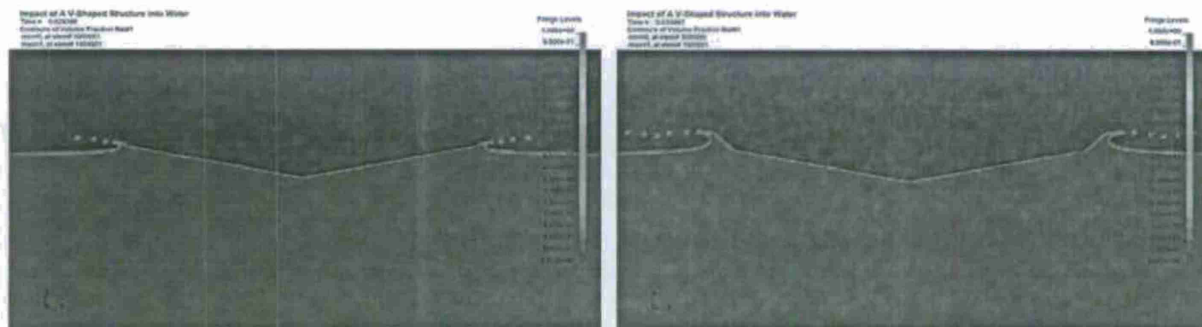


Figure 77: Contours of Volume Fraction of Fluids at 0.029 sec (Left) and 0.035 sec (Right)

Path Forward

The effects of different mesh sizes will be investigated to validate the modeling. The modeling will develop a deformable composite sandwich structure, and predict the actual stresses on the foam core due to the water impact. The previous work reported in the last progress report is not repeated here.

References

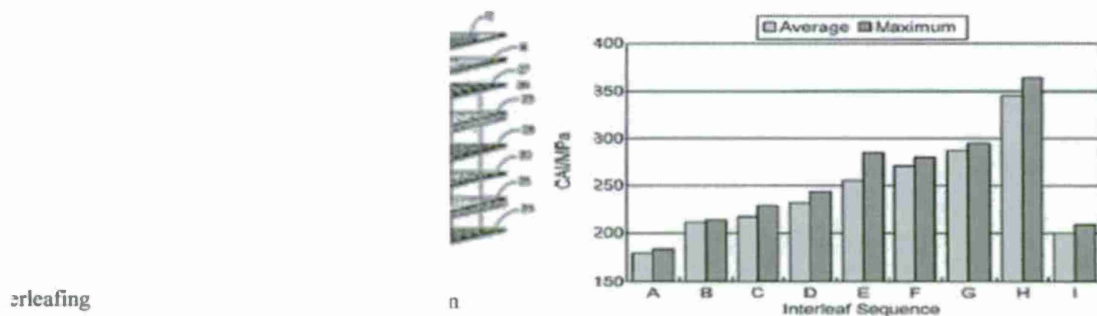
- [1] Advanced Composites Group, ACG VTM260 Series Variable Temperature Moulding Prepreg System, PDS1154/02.09/7.
- [2] Gurit, Corecell™ P-Foam – Structural Core Material, PDS-Corecell P-Foam-7-0511.

Task VII: Improving Impact Survivability of CFRP Sandwiches via Hybridization

Introduction and Background

CFRP sandwich structures have become an increasingly economic solution in ship structures due to advances in composite manufacturing techniques and a growing supply of raw materials. Properly implemented CFRP sandwiches provide a stiff, load-bearing hull that reduces the dead weight of the vessel, allowing for a larger operational load. Unfortunately, the brittle nature of CFRP leads to susceptibility to low-velocity and low energy impact damage that would for the most part leave a traditional metallic hull unaffected. Numerous experiments have demonstrated that impacts at energies as low as 10 joules have the ability to reduce the compressive load-carrying ability of a CFRP sandwich by as much as 40% (Peijs, Venderbosch & Lemstra) due to a complex combination of facesheet and internal failures that often go undetected to the human eye. In naval environments barely submerged objects such as dumped cargo, ice, and organic materials like wood or wave slam can cause significant damage at operational speeds. Consequently, impact durability (both penetration resistance and toughness) of these materials remains a major concern.

Typical techniques for improving the impact response and toughness of composite structures involve ply-dropping toughened fabrics into the layup, thickening of the facesheet on the impact side, or interleaving by using inter-layer materials to increase delamination resistance. (YI & An) The addition of toughened material to the fabric stack improves the impact resistance more than thickening the facing (Gustin, Joneson, Mahinifalah & Stone) and geometric properties have been observed to have large effects on the final properties of the composite (Cantwell & Morton).



An improvement over the baseline CFRP systems impact durability is sought through hybridization of the facesheets, combining baseline carbon fiber systems with high impact resistance layers. Of particular importance is to prevent the impacting object from puncturing the sandwich by arresting its penetration through an increase in the sum of the energy absorption mechanisms that constitute an impact event. These mechanisms include amplified elastic response, fiber pull-out and breakage, delamination, and debonding. (Agarwal, Broutman & Chandrashekhara) Energy absorption should increase due to the toughness increase offered by

substitute plies alone, but maximizing these absorption effects is the overarching goal. A second goal is to mitigate residual load-bearing losses incurred during an impact event. Ideally, a system will be able to not only arrest an impacting object, but continue to bear a larger percentage of its original maximum load than the baseline system.

Approach

The general approach is based on a modified version of the Compression after Impact (CAI) standard (ASTM D-7136, 7137) and the proposed ASTM sandwich standard WK30231, to assess flexural performance of a model sandwich structure before and after impact. The test coupon has 14" x 6" length and width dimensions with a nominal 1/2" inch thick foam core. The width was chosen to accommodate for the maximum damage width criteria of the ASTM D-7136 standard, using a literature review as a guide. The remaining dimensions of the test specimen were determined by reducing the physical ship-scale sandwich design down to a more cost-reasonable size following ASTM C-393 and solving for an equivalent facing/core failure ratio, solving for displacement, and using a given ratio of 3.53: Facings for the baseline sandwich work out to roughly 4 plies per side, and follow ASTM D-7136 for layup configuration.

Materials

Baseline:

The core material is P600 series foam from Gurit and the facesheets are fabricated from carbon fiber prepreg in the VTM-264 family from ACG. The prepreg is a 2x2 twill carbon fabric with a toughened epoxy matrix. Layup is consistent with the recommendations of the ASTM D-7136 standard constitutes a [+/- 45/0/90] layup for each facesheet, with symmetry maintained about the midplane of the sandwich structure.

Hybrids:

Hybrid materials are to be selected based on material properties; mainly that the material has a higher strain-to-failure than the CF baseline with comparable tensile strength and Young's modulus (Cantwell & Morton). Current choices include: Kevlar, Dyneema, Vectran, and S-glass based systems.

Test Coupon Production

Sandwich fabrication follows established processing guidelines for the ACG prepreg, and follows a 16 hr, 65C cure cycle. Coupons are made in batches of 4 from a larger 25" x 15" sample. After layup, the batches are cured over the weekend using the pre-preg manufacturer's suggested cure cycle. Cured samples are then trimmed before being cut down to coupon size using a rotary wet saw and a sizing tool. Trimmings from these coupons are saved for microscopy purposes. Prior to being cut into individual coupons, the batch is C-Scanned for comparison purposes post-impact, and to ensure quality.

Impact Testing

Sixteen total coupons are used to characterize a single material system; 4 coupons are used per impact energy – undamaged, 20, 30, and 50 J impacts. These energies were selected based on the ASTM D-7136 recommendation, the observed energy required to fully puncture the top-facing and pierce into the core, and the energy required to consistently penetrate through the entire coupon, representing total failure. Impacts are performed on a Dynatup 8200 drop-tower, using a constant mass of 12.8143 kg and a 0.625" hemispherical impact tup. Data recorded during the impact event includes displacement, force, and incident velocity. Samples are constrained by clamps on a raised, open-bottomed fixture identical to the one depicted in the D7136 LVI standard.

Post-Impact Testing and Characterization

Following the impact stage, the damaged coupons are C-scanned to assess impact damage. Post-scan, the samples are tested in a ¼ span 4-pt bend configuration using an Instron 4484 testing machine, following the ASTM C-393 standard. Loading rates of 1/10th inch per minute are kept constant, and a LVDT is used to measure displacement in the vertical direction.

Flexural stiffnesses (D11) are calculated by solving equation 9 of ASTM C-393 for Load – deflection ratio, and curve fitting the results over the linear region of the load-deflection curve obtained by the 4-pt bend experiment:

$$\Delta = \frac{11 PL^3}{768 D} + \frac{PL}{8 U}$$

The other physical results; load and deflection, are measured directly from the load cell, or from the LVDT attached to the sandwich. Lastly, Microscopy is performed on the trimmings of the coupons to ensure a low void fraction in the 1-2% range.

Results and Discussion

Baseline Impact Performance

The baseline sandwich structure was tested at 20, 30 and 50 J and the damage cross-sections are shown in the Figure 79 below and damage modes and penetration depths are summarized in the Table 9 below.

	Penetration Depth (in)	Damaged Area (in ²)	Observed Failure Modes
20 J	0.289 (49%)	0.700	Fiber Breakage and Local Core Crushing
30 J	0.540 (92%)	1.680	Fiber breakage, Delamination, and Local Core Crushing
50 J	Through	9.25	Fiber Breakage, Delamination, wide Core Cracking and Crushing

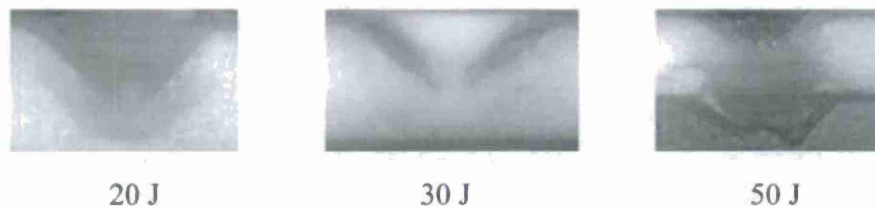


Figure 79: Damage cross sections at baseline impact

Impacted samples were tested in 4-pt flexure per ASTM C 393 and results are summarized in Figure 80. No measurable change in flexural properties is noted, primarily because the selected sandwich structure configuration is core failure driven. Other configurations will be evaluated in the future.

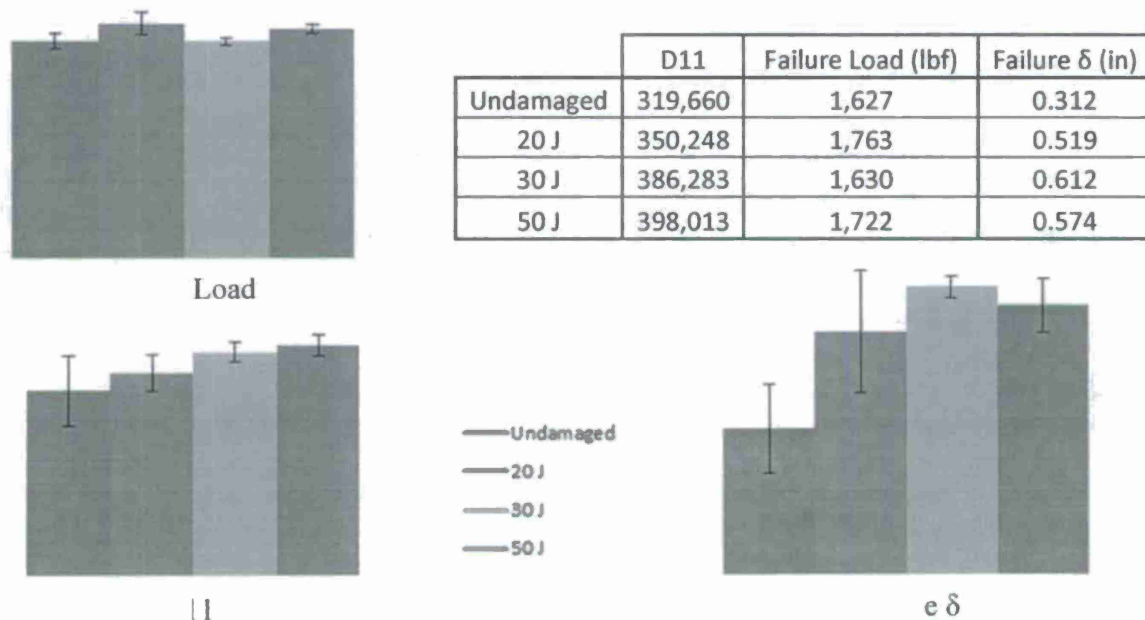


Figure 80: Results of flexural stiffness (D11), Failure load and failure depth

The baseline system does little to impede the progress of the impactor. Core crushing is prevalent in all cases, and at the highest energy level the core begins to crack downwards towards the bottom facing. The damaged area detected by the C-scan rapidly increases as impact energy increases. D11 results are counter-intuitive, suggesting that the coupon is driven by core failure, as opposed to facesheet failure. Failure loads are consistent between the energy ranges, further suggesting that the failure is core-dominant.

Kevlar-Faced Samples

The Kevlar-Faced system was designed to take advantage of the energy-absorbing properties of the Kevlar by placing it on the impact side of the sandwich, as the top layer. The role of the Kevlar layer is to slow or arrest the penetration of the tup while protecting the carbon beneath from breakage, delamination, or other damage. The Kevlar has been added to the layup without

removing equivalent amount of carbon fiber, so the system is expected to perform better both pre and post-damage.

Impact and Scan Results are shown in the Figure 81 and Table 10. Large improvements are seen in impact resistance, with no facesheet damage at 20 J and small degree of facesheet damage at 30 J. At 50 J, we see penetration through the top facesheet, but no penetration of the bottom facesheet, compared to the baseline. Damage area reduction is significant in all cases compared to the baseline

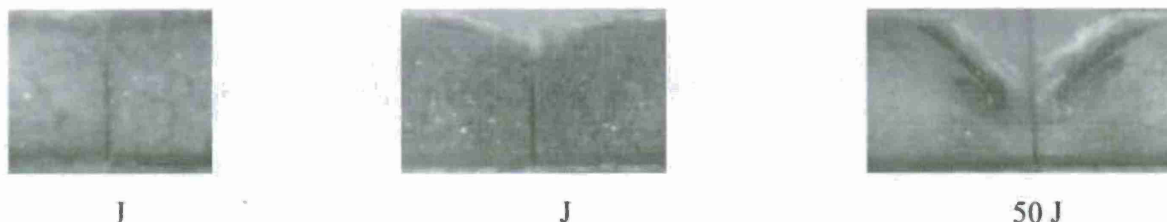


Figure 81: Damage Cross sections with Kevlar facesheet

Table 10: Damage Modes and Penetration with Kevlar faced system

	Penetration Depth (in)	Damaged Area (in ²)	Observed Failure Modes
20 J	0.160 (25%)	0.590	Local, Minimal core crushing
30 J	0.320 (50%)	1.120	Slight delamination and Core Crushing
50 J	0.550 (85%)	1.54	Fiber breakage, Core crushing, and Fiber breakage

A comparison of pre- and post-impact flexural performance shows similar results to the baseline, with no significant change in flexural strength or stiffness, due to core-driven failure in flexure.

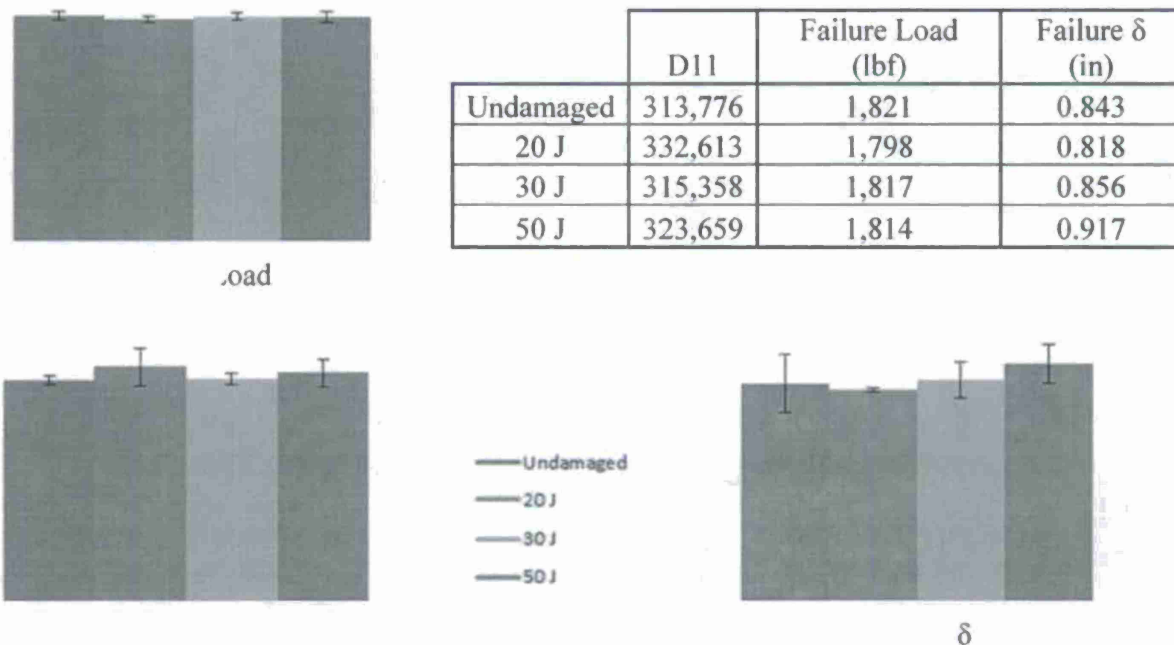


Figure 82: Results of flexural stiffness (D11), Failure load and failure depth for Kevlar faced system

The improvements in impact toughness for the Kevlar-Faced system were significant. The tup was consistently arrested at a fraction of the depth observed in the baseline for equivalent impacts. The failure statistics were pretty consistent, again reaffirming the core-failure hypothesis: not enough of the load is carried by the facing to cause a significant change in the results.

Kevlar-Interleaved Samples

Similar to the previous system, the Kevlar-interleaved system is designed to improve impact performance, but without the flexural stiffness cost associated with the Kevlar-faced system. By placing the stiffer material on the outside of the stack, it is hoped that the layup will retain or increase the stiffness compared to the baseline while incorporating the damage resistance observed in the Kevlar-faced experiment.

Impact and Scan Results are shown in the Figure 83 and Table 11, with similar trends to the Kevlar-faced samples, and impact performance is similar.

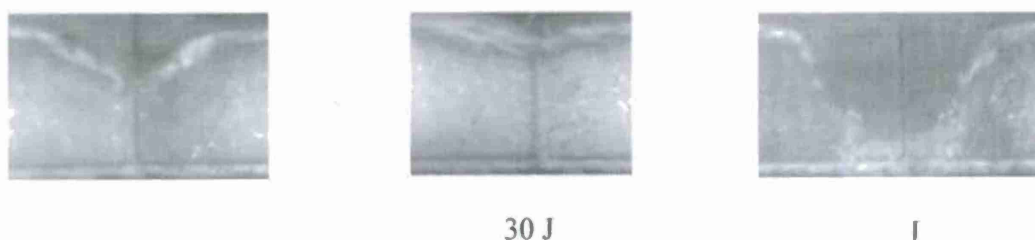


Figure 83: Damage Cross sections with Kevlar interleaved

Table 11: Damage Modes and Penetration with Kevlar interleaved

	Penetration Depth (in)	Damaged Area (in ²)	Observed Failure Modes
20 J	0.260 (40%)	0.230	Minimal delamination
30 J	0.360 (55%)	0.290	Partial breakage, with Core Crushing and Delamination
50 J	0.600 (93%)	0.53	Significant Core Crushing and Delamination, along with Fiber Breakage

A comparison of pre- and post-impact flexural performance in Figure 84 shows interesting trends, there is a measurable increase in failure load compared to the baseline (~12%), which is not expected due to the core failure dominated flexural behavior. While Kevlar has good tensile properties (modulus and strength), it has poor properties in compression. The addition of the Kevlar layer closer to the core appears to improve the shear capacity of the core and bears further investigation.

Impact performance is similar to the Kevlar-faced system, though slightly worse. Damage depths are slightly higher than the Kevlar-faced system, though damaged area is significantly smaller and more localized. Failure loads and stiffnesses remain almost unchanged pre and post-damage.

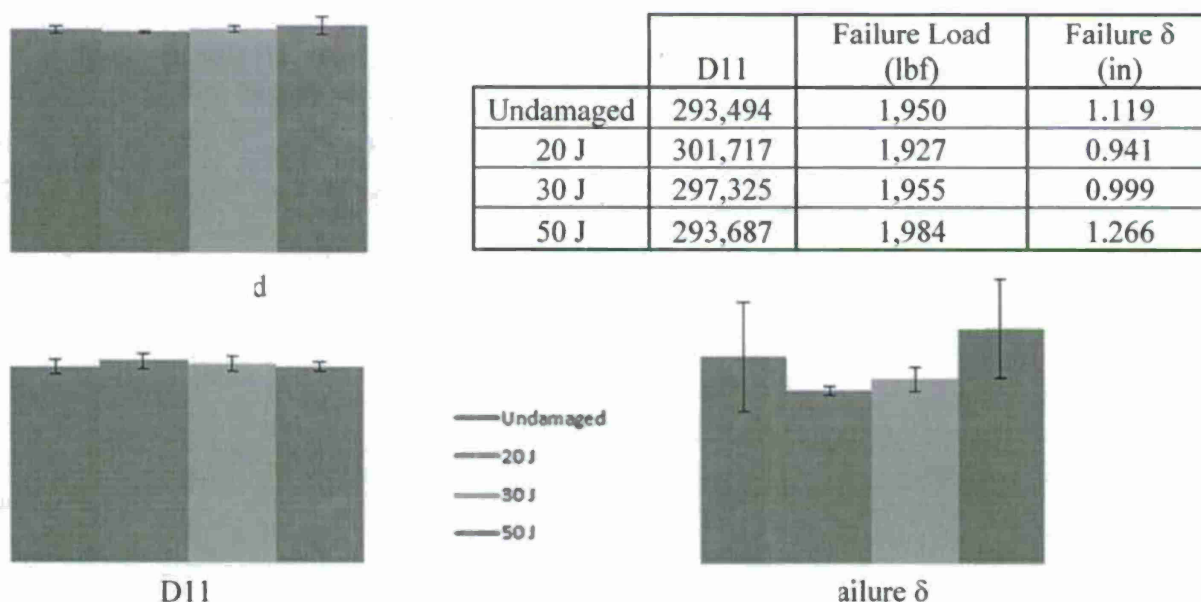


Figure 84: Flexural stiffness (D11), Failure load and failure depth for Kevlar interleaved system

Milestones Accomplished

Early hybrids have demonstrated that the hybridization approach is capable of improving the post-impact response of CFRP sandwiches by considerably reducing the through-thickness penetration as well as damage area. Kevlar-faced Hybrids have proven to be especially difficult to damage; with the lower range of impact energies providing little to no observable damage - even after sectioning - and little internal damage when scanned ultrasonically.

Path Forward

A mass and thickness equivalent carbon baseline series of coupons are to be tested to remove the possibility of the increase in impact performance being a result of more material obstructing the tups progress through the specimen. These coupons are to be 6 layers thick per facing, representing a $[+/- 45/03/90]_s$ layup. These specimens are anticipated to have a significantly higher undamaged stiffnesses and failure loads due to the addition of CFRP than any of the currently tested systems.

Dyneema, a stiff, synthetic fiber, is planned to be incorporated into the facing material in a similar fashion to the Kevlar. We expect the Dyneema system will behave similarly to the Kevlar system though at a lighter weight. Following the characterization of the dyneema specimens, additional fabrics are to be tested in a similar fashion.

Interleafing - a promising methodology for improving impact performance - will be incorporated into the test matrix after fabric testing is complete. Interleafing has been experimentally demonstrated to reduce the post-impact losses by as much as 30% (Duarte, Herzberg & Paton) with little change from initial properties.

References

1. Peijs, A.A. J.M., R. W. Venderbosch, and P. J. Lemstra. "Hybridcompositesbased on Polyethylene and Carbonfibres Part 3: Impact Resistant Structural Composites through Damage Management." *Composites* 21.6 (1990): 522-30.
2. Yi, X.-S., and X. F. An. "Effect of Interleaf Sequence on Impact Damage and Residual Strength in a Graphite/epoxy Laminate." *Journal of Materials Science* 39.9 (2004): 3253-255.
3. Gustin, J., A. Joneson, M. Mahinfalah, and J. Stone. "Low Velocity Impact of Combination Kevlar/carbon Fiber Sandwich Composites." *Composite Structures* 69.4 (2005): 396-406.
4. Agarwal, Bhagwan D., Lawrence J. Broutman, and K. Chandrashekhara. "Impact." *Analysis and Performance of Fiber Composites*. 3rd ed. Hoboken, NJ: John Wiley & Sons, 2006. 395-416.
5. Duarte, Andre, Israel Herszberg, and Rowan Paton. "Impact Resistance and Tolerance of Interleaved Tape Laminates." *Composite Structures* 47.1-4 (1999): 753-58. Print.

Task IX. Integration of CFD to Structural Analysis for Streamlining the Marine Design Process

Motivation and Background

In the design of a small high-speed craft, designers rely on the semi-empirical design methods, e.g. design rules by ship classification societies [1]. A current issue on wave slamming is that the guidelines for slamming design loads are limited to small planning hulls [2] or steel vessels [3], and have no consideration about multiple impact effects. A large number of theoretical and experimental studies on water impact problems have been performed for more than half a century; however design methods for repeated impulsive loads have still not been well understood.

This task explores improving the current design process so that composite sandwich hulls are managed more safely and effectively against wave slamming loads. The research question is related to design methods for impulsive and multiple slamming loads in order to consider the long-term durability of sandwich composite hull materials for high-performance composite vessels. CFD technique is applied to predict the pressure profiles from the fluid flow fields of water impact problem. The CFD software platform selected was the commercial code, STAR CCM+. The wave slam pressure determined by the simulation will be simulated experimentally for multiple cycles. This study also develops unique experimental methods based on Dynamic Mechanical Analysis (DMA) technique.

Objectives and Goals

The most important research effort is to specify what requirement for constituents to survive under the severe environment over the ship life time is. The final goal is to systematize the modeling and the experimental methods to be able to estimate the long-term effect considering materials system, sea state, ship speed and general configuration. This systematization will have to contribute for selecting a material in the design process reasonably considering the slamming effects. It will be beneficial to improve the design requirement for composite sandwich vessels.

Approach

Experimental method to apply the repeated slamming loads

The experimental study focuses on developing advanced Dynamic Mechanical Analysis (DMA) methods by simulating the wave slam loading. Basic principle of DMA is described as analyzing the responses between the sinusoidal stress caused by an oscillating force to a sample and the sinusoidal strain generated in it in order to measure dynamic mechanical and viscoelastic properties. The preferable feature in DMA is its flexibility to control magnitude, frequency and cycles in applied displacement/force profile. The experiment has to keep a consistency with the nonlinear and complicated aspect in wave slam loading as possible: a high pressure peak in a very short period, a subsequent duration with plateau pressure and dwell time between repeated impulsive loads. The particular challenging task is to simulate the slamming loads, and evaluate dynamic response and long-term durability of a foam core, which will be mentioned in detail

later. The unique approach however will be novel and versatile experimental methods for characterization of composite sandwiches.

Long-term durability of a foam core material due to slamming

Polymeric foams are widely used as cores in the structural or non-structural components for marine composite sandwich structures. High rate loading of the slamming might affect property of a foam core more than that of faces. In general, core failure and / or interface debonding have been considered as the primary failure modes in the sandwich composite of slammed hull due to wave slamming. Repeated and long-term wave impacting can degrade property of a foam core, and cause local and fatigue damages even if the single encounter is not severe. Most of past researches have paid attention to response against the peak pressure of single wave slam. DMA is an applicable technique for fatigue characterization of a foam core with correct consideration of the internal heating effect. Fatigue characterization by DMA will offer new rapid and affordable method compared to conventional test ones.

Numerical modeling to evaluate the wave slamming of stiffened composite sandwich structures

This task will apply CFD techniques to wave slamming problem. The modeling requires to be validated by the analytical solutions for water impact problem. The later phase of this research will focus on demonstrating the numerical simulation of a stiffened composite sandwich structure. Damage caused by slamming can depend on the structural configuration including stiffeners. The CFD and FEA modeling of a composite sandwich structure will incorporate the foam core property. This demonstration will integrate the experiment and modeling and provide practical foresight into future design methods.

Results and Discussion

Benchmark of a Foam Core Property by Static Compressive Testing

The applicability of DMA testing has been focused on for obtaining the consistent core property. There is significant difference in specimen geometry between a standardized test and a DMA measurement: a much smaller specimen needs to be prepared for DMA. Benchmark experiment was therefore performed in order to verify the mechanical properties and the microscopic failure modes between DMA-type and baseline specimens.

Table 12 lists geometry of the prepared test specimens. All of them are cuboid and square in cross section. All specimens were tested at room temperature in an Instron 5848 MicroTester system.

Figure 85 shows the representative stress-strain relations for each specimen. All curves exhibit linear elasticity first, yield points, and subsequently declines to plateau stresses. The left plot in Figure 86 compares the compressive strength obtained for each specimen. The cross marks represent the manufacturer's data. Although small specimen has larger variation, the compressive strengths are almost identical. On the other hand, there is obvious variation for the moduli shown in the right plot in Figure 86. Small and thin specimens have the lower moduli than baseline. One of the reasons is that some initial damages caused by machining can lead to the compliant response. However, as for the mechanical property a small specimen is consistent with the baseline material, and has uniform property through the thickness.

Table 12: Foam Specimen Geometry for Benchmark Testing of Static Compression

	Baseline	Small (DMA-type)	Medium	Thin
W, T	30 mm	4 mm	15 mm	30 mm
H	38 mm	5 mm	19 mm	5 mm
Slenderness Ratio	4.40	4.33	4.39	0.58
Strain Rate	0.1	0.1	0.1	0.1

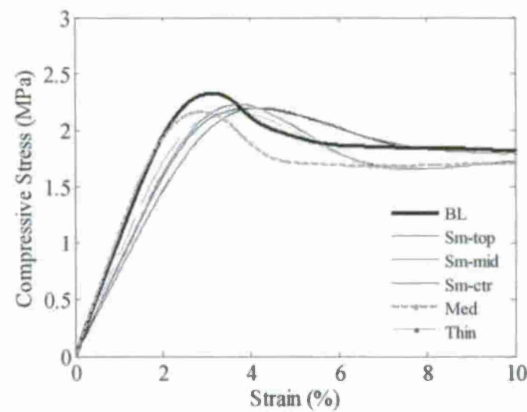


Figure 85: Comparison of Stress-Strain Relationship for Different-sized Foam Specimens

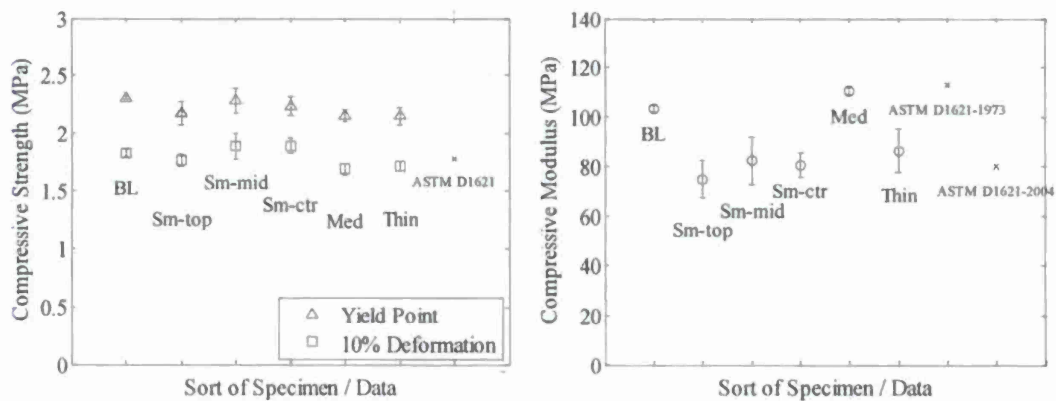


Figure 86: Comparison of Compressive Strength (Left) and Modulus (Right) for Different-sized Foam Specimens

Dynamic Compressive Strain Sweep Testing

A compressive strain sweep test by DMA evaluates mechanical behavior responding to linearly increasing displacement amplitude until a foam core crushes. DMA measurements were

performed using the METTLER TOLEDO DMA/SDTA861e system at ambient temperature and frequency of 1Hz. Test specimen is DMA-type specified in Table 2.

Figure 87 shows the modulus with respect to the displacement amplitude or dynamic strain. The storage modulus decreased as displacement increased. It was found that the highest modulus is close to the static compressive modulus. Figure 87 also provides the dynamic stress-strain relation schematically. The offset can be added as static contribution by force control to ensure perfect contact between the specimen and the holding fixture. Although the dynamic and static contributions are included in the total response, the result is comparable to the typical stress-strain curve obtained under static loading.

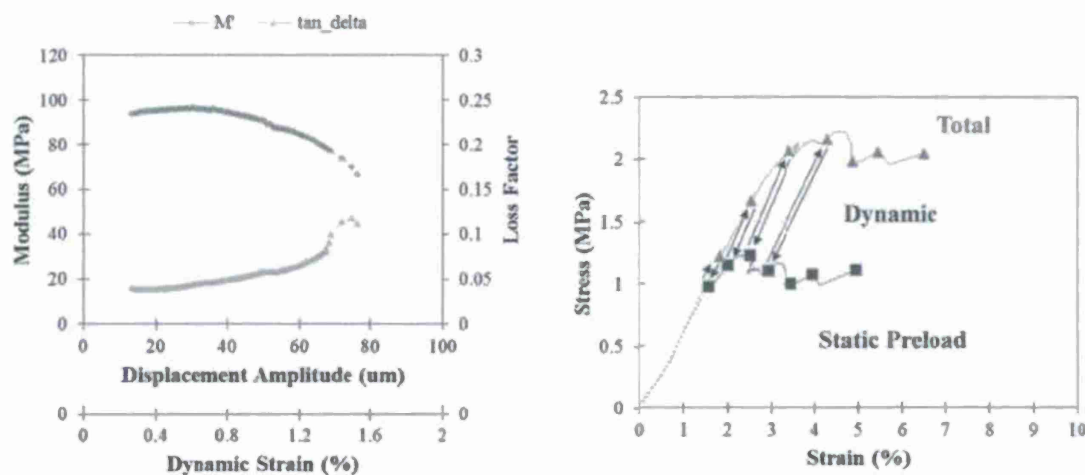


Figure 87: Dynamic Strain Sweep Test Results of Modulus-Displacement (Strain) Relation (Left), and Stress-Strain Relation (Right)

Approximation of Wave Encounters

Slamming event is characterized essentially by the impact velocity and the frequency of impact: the former relates to the peak and duration of slamming pressure pulse and the latter describes the repeated cycles. The fundamental study approximates the vertical impact velocity and the frequency of wave encounters based on the sea state. The sea state number classifies statistically the sea condition including the wave height and period. Table 13 shows the typical parameters for Sea State 1 through Sea State 8 from the sea state chart [1][2].

The frequency of occurrence of wave slamming is an important characteristic which relates to hull material durability. In general, the slam frequency depends on the sea condition as well as the length, speed, and direction of the ship with respect to the waves. A ship motion analysis is usually conducted to predict the velocity and motion at the impact position of the ship. However, the frequency which the ship encounters a wave with can be approximated from the wave conditions and the ship speed as follows.

$$f_E = f_w + \frac{V_s}{L_w}$$

where f_E is the frequency of wave encounters (crest/sec), f_W is the frequency of the wave (crest/sec), V_S is the ship speed (m/s), L_W is the wave length (m). Assuming the most probable Sea State 4 and the ship speed of 50 knots,

$$f_E = \frac{1}{5.3 \text{ (sec)}} + \frac{25.7 \text{ (m/sec)}}{28.80 \text{ (m)}} = 1.08 \text{ (crest/sec)}$$

This means that the ship encounters approximately 3,900 waves in an hour. **Error! Reference source not found.** Figure 85 also shows the wave encounters with respect to the sea state and the ship speed when the operating time is assumed to be 1000 hours. The possible number of experiencing waves can exceed a million-cycle which corresponds to characterize the fatigue property of materials.

Table 13: Sea State Parameters

Sea State	Probability of sea state (%)	Significant Wave Height (m)	Average wave period (sec)	Average wave length (m)
1	0.7	0.20	1.9	4.07
2	6.8	0.66	3.4	12.09
3	23.7	1.23	4.3	19.81
4	27.8	1.98	5.3	28.80
5	20.64	3.05	6.3	41.15
6	13.15	4.67	7.4	57.30
7	6.05	9.27	9.7	97.80
8	1.11	15.54	12.0	149.35

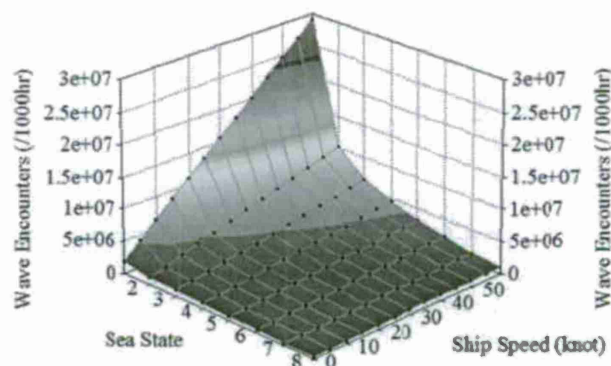


Figure 88: Approximation of Wave Encounters (Right)

Milestones

Path Forward

CFD Modeling

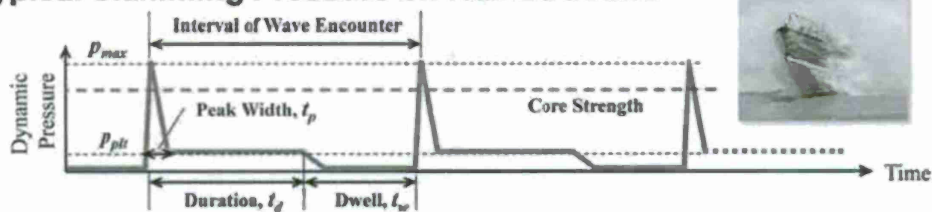
The CFD simulation using STAR-CCM+ will be validated on a water slamming problem where the pressure distribution on an impacted body can be calculated analytically. It will be compared to the slamming analysis performed by explicit FEA code as well. For this purpose, the CFD and FEA modeling will be performed to predict the water slamming pressure assuming the impacted structure as a rigid body.

Advanced DMA Methods

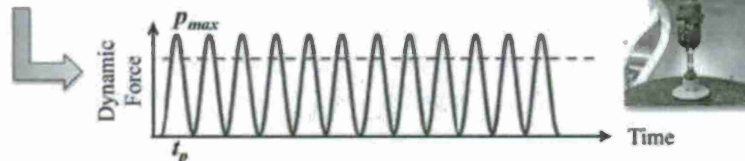
The most important scientific/technical problem is to develop experimental method utilizing DMA, which will be a quite unique contribution. The complication is to simulate the impulsive pressure of wave slamming physically, and analyze the fatigue performance. As shown Figure 88 slamming pressure on a hull structure can be typically characterized by peak pressure (p_{\max}), peak width (t_p), plateau pressure (p_{plt}), duration (t_d), and dwell time (t_w). With extreme wave environment, the peak pressure can cause stresses in excess of foam core strength. Even if this excessed pressure acts for a brief instant of time, effect of the long-term repeated loading is unpredictable. On the other hand, effect of the plateau pressure on impacted damage is considered very small since it has lower amplitude than the peak pressure, and in fact most studies have developed predictions for the peak pressure 0. The plateau pressure however might be more influential if we consider multiple impacts on a foam core. In this research, the actual wave-slam loading is decomposed into high frequency and low frequency components. The high frequency load consisting of p_{\max} and t_p will be simulated by DMA while the low frequency load consisting of p_{plt} and t_d by a hydraulic test machine. Long-term durability of a foam core will be investigated by 1) high frequency DMA testing, and 2) low frequency fatigue testing. The successive high-frequency loading with larger amplitude is the most severe case and will provide an evaluation on the save side, while the low-frequency loading will be a lower bound.

DMA methods will be explored for the high frequency testing. DMA can work by applying a sinusoidal oscillating force to a specimen. The METTLER TOLEDO DMA/SDTA861e has a wide frequency range from 0.001 Hz to 1000 Hz (up to 300 Hz in compression mode), and a force range up to 40 N. The capability for frequency and force will be able to program methods to simulate the impulsive slamming pressure. On the other hand, a conventional fatigue test machine will be able to be utilized for a foam core to be loaded under the plateau pressure with a relative long duration of the lower pressure Figure 89 also shows the schematic of DMA oscillation for simulated peak pressure and cyclic loading for plateau pressure over time. The experimental study will conduct the DMA testing under frequencies higher 20 Hz.

♦ **Typical Slamming Pressure on Hull Structure**



♦ **High Frequency DMA Testing**



♦ **Low Frequency Fatigue Testing**

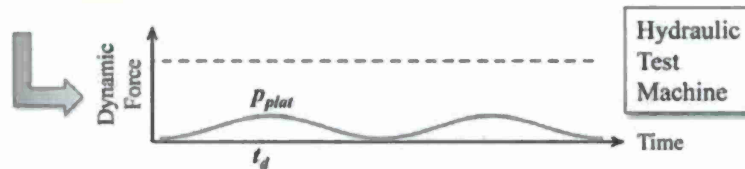


Figure 89: Development of DMA Methods for Fatigue Characterization of a Foam Core

References

- [1] I. Stenius, A. Rosén, and J. Kutteneuler, Hydroelastic Interaction in Panel-water Impacts of High-speed Craft, *Ocean Engineering*, vol. 38 (2011), pp. 371-381.
- [2] S. Kim, D. Novak, K.M. Weems and H.-C. Chen, Slamming Impact Design Loads on Large High Speed Naval Craft, *SuperFAST'2008*, Russia (2008).
- [3] ABS, Guide for Slamming Loads and Strength Assessment for Vessels, March 2011(updated March 2012).
- [4] ISSC, Report of Committee Technical Committee V.7: Impulsive Pressure Loading and Response Assessment , *Proc.17th International Ships and Offshore Structures Congress*, Seoul, Korea, vol.2 (2009).
- [5] O.M. Faltinsen, *Sea Loads on Ships and Offshore Structures*, Cambridge University Press, Cambridge (1990).
- [6] Naval Surface Warfare Center, Unknown Title (Sea State Chart), *NSWCCD-23-TM-1999/16* (1999).

Task X. Virtual Simulation for Cost Reduction

Motivation and Background

The engineering of large structures from advanced composite materials often involves venturing into unknown territory with regards to the selection of manufacturing methods. This is particularly a problem for boat design. Most boat design standards have been developed for wooden or metal vessels, or standard fiber reinforced polymers (FRP). The lack of engineering standards makes it challenging to estimate the costs of producing boats from advanced composite materials, as few historical benchmarks exist. The cost estimation tools developed herein provide the engineer with the economic guidance needed to understand the cost implications of choices made during conceptual design and selection of manufacturing methodology. The methodology uses the principles of time-driven activity based costing, and for scaling the ship hull design uses the American Bureau of Shipping Standards and the scantling rules proposed published by Gerr[2000]. It should be noted that scantling rules encounter physical limitations at moderate dimensions. In order to scale the cost model beyond these limits, the scaling formula and approaches to production must be validated by detailed engineering design and experimentation. The purpose of this study is to develop cost estimates derived from the ABS standards based model to guide the engineer towards the most cost efficient choice of manufacturing design methodology.

Task 10 relied heavily on inputs from other tasks, including: task I, IV and V.

Objectives and Goals

The cost model involved in this study is currently being used to understand the economic implications of design and manufacturing process tradeoffs involved during the design phase. In addition, the model is dynamically scalable so that the costs of alternative hull dimensions may be investigated. The cost model is specifically tuned to allow for the following key choices: 1. Material selection; 2. Ply Configuration; 3. Process selection (e.g., bagging options, placement, capital configuration)

Approach

The current effort involves the evaluation of alternative approaches to laminate consolidation. Three scenarios are currently interesting to further the advancement of processing science: 1) in situ or bagless consolidation, 2) consolidation using spray-on membranes, 3) consolidation using traditional film vacuum bagging.

Activity-based costing is an approach to computing cost that divides the cost pools into major steps aligned with the production process [Karbhari & Jones, 1992; Jones et al, 1999]. Time-driven activity costing assigns the cost of supplying the resource (e.g., oven) to objects (e.g., curing). The cost per unit time is then computed based upon total available capacity of the resource. Cost is assigned to the unit of production based upon the time it actually takes to complete the activity [Kaplan & Anderson, 2007]. In the model, idle time and unused or excess capacity costs are also tracked and reported. The actual amount of unused capacity cost is highly

dependent on the assumed lifetime production volume of the boat, and is not discussed herein for purposes of brevity. We will therefore assume that all available capacity is used for some type of production. The use of activity based costing and the ability to use these models to manage the cost of ATL has been demonstrated for aerospace applications [Jones et al, 1998].

The large number of parameters in Task 10 are developed from three principle sources: studies conducted in laboratories at the University of Delaware Center for Composite Materials, published findings from historical industry reports and publications, and current published vendor price lists. Because of limited experience using ATL for naval ships, many parameters are adapted from aerospace publications. In addition, a database of high performance hull dimensions was used to devise primary functional relationships such as length-to beam ratios. The model assumes all material is placed using automated fiber placement. The size of the gantry, ovens for curing and manufacturing area all scale relative to the size of the vessel. The placement process can accept many parameters, but for the purposes of this paper the assumed tape width is held constant 0.3048m. The model also accommodates time to reload material and change end effectors as needed. Adjustments to placement speed are made for complex parts. The ship is divided into multiple components for fiber placement (hull, framing, decks, bulkheads). Individual components are placed and consolidated separately and then bonded together in a final assembly step.

An important consideration in the manufacture of the laminate and other structural components is the consolidation process. As the number of plies increases, so does the need for additional consolidation cycles. Thus, if there is a way to reduce the cost of each cycle, the overall cost of the vessel may be managed and the optimal tradeoff between manufacturing cost and stiffness can be determined. The base case is traditional film bagging, whereby a crew manually places and seals the film seams to encase the part for vacuum consolidation. The spray-on membrane alternative substitutes for film bagging material by spraying on a silicon membrane. Less labor is required using this alternative because low cost automation is used to disperse the membrane, although some additional processing time is needed to cure the membrane. Nominal additional capital costs are needed as the cost increments are dominated by materials. The consolidation process is similar to film bagging. In the final alternative, in situ consolidation substitutes for the film and the vacuum process. Here, placement and consolidation occur simultaneously, no vacuum bagging is needed. The placement apparatus is augmented by additional heating and pressure at placement. Additional end effector cost should be added to the capital costs, but is presently indeterminate.

Results and Discussion

Figure 90 shows how material and labor costs differences between spray-on membranes and film bagging change as spray bag thickness and the length of the ship increases. The material difference plots (Spray - Film) in Figure 91 are for the range of membrane thicknesses of 6.35E-4m to 3.18E-3m. As is evident, a thicker membrane results in a greater cost disadvantage to the spray-on approach. The material cost for spray-on membranes increases somewhat exponentially for low to moderate length (20 to 40m) vessels as the displacement increases due to simultaneously increasing length, beam, and depth. A greater displacement indicates that more material is needed for the hull and for internal structural support. In the case of film bagging,

more bagging material, labor, and time is also needed to cover the hull and frame components during consolidation as the vessel length increases. The positive trend of the plot indicates that the material cost for spray bagging is always greater than film bagging, and there is an exponential growth in the amount of material used because of the exponential increase in surface area that results from increasing the length of the vessel. Thus, there is a cost advantage to developing thinner membranes. The added material cost for spray-on membranes is offset by the reduced labor costs involved as a result of the selection of this consolidation method. The thickness of the membrane has little to do with labor costs, although some additional labor costs are incurred for thicker bags because of the slightly longer duration required to deposit the membrane, since a constant flow rate is assumed.

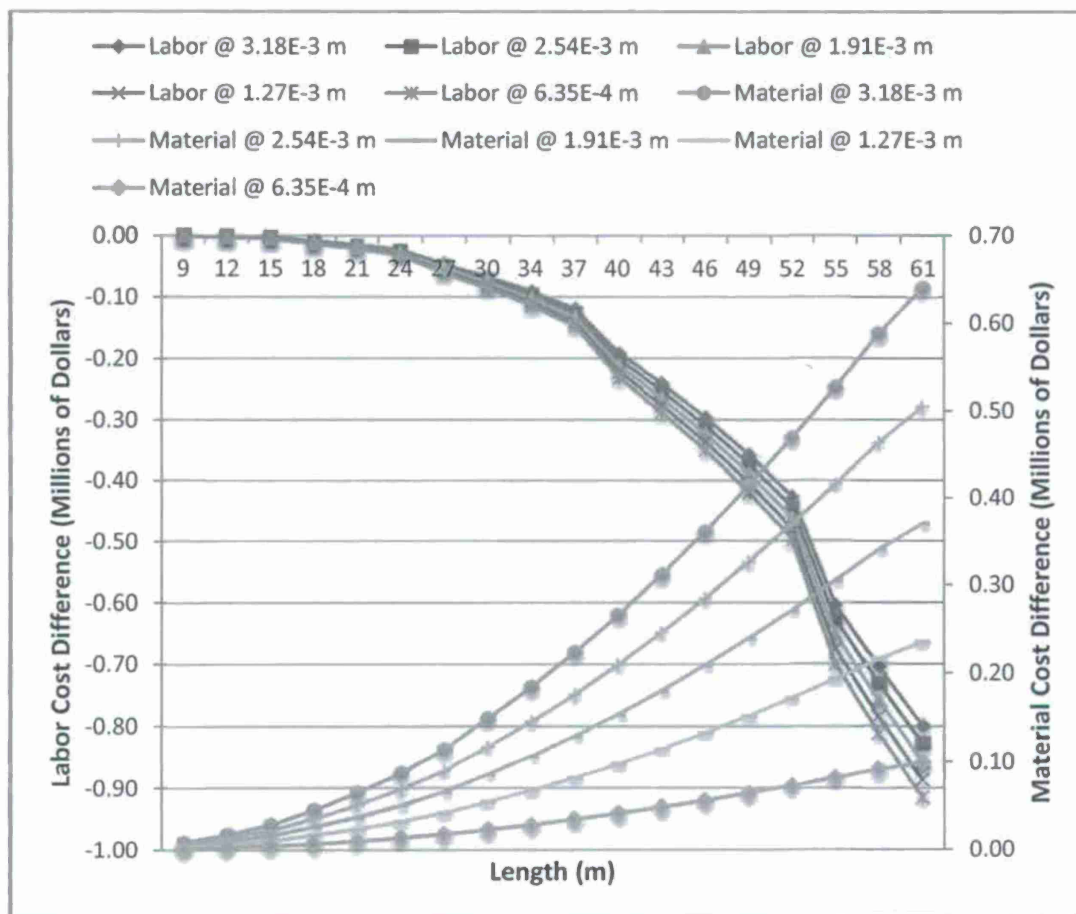


Figure 90. Materials and labor cost differences (Spray – Film) by membrane thickness

The total labor cost is very similar for spray-on and film bagging for vessels up to about 30 meters in length, as indicated by a negligible cost difference. After that point the beam and depth dimensions of the vessel begin to add significantly to the outer mold line of the hull's transverse cross section. This increases the amount of labor needed to handle film bag placement.

In our time-based activity costing model, indirect costs (including both active and idle time), are allocated to production on the basis of time spent in each production cell. Thus, the added labor

time of film bagging tends to accumulate more overhead costs beginning with more moderate displacement vessels of 30m in length. Time-based allocation of production cell indirect costs is the proper methodology because the hull and related structures are too large to be moved in and out of a cell, so resource consumption is thus fundamentally related to time. Figure 91 shows the cost difference when capital costs are allocated on the basis of time. The analysis indicates that on a full cost basis, even relatively thick spray-on membranes (2.54E-3 to 3.18E-3m) could result in cost effective production of ships in the 40m range. Again, when fully burdening production with a time-based allocation of work cell indirect costs, the film bagging process absorbs more costs. Hence, the cost advantage of film bagging disappears at vessel lengths of around 30m. If very thin spray membranes (6.35E-4m to 1.27E-3m) can result in adequate permeability, then cost advantages of that process can be attained at lengths of 15m to 20m. An advantage of spray-on membranes is that the flow rate and nozzle positioning can be adjusted to increase deposition rate of the material. In this case, the nozzle flow rate remained at 0.015 m³/hour per nozzle, with three nozzles per meter of outer mold line(OML). Additionally, since the shelf life at room temperature of many materials is limited, a further advantage accrues to spray-on membranes. Since the process takes less time, it may decrease the risks associated with premature curing of material.

In conclusion, the cost model results show that traditional film bagging has a combined labor and material cost advantage over spray-on membranes for smaller vessels. If the spray membrane thickness can be reduced, then the cost advantage of film bagging begins to diminish. Spray-on membranes offers a reduction in labor cost that outweighs its added material cost. This advantage may occur at lower displacements, depending upon the method of indirect cost allocation. We believe the economic conclusions justify continued research and development in spray-on membrane applications.

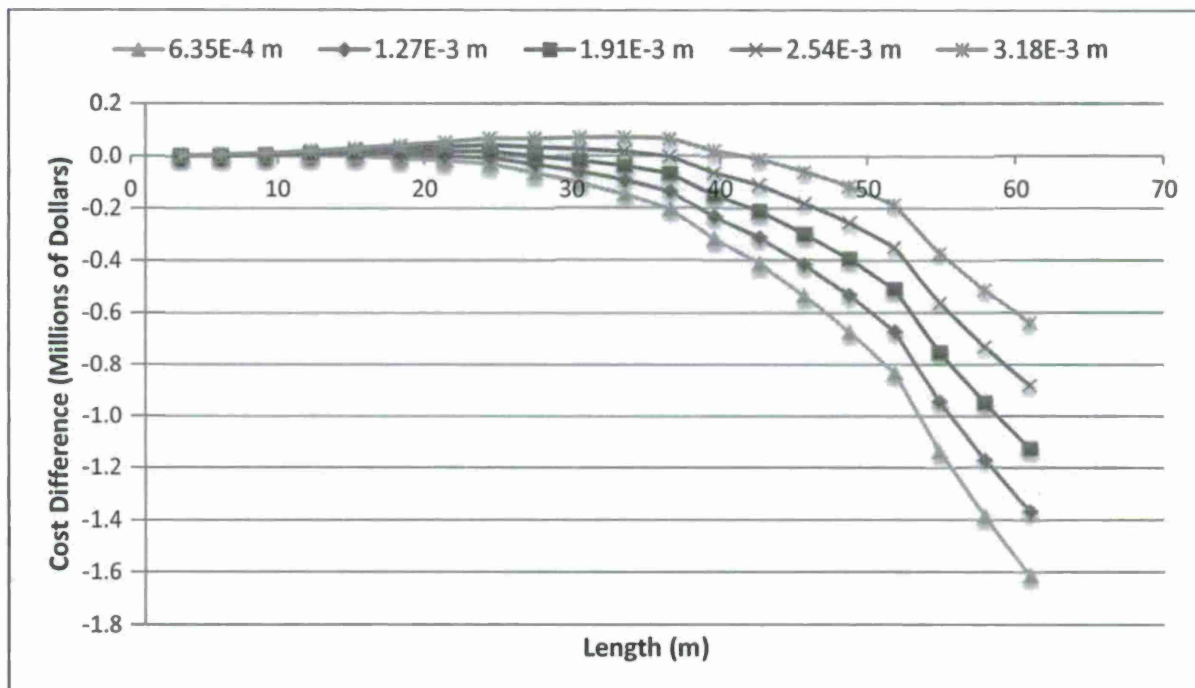


Figure 91. Spray – Film Total Cost Difference

Next, we consider the prospects of *in situ* or, on-line, consolidation. It is assumed that *in situ* consolidation is possible and that equally repeatable, identical-quality parts can be produced across the three consolidation methods. At the present time, the capital investment needed is unknown. Instead, Figure 92 presents capital payback rates as an alternative to making uncertain assumptions. Figure 92 shows the overall cost comparisons across the three processes. In Figure 92 we assume that the three methods use the exact same material deposition rates of $0.0155 \text{ m}^2/\text{s}$. Figure lists the potential cost savings of the *in situ* method over the alternatives. The advantage of *in situ* consolidation over thin spray-on membranes is generally less than 1-2%, compared to a 3-5% advantage over thick membranes. The cost advantage of *in situ* consolidation over film bagging is quite substantial, from about 2% up to 10% for larger vessels. This suggests that there is promise for further development of *in situ* consolidation methods. The main limitations at this point seem to be the constraints on the allowable material deposition rate inherent with *in situ* methods due to laminate material property requirements as well as the unknown additional capital costs required. The payback per unit ranges widely depending on vessel length. Contingent on the number of units to be produced, the total payback for an investment in an *in situ* consolidation apparatus could be substantial.

Length	10m %	20m %	30m %	40m %	50m %	60m %
<i>In situ</i> – $6.35\text{E-}4\text{m}$ Membrane	1.7	1.1	0.9	0.8	0.8	0.7
<i>In situ</i> – $3.18\text{E-}3\text{m}$ Membrane	4.9	4.6	4.2	3.8	3.5	3.4
<i>In situ</i> - Film	2.2	3.1	4.6	6.4	7.8	9.7
Investment payback rate (range in \$000/unit)	5.1- 6.1	22.0- 63.7	49.8- 246.5	92.5- 691	173.4- 1,881.5	257.8- 3,571.1

Figure 92. Potential manufacturing cost savings using *In Situ* consolidation at $0.0155 \text{ m}^2/\text{s}$ deposition rate

It is entirely likely that the deposition rate for *in situ* methods would be less than that for a more traditional approach such as film bagging. This scenario is considered below. An analysis was conducted to determine the point at which the cost of each method is equal for a given speed and vessel size. Figure 93 is a plot of the indifference points across the three consolidation methods, showing deposition rate versus vessel length. In the comparison of spray-on and film bagging, it is assumed that the deposition rate is $0.0155 \text{ m}^2/\text{s}$ and the thickness of the spray-on membrane is $3.18\text{E-}3\text{m}$. There is no limitation in the consolidation approach that would require the placement rate to slow down, resulting in a vertical line at approximately 28m in length. Below 28m the labor and material cost of film bagging is lower than that of spray-on membrane consolidation, so film bagging is preferred. Larger vessels could be produced more cost effectively by spray-on membrane consolidation. To consider *in situ*, the alternatives of film and spray-on are fixed at a placement rate of about $0.0155 \text{ m}^2/\text{s}$, while the *in situ* method is slowed to as little as $0.002 \text{ m}^2/\text{s}$. Figure 93 shows the resulting indifference curves. At a deposition rate of about $0.007 \text{ m}^2/\text{s}$, and a vessel length of about 28m, the selection of a particular consolidation method is irrelevant. The areas boxed show the combination of deposition rate and ship length that favor each method. For small vessels, film bagging is preferred to *in situ* for deposition rates less than about $0.007 \text{ m}^2/\text{s}$. For larger vessels (28m or more) both *in situ* and spray-on consolidation methods are preferable to film bagging. The boundary between *in situ* and spray-on indicates that by

improving deposition rates of *in situ*, larger the vessels that can be produced as cost effectively as using spray-on membranes. For small vessels (up to 30m), *in situ* could operate as slow as 50% of the film bagging speed and remain cost competitive.

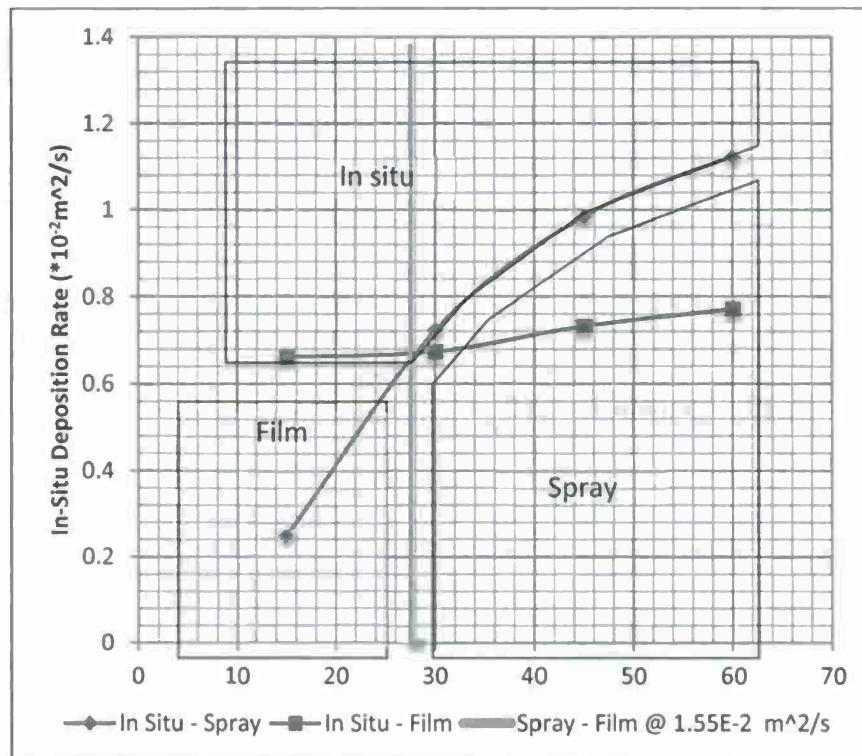


Figure 93. Cost indifference points across consolidation methods

Milestones Accomplished

In this task the costs of producing high speed ship hulls and related structural components using three alternative processes for consolidation are determined. The consolidation methods evaluated were traditional film bagging, spray-on membranes, and *in situ* or on-line consolidation.

The results obtained suggest that traditional film bagging is very cost effective for smaller vessels (less than 25 to 30m). Larger vessels could see cost reductions if thin spray-on membranes can be developed. Thin membranes could produce significant cost reductions beginning at vessels of 20m in length. There is also a cost advantage to *in situ* consolidation if the process can be maintained at deposition and consolidation rates comparable to film bagging and spray-on membrane. Cost reductions of up to 10% could be realized for larger vessels.

Path Forward

A model of risk has been developed that identifies the worst-case scenario for failure based on voids and related material properties. These risks will be integrated into the cost model to help determine costs associated with various void contents. Currently, the UD-CCM advanced

placement robotics tests results are being used to populate the risk model with experimental void content results and placement properties.

References

1. American Bureau of Shipping. "Guide For Building And Classing High-Speed Craft" American Bureau of Shipping: New York, NY. October 2001.
2. American Bureau of Shipping. "Guide For Building And Classing Reinforced Plastic Vessels 1978, Notices No.1 and No. 2." American Bureau of Shipping: New York, NY. May 1992.
3. Gerr, Dave. The Elements of Boat Strength: for Builders, Designers, and Owners. Camden, ME: International Marine, 2000.
4. Jones, S., Raciti, R., Stolfo, K., Steiner, K., & Lamontia, M. "Hybrid Methodology for Quantifying the Cost and Productivity of Manufacturing Scenarios for the Automated Fiber Placement of Aircraft Skins," Proceedings of the 43rd International SAMPE Symposium, June 1998. Society for the Advancement of Material and Process Engineering. pp. 44-55.
5. Jones, S., Wright, D., & Karbari, V., "The Relevance of Activity-Based Management Support for Composite Structures Design." *Advances in Management Accounting*, 7 (1999): 1-24.
6. Jones, S., & Wright, D., "Assessing the Relevance of Cost Information for Product Design," *Challenging the Status Quo in Design*. Chicago, Ill., March, 1994. Society of Plastics Engineers. pp. 151-156.
7. Jones, Scott. "Cost Accounting" *Marks Standard Handbook for Mechanical Engineers*, Ed. Eugene Avallone and Theodore Burmeister, 11ed. McGraw-Hill Book Company: New York. 2007.
8. Karbhari, V., & Jones, S. "Cost Information Barriers and Composite Materials." *International Journal of Materials and Product Technology*, 7(3) (1992), 215-230.
9. Kaplan, R. & Anderson, S. "The Innovation Of Time-Driven Activity-Based Costing," *Cost Management*, 21(2) (March 2007), 5-15.